Vibronic coupling and ultrafast electron transfer studied by picosecond time-resolved resonance Raman and CARS spectroscopy

Dissertation

zur Erlangung des akademischen Grades
doctor rerum naturalium

(Dr. rer. nat.)
im Fach Physik
eingereicht an der

Mathematisch-Naturwissenschaftlichen Fakultät I
der Humboldt-Universität zu Berlin

von

Diplom Physiker Sebastian Wachsmann-Hogiu
geboren am 1. Februar 1968 in Rumänien

Präsident der Humboldt-Universität zu Berlin
Prof. Dr. Dr. h. c. Hans Meyer

Dekan der Mathematisch-Naturwissenschaftlichen Fakultät I
Prof. Dr. Bernhard Ronacher

Gutachter/innen:	1. Prof. Dr. Thomas Elsässer, Humboldt Universität Berlin
	2. Prof. Dr. Beate Röder, Humboldt Universität Berlin
	3. Prof. Dr. Wolfgang Kiefer, Universität Würzburg

Tag der mündlichen Prüfung: 18.10.00

Herrn Prof. Dr. Thomas Elsässer danke ich sehr herzlich für die interessante Themenstellung und für die Förderung, Betreuung und Unterstützung dieser Arbeit. Die motivierenden Gespräche waren für mich sehr wichtig beim Fortgang meiner Untersuchungen.

Herrn Dr. Wolfgang Werncke danke ich für die stetige Förderung und Betreuung, für die gute Zusammenarbeit im Labor und für die zahlreichen Ratschläge und Diskussionen bei der Anfertigung dieser Arbeit.

Mein besonderer Dank gilt

Herrn Dr. Albrecht Lau, für die Möglichkeit, in seiner Arbeitsgruppe als DAAD Stipendiat zu lernen, und für stetige interessante Diskussionen,
Herrn Dr. Michael Pfeiffer für die gute Zusammenarbeit,
Herrn Dr. Jens Dreyer für die freundliche Unterstützung bei Klärung schwieriger Probleme,
Herrn Dr. Erik Theodorus Johannes Nibbering für fruchtbaren Diskussionen,
Herrn Dr. Peter Hamm für anregende Gespräche,
Herrn Dr. Andreas Kummrow für hilfreiche Diskussionen,

Frau Regina Goleschny, Frau Brigitte Steinert, Frau Britta Neutenkötter, Frau Karin Kirchner und Herrn Günter Schultz für vielfältige Hilfe im Labor,

sowie allen Kollegen im Institut für eine hervorragende Arbeitsatmosphäre.

Veröffentlichungen im Zusammenhang mit dieser Arbeit

- S. Hogiu, W. Werncke, M. Pfeiffer, A. Lau, T. Steinke; „Picosecond time-resolved CARS spectroscopy of a mixed excited singlet state of diphenylhexatriene“, *Chem. Phys. Lett.* **287** (1998) 8
- S. Hogiu, W. Werncke, M. Pfeiffer, A. Lau; „Evidence of strong vibronic coupling in the first excited singlet state of diphenylhexatriene by picosecond CARS spectroscopy“, *Chem. Phys. Lett.* **303** (1999) 218
- M. Pfeiffer, W. Werncke, S. Hogiu, A. Kummrow, A. Lau; „Strong vibronic coupling in the first excited singlet state of diphenylhexatriene by an asymmetric low-frequency mode“, *Chem. Phys. Lett.* **295** (1998) 56
- W. Werncke, S. Hogiu, M. Pfeiffer, A. Lau; „Strong S_1-S_2 vibronic coupling and enhanced third order hyperpolarizability in the first excited singlet state of diphenylhexatriene studied by time-resolved CARS“, *J. Phys. Chem. A* **104 (**2000) 4211-4217
- S. Hogiu, W. Werncke, M. Pfeiffer, T. Elsaesser; „Mode specific vibrational kinetics after intramolecular electron transfer studied by picosecond anti-Stokes Raman spectroscopy“, *Chem. Phys. Lett.* **312** (1999) 407
- S. Hogiu; W. Werncke, M. Pfeiffer, J. Dreyer, T. Elsaesser; „Mode specific vibrational excitation and energy redistribution after ultrafast intramolecular electron transfer“, *J. Chem. Phys.* **113** (2000) 1587
- S. Hogiu, J. Dreyer, M. Pfeiffer, K.-W. Brzezinka, W. Werncke; „Vibrational analysis and excited state geometrical changes of betaine-30 derived from Raman and infrared spectra combined with ab initio calculations“, *J. Raman Spectrosc.* **31** (2000) 797

Contents

1. Introduction *1*

1.1. Vibronic coupling in polyene-like molecules **2**

1.2. Photoinduced electron transfer in condensed phase **3**

1.3. Outline of the thesis **3**

References *5*

2. Theoretical background *7*

2.1. Vibronic coupling in organic molecules **7**
2.1.1. The Born-Oppenheimer adiabatic representation 7
2.1.2. Vibronic interactions and vibronic constants 9
2.1.3. Symmetry selection rules 9
2.1.4. The Jahn-Teller theorem 10

2.2. Time-dependent formalism for absorption and Raman scattering **12**
2.3.1. Milestones in understanding of ET mechanism in solution 14
2.3.2. The classical Marcus theory of ET 15
2.3.3. Inner-sphere versus outer-sphere ET 16
2.3.4. Adiabatic versus nonadiabatic ET 18
2.3.5. Microscopic ET rates using the Fermi's Golden Rule 19

References *21*

3. Experiment *23*

3.1. Theoretical considerations of the experiments **23**
3.1.1. Introduction 23
3.1.2. Raman scattering 23
3.1.3. Coherent Anti-Stokes Raman Scattering (CARS) 26
3.1.4. Second Harmonic Generation (SHG) 30
3.1.5. Stimulated Raman Scattering (SRS) 31
3.1.6. The pump-probe technique 33

3.2. Experimental set-up **34**
3.2.1. Generation of the picosecond laser pulses 34
3.2.2. CARS set-up 36
3.2.3. Raman set-up 37
3.2.4. Measuring of the time resolution in the experiment 38

References *41*

4. Vibronic coupling in the first excited singlet state of DPH *43*

4.1. Motivation **43**

4.2. Photophysics of DPH **45**

4.3. Results **47**
4.3.1. Raman spectra in ground state and time-resolved CARS spectra in excited states 47
4.3.2. Depolarization ratios of the Raman vibrations 50
4.3.3. Background free CARS measurements 52
4.3.4. Kinetics of the CARS spectra 56

4.4. Discussion **57**
4.4.1. Molecular geometry and assignment of the Raman frequencies in the ground and excited states 57
4.4.2. Bond order equalization in the first and second excited state 58
4.4.3. Origin of the Raman resonances 60
4.4.4. Mechanisms of vibronic coupling 61

4.5. Conclusions **67**

References ***69***

5. Mode specific vibrational kinetics after intramolecular electron transfer in Betaine-30 ***71***

5.1. Motivation **71**

5.2. Absorption spectra and photophysics of the molecule **73**

5.3. Stationary vibrational spectra and ab initio calculations of geometry and vibrational spectra. **76**

5.3.1. Stationary Stokes-Raman and infrared spectra 76
5.3.2. Molecule geometry in ground and excited electronic state 79
5.3.3. Assignment of the Raman vibrations 82
5.3.4. Discussion of the dispersion effects 84
5.3.5. Overtones and combination tones 84

5.4. Transient spectra and a view into the mechanism of back-ET **85**

5.4.1. Kinetics of the anti-Stokes Raman modes in slowly and fast relaxing solvents 86
5.4.2. Selective excitation of the vibrations and IVR after back-ET 89
5.4.3. Nonequilibrium vibrational populations of B-30 after back-ET 91
5.4.4. Transient Stokes-Raman spectra in the first excited electronic singlet state 94

5.5. Conclusions **98**

References ***101***

6. Summary ***103***

6.1. Vibronic coupling in DPH **103**

6.2. Back-ET in B-30 **103**

References ***105***

Appendix 1 ***107***

Zusammenfassung ***109***

1. Introduction

Electronic photoexcitation of a molecular system initiates a complex sequence of dynamical and kinetical processes in which the molecule can either change or preserve its chemical identity. The processes are called photophysical if the chemical identity of the molecule is preserved, and photochemical if not. Frequently, the nuclei do not move on a single adiabatic electronic potential energy surface, but transit between different adiabatic potential surfaces. In such transition points (actually hypersurfaces in the multidimensional nuclear coordinate space) of exact degeneracy of adiabatic potential energy surfaces, also called conical intersections, the Born-Oppenheimer approximation breaks down, and vibronic coupling related to these nonadiabatic events occurs [1-6]. Photodissociation, charge-transfer, isomerization, and spin-changing reactions are, generally speaking, typical examples of events occurring at conical intersections [7]. In particular, in the mechanism of vision and photosynthesis, a sequence of processes taking place at conical intersection occur.

Photophysical and photochemical processes cover a wide range of timescales. They can be very slow, like the oxidation of iron in air, which can take even years, or very fast, like the photoisomerization of the visual pigment rhodopsin, which occurs in femtoseconds [8]. New developments of picosecond and femtosecond laser technology allow a view into the ultrafast photochemical and photophysical processes which occur on the timescale of a period of the nuclear vibration. Conversion of light energy into chemical energy in photosynthesis and vision can thus be studied on a real time scale. The knowledge gained from these studies can be used, for example, for developing materials and components for artificial photosynthesis. Controlling chemical reactions could become reality and new chemical components with new properties could be obtained. Developing fast electronic components based on light-driven processes is another important direction of studies using picoseconds and femtosecond methods.

Nonadiabatic interactions have long been known in molecular spectroscopy as being responsible for spectral perturbations, Jahn-Teller and Renner-Teller effects [6, 9]. The role of conical intersections as funnels for radiationless decay has also been recognized [10]. There are three aspects related to the mechanism of the processes induced by conical intersection(s) [4]: (i) the path to the conical intersection(s) on the electronically excited potential energy surface, (ii) the nonadiabatic transition near the conical intersection(s), which is determined by the geometrical structure of the conical intersection(s) and provides the opportunity for branching to different regions of the ground state potential energy surface, i.e. for multiple products, and (iii) the subsequent motion on the ground state potential energy surface.

This thesis deals with photophysical elementary processes occurring at/near conical intersections. The interactions responsible for them are strong intramolecular couplings. Among them, strong electron-vibration interactions (gradients of excited state potential energy surfaces with respect to the Condon active normal modes) is the key for photoisomerization (see paragraph 1.1), and strong mode-mode couplings play an important role in the ultrafast radiationless decay (paragraph 1.2).

1.1. Vibronic coupling in polyene-like molecules

Photoisomerization of polyene-like molecules (see Fig. 1.1 for the structure of polyene-like molecules) such as rhodopsin and bacteriorhodopsin is of great importance for the role they play in the nature. They exploit the high efficiency and speed of cis-trans isomerization about polyene double bonds for signal transduction [8, 11]. Another role of polyenes in nature is light-harvesting involving singlet-singlet energy transfer from carotenoids to chlorophylls and bacteriochlorophylls as well as photoprotection by quenching the triplet state of either chlorophyll or bacteriochlorophyll. These properties are believed to arise, at least partially, from the interaction of two energetically close lying excited electronic states [12]. The nature of this interaction is still the subject of many studies. Its understanding requires elucidation of the coupling mechanism between these two excited states.

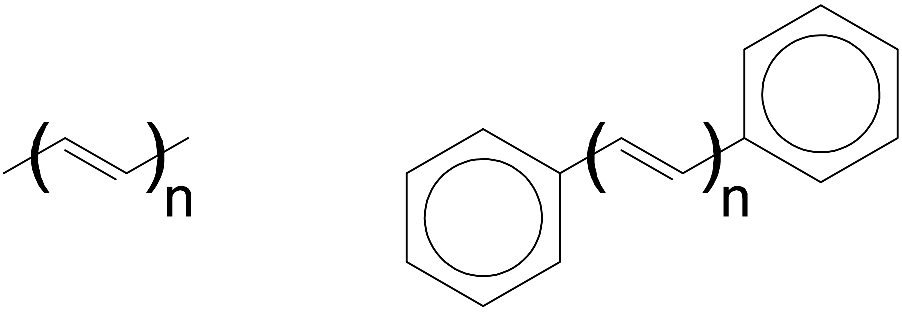

Fig. 1.1: Polyene sequence (left) and diphenylpolyene (right) general structure. By increasing n, longer (diphenyl)polyene chains are obtained.

A great number of experimental and theoretical work has been done to describe the spectroscopic properties and to identify the electronic states of polyenes ([13-15] and references therein). In particular, the coupling mechanism between their excited states has been a main topic in the last years. Ultrafast radiationless decay of the optically bright B excited state into the dark A excited state in trans-butadiene has been explained by a vibronic-coupling model describing the conical intersection of the A and B states [16]. Woywod et. a. developed a model of vibronic coupling in the first two excited states of trans-hexatriene [17]. Nevertheless, experimental work on this topic is scarce.
Time-resolved Raman or Coherent Anti-Stokes Raman Scattering (CARS) spectroscopy are powerful methods to study the role of vibrational modes in coupling between the two excited electronic states of polyenes and diphenylpolyenes. They enable to monitor the formation of photoproducts as a function of time, and to determine the specific modes responsible for vibronic coupling. One goal of this thesis is the study of the mechanism of electron-vibration interaction in excited states of a polyene-like molecule, diphenylhexatriene. A time-resolved picosecond CARS spectrometer has been constructed to determine the changes and instabilities in molecular structure due to vibronic coupling.

1.2. Photoinduced electron transfer in condensed phase

Electron transfer (ET) reactions represent an elementary chemical process which occurs in a large variety of molecules, ranging from small ion pairs up to large biological systems. ET can be optically or/and thermally activated and triggers photosynthesis, metabolism, polymerization reactions, electrochemical reactions, etc. Understanding and control of electron transfer reactions comprises one of the broadest and most active research areas of physical chemistry [18-20]. Photoinduced ET occurs in nature in connection with energy transduction. Many coupled ET events in photosynthesis and respiratory chain are crucial to the respective function. The kinetics of specific charge-transfer processes dictate the efficiency of photosynthetic and energy conversion systems (natural or artificial). The overall rates of ET are determined by intramolecular mechanisms as well as by the response of the environment to the photoinduced changes of the charge distribution [18]. The intramolecular mechanisms include redistribution of electronic charge and relevant vibrational excitations due to electron-vibrational interactions described by the interaction Hamiltonian H_{if} in Fig. 1.2. Excitation of high-frequency molecular vibrations could be the basic physical mechanism allowing to control ET. However, few experiments have been performed to identify the strongly contributing modes and the research is still at the beginning.

Because Resonance Raman spectroscopy is very sensitive to the vibrational modes with high Franck-Condon factors, it allows to monitor directly the relevant coupling modes in the ET process. This method gives thus an insight into the ET mechanism. The goal of this study is to determine the role of vibrational modes in the back-ET reaction in Betaine-30 (B-30). A highly sensitive time-resolved picosecond Raman spectrometer has been developed for this purpose.

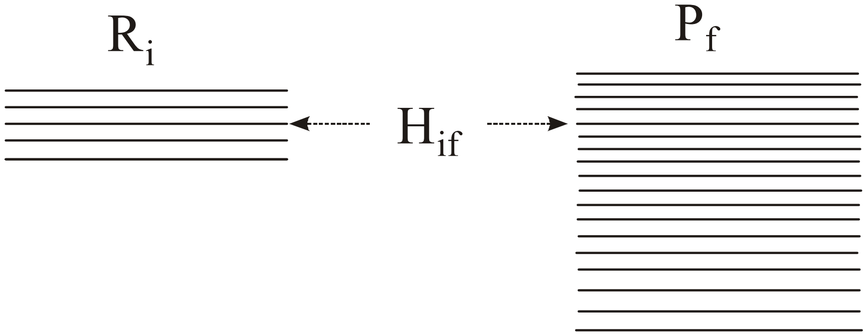

Fig. 1.2: Schematic diagram of vibrational excitation of high frequency modes of the product during ET. Electron-vibrational coupling described by the Hamiltonian H_{if}, and vibrational manifold of the reactant R (i) and product P (f) are also shown.

1.3. Outline of the thesis

Chapter 2 contains the theoretical background that is used for the interpretation of the experimental results. Mechanisms of vibronic coupling in organic molecules will be discussed, followed by the introduction of the time-dependent approach of light-matter interaction. In addition, a review of the models used most frequently in describing ET processes will be presented.

In Chapter 3, general considerations of the experiments will be presented, including the Raman effect, Coherent Anti-Stokes Raman Scattering (CARS) and the pump-probe technique. The picosecond Raman/CARS experimental set-up consisting of a 50 Hz amplified dye laser and a highly sensitive detection system will also be described in detail.

In Chapter 4 a study of the vibronic coupling between the first and second excited electronic states of diphenylhexatriene (DPH) will be presented. This should offer the possibility to gain new information about the relaxation mechanism between the excited states of polyenes and about their role in the intermolecular energy transfer in photosynthesis.
First, some photophysical properties of the molecule will be introduced. Secondly, the experimental results of the CARS measurements after excitation in the optically allowed excited state will be presented. Based on the CARS spectra of the excited states and semiempirical calculations, the changes of molecular geometry in the excited state will be discussed. These information reveal a new effect of vibronic coupling between the two excited states. Two mechanisms of vibronic coupling will be finally discussed.

In Chapter 5 a study of the mode specific vibrational kinetics after intramolecular back-ET in B-30 will be reported. This will enable us to determine the role of the vibrational modes in back-ET and subsequent relaxation.
The importance of the work is discussed in a general context, followed by the presentation of stationary and transient Raman spectra. These spectra allow to discern the acceptor modes in the back-ET process. The transient spectra give evidence of selective vibrational excitation and nonequilibrium vibrational population for a few ps after back-ET. The interplay between vibrational excitation and intramolecular vibrational relaxation will be discussed. Quantum-chemical calculations will be presented, which allow to assign most of the observed vibrational frequencies.

Chapter 6 contains final conclusions and remarks.

References

[1] M. Klessinger, J. Michl, in *„Excited states and photochemistry of organic molecules"*, VCH Publishers, New York (1995)

[2] M. Klessinger, *Angew. Chem. Int. Ed. Engl.* **34** (1995) 549

[3] M. Olivucci, F. Bernardi, S. Ottani, M. A. Robb, *J. Am. Chem. Soc.*, **116** (1994) 2034

[4] M. Klessinger, *Pure § Appl. Chem.*, **69** (1997) 773

[5] Von H. Köppel, L. S. Cederbaum, W. Domcke, S. S. Shaik, *Angew. Chem.*, **95** (1983) 221

[6] W. Domcke, G. Stock, *Adv. in Chem.Phys.*, Eds. I. Prigogine and S.A. Rice, **100** (1997) 1

[7] J. Michl, A. Bonacic-Koutecky, in *„Electronic aspects of organic photochemistry"*, Wiley-Intrescience publication, New York (1990)

[8] L. A. Peteanu, R. W. Schoenlein, Q. W. Wang, R. A. Mathies, C. V. Shank, *Proceedings of the National Academy of Sciences* **90** (1993) 11762-11766

[9] I. B. Bersuker, in *„The Jahn-Teller effect and vibronic interactions in modern chemistry*", Ed. John P. Fackler, Plenum Press, New York and London (1984)

[10] G. Herzberg, in *„Electronic spectra and electronic structure of polyatomic molecules"*, New York (1966)

[11] Q. Wang, R.W. Schoenlein, L.A. Peteanu, R.A. Mathies and C.V Shank, *Science* **266** (1994) 422-24

[12] B. S. Hudson and B. E. Kohler, *J. Chem. Phys.* **59** (1973) 4984

[13] *„The photochemistry of carotenoids"*, Ed. H. A. Frank, *Adv. in Photosynthesis*, **8** (1999)

[14] G. Orlandi, F. Zerbetto, M. Z. Zgierski, *Chem. Rev.*, **91** (1991) 867

[15] B. E. Kohler, *J. Chem. Phys.*, **93** (1990) 5838

[16] R. P. Krawczyk, K. Malsch, G. Hohlneicher, R. C. Gillen, W. Domcke, *Chem. Phys. Lett.* **320** (2000) 535–541

[17] C. Woywod, W. C. Livingood, J. H. Frederick, *J. Chem. Phys.*, **112** (2000) 613

[18] *„Electron Transfer From Isolated Molecules To Biomolecules"*, Parts 1 and 2 *Advances in Chemical Physics*; M. Bixon, J. Jortner, Eds.; Wiley: New York,; Vol. **106** and **107** (1999)

[19] P. Y. Chen, T. J. Meyer, *Chem. Rev.* **98 (**1998) 1439

[20] P. F. Barbara, T. J. Meyer, M. A. Ratner, *J. Phys. Chem.* 100 (**1996)** 13148.

2. Theoretical background

2.1. Vibronic coupling in organic molecules

Vibronic coupling is of great importance in spectroscopy. One can discern three main areas where vibronic coupling plays a major role. First, the absorption and emission of light are determined by the overlap of the vibrational wavefunctions of the initial and final states, as visualized in the „vertical“ Franck-Condon principle. When the equilibrium geometries of the molecule in the states involved in transition are similar, i.e., small lateral displacements of the potential energy surfaces, and the force constants, i.e., the curvatures, are similar, the vibronic overlap between the two states is large and the transition is Franck-Condon allowed. Secondly, vibronic coupling determines the distortion introduced by degenerate electronic states. Thirdly, nonadiabatic radiationless transitions between states of different symmetry occur through vibronic coupling and are very important in photophysics.

The main aim of this paragraph is to present in the problem of vibronic coupling in polyatomic molecules in the presence of electronic degeneracy.

The idea of vibronic coupling and instability in a degenerate electronic state has first been formulated by Landau and Teller in 1934 (see for a reference [1]) and shown to be true for all nonlinear molecular systems by Jahn and Teller as formulated in the well-known Jahn-Teller theorem [2]. This effect is present in all situations where the electrons do not adiabatically follow the motion of the nuclei. Consequently, the nuclear positions are determined not only by the averaged field of the electrons, but also by the details of the electronic structure and their changes under nuclear displacements. This is always the case if electronic degeneracy is present.

2.1.1. The Born-Oppenheimer adiabatic representation

Consider an isolated molecule which has no interaction with any external field. The structure and the properties of this molecular system are determined by the motion of its electrons and nuclei and by their interaction. The main laws governing these motions have been discovered in the early thirties. However, because of mathematical difficulties, the quantum-mechanical treatment of molecular structures in most cases can be carried out only if some simplifying approximations (which are physically justified) are introduced. The most general of them is the Born-Oppenheimer adiabatic approximation which separates the time-scales of the electronic and nuclear motions.

The origin of the adiabatic approximation is the fact that the nuclear mass much larger than the mass of the electron (the nuclear mass of the H atom is 1837 times the electronic mass). Consequently, the electron velocity is much larger than that of the nucleus. Therefore, it can be assumed that every instantaneous (fixed) position of the nuclei corresponds to a stationary electronic state, and the motions of the nuclei are governed by the average field of the electrons. In other words, the nuclei are moving on a potential energy surface (PES) in the space of nuclear coordinates.

Under this assumption the Schrödinger equation can be solved in two stages [3]:

(i) first, solving the electronic part of the problem by ignoring the nuclear motion,

(ii) secondly, using the mean electronic energy as the potential for the nuclear motion.

The total Hamiltonian that enters into the Schrödinger equation is:

$$H = H_r + H_Q + V(r,Q) \qquad (2.1)$$

where H_r is the electronic component including the kinetic energy, H_Q is the kinetic energy of the nuclei, and $V(r,Q)$ is the energy due to interaction of the electrons with the nuclei and the nuclear repulsion (r and Q are the whole set of coordinates of electrons r_i and nuclei Q_α, respectively).

The operator $V(r,Q)$ can be expanded as a series of small displacements of the nuclei about an origin point $Q_\alpha = Q_{\alpha 0} = 0$:

$$V(r,Q) = V(r,0) + \sum_\alpha \left(\frac{\partial V}{\partial Q_\alpha} \right)_0 Q_\alpha + \frac{1}{2} \sum_{\alpha,\beta} \left(\frac{\partial^2 V}{\partial Q_\alpha \partial Q_\beta} \right)_0 Q_\alpha Q_\beta + ... \qquad (2.2)$$

$V(r,0)$ is the potential energy of the electrons in the field of fixed nuclei.

One can solve the electronic part of Schrödinger equation (stage (i)):

$$\left[H_r + V(r,0) \right] \varphi_k(r) = \varepsilon_k' \varphi_k(r) \qquad (2.3)$$

and obtain a set of eigenvalues (energies) ε_k' and eigenfunctions (wave functions) $\varphi_k(r)$ for a given nuclear configuration.

Now the question is how these solutions vary under nuclear displacements. Solving the full Schrödinger equation for different Q, one can obtain the PES's (stage (ii)).

The total Schrödinger equation is:

$$H\Psi(r,Q) = E\Psi(r,Q) \qquad (2.4)$$

The total wavefunction is expanded in terms of electronic wavefunction:

$$\Psi(r,Q) = \sum_k \chi_k(Q) \varphi_k(r) \qquad (2.5)$$

Substituting equation (2.5) in equation (2.4) a set of coupled equations for the nuclear wave-functions χ_k will be obtained:

$$\left[H_Q + \varepsilon_k(Q) \right] \chi_k(Q) + \sum_{m \neq k} W_{km}(Q) \chi_m(Q) = E \chi_k(Q) \qquad (2.6)$$

where $W_{km}(Q)$ is the electronic matrix element of vibronic interaction which depend on Q and is called vibronic coupling constant:

$$W(r,Q) = V(r,Q) - V(r,0) = \sum_i \left(\frac{\partial V}{\partial Q_i} \right)_0 Q_i + \frac{1}{2} \sum_{i,j} \left(\frac{\partial^2 V}{\partial Q_i \partial Q_j} \right)_0 Q_i Q_j + ... \qquad (2.7)$$

$$\text{and } \varepsilon_k(Q) = \varepsilon_k' + W_{kk}(Q) \qquad (2.8)$$

is the potential energy of the nuclei in the average field of the electrons in state $\varphi_k(r)$.

If second- and higher-order terms are neglected, W_{km} may be further explicitly written as:

$$W_{km} = \sum_i \langle k | \frac{\partial V}{\partial Q_i} | m \rangle Q_i \qquad (2.9)$$

For $W(r,Q)=0$ (i.e. no vibronic mixing) it is easy to see that the set of equations (2.6) transforms into a simple set of equations:

$$\left[H_Q + \varepsilon_k(Q) \right] \chi_k(Q) = E \chi_k(Q) \qquad (2.10)$$

which represents the Schrödinger equation for the nuclei moving in the mean field of the electrons in state $\varphi_k(r)$. In other words this is the adiabatic or Born-Oppenheimer approximation. It can be shown [3] that the perturbation of the total wave function by vibronic mixing is negligible if:

$$\hbar\omega << \left|\varepsilon_m{}'-\varepsilon_k{}'\right| \qquad (2.11)$$

where the term on the left side is the energy quantum of vibrations in the electronic state under consideration (*k* or *m*) and $\varepsilon_m{}'$ and $\varepsilon_k{}'$ represents the energy levels *m* or *k*.

Equation (2.11) is a good criterion to discern whenever the adiabatic approximation can be applied. If this criterion is fulfilled, the error induced by the adiabatic approximation is of the order of $(m/M)^{1/2}$, where m and M are the electronic and nuclear masses, respectively.

2.1.2. Vibronic interactions and vibronic constants

Consider now a molecular system where two electronic states are degenerate or at least near-lying (pseudo-degeneracy). In this case, criterion (2.11) is not satisfied and vibronic mixing described by the operator (2.7) plays a significant role in describing the molecular properties.

To start the problem of vibronic coupling, Eq. (2.3) is solved for fixed nuclei, in order to determine the electronic levels and to find the electronic degeneracies. Then, Eq. (2.10) has to be solved in the normal coordinates of the molecule, to determine the frequencies of the normal modes. Finally, the matrix elements $\langle k|\frac{\partial V}{\partial Q_i}|m\rangle Q_i = \alpha_{km}$ of the coupling operator in Eq. (2.9) (called vibronic coupling constants) are calculated. They characterize the measure of coupling between the electronic structure and nuclear displacements, i.e. the measure of influence of the nuclear displacements on the electron distribution and, conversely, the effect of the changes in the electronic structure upon nuclear dynamics [3]. The first term in Eq. (2.7) is the linear vibronic constant and the second term is the quadratic vibronic constant, etc. In most cases, it is enough to take into account the linear and quadratic terms in order to reveal the vibronic effects. The linear vibronic constants have a clear physical meaning: they represent the force α (see Eq. (2.9)) with which the electrons affect the nuclei.

One of the effects of vibronic mixing is the appearance of anharmonicity in the potential energy surfaces of molecules, which has the origin in the existence of higher terms in the expansion (2.2).

2.1.3. Symmetry selection rules

The symmetry selection rule states that a transition or vibronic coupling is allowed only if the direct product of the representations involved in the process includes the fully symmetric species of the molecular point group: $\Gamma_{\Psi_i} \otimes \Gamma_\alpha \otimes \Gamma_{\Psi_f} \supset \Gamma_s$. Here, Γ_{Ψ_i}, Γ_α, Γ_{Ψ_f} and Γ_s are the representations of the initial, transition (coupling), final and fully symmetric species.

The consequences that can be derived for Raman and electronic transitions, and for vibronic coupling will be discussed in the following.

Because the ground state wave function is usually fully symmetric, the Raman activity of a transition will be determined by the symmetry properties of the polarizability tensor components and of the vibrational wave function of the final state. If they belong to the same symmetry species, the full direct product of the transition will be symmetric and the transition is Raman active.

For an electronic transition, the direct product between the two electronic wave function and that of the transition dipole moment vector component should be totally symmetric. The ground state wave function is, as mentioned, totally symmetric. For molecules possessing a center of symmetry, it belongs to the gerade representation since it is not affected by inversion operation with respect to the center of symmetry. The dipole moment, however, changes its sign when the inversion operation is made. Consequently, it belongs to the ungerade representation. The electronic transition is thus allowed only if the excited state wave function belongs to the ungerade representation.

In the case of Diphenylhexatriene (n=3 in Fig. 1.1 right), which belongs to the C_{2h} point symmetry group (two C_2 axes and an inversion centrum), the ground and the first excited singlet state is of A_g symmetry and the second excited state of B_u symmetry. The Mulliken notation A and B for nondegenerate electronic states has been used [4].

This labeling scheme of the irreducible representations provides some additional information about their symmetry properties. All one-dimensional representations are labeled with A (for symmetric irreducible representations) or B (for antisymmetric irreducible representations). If a center of symmetry is present in a molecule, then g or u are used as a subscript to identify gerade (g) or ungerade (u) irreducible representations.

The consequence that can be derived from the symmetry selection rules in the case of Diphenylhexatriene is that only the transition from the ground state to the second excited singlet state (of B_u symmetry) is allowed.

The same selection rule applies for vibronic coupling between electronic states. The total vibronic and electronic symmetry must be examined. At this point it is important to mention that only nontotally symmetric displacements Q_i can contribute to the matrix elements W_{km}, since the totally symmetric displacements do not change the symmetry and hence do not remove the degeneracy (considered as due to the symmetry of the system). Consequently, coupling between A_g and B_u electronic states in Diphenylhexatriene can only be made by nonsymmetric b_u vibrations.

2.1.4. The Jahn-Teller theorem

Jahn and Teller proved that any nonlinear molecule in an orbitally degenerate electronic state will always distort in such a way as to lower the symmetry and remove the degeneracy [2].

The Jahn-Teller theorem is based on the analysis of the behavior of the adiabatic potentials of a polyatomic system near the point of electronic degeneracy. They showed [2, 4] that if the adiabatic potentials of a nonlinear polyatomic system have a n-fold degeneracy, at least one of them has no minimum at this point.

Suppose now that by solving Eq. (2.3) for nuclei fixed at the point $Q_i=Q_i^0=0$ a n-fold degeneracy is obtained with energies $\varepsilon_k'=\varepsilon_0$. The question is how do these energy levels vary under nuclear displacements? In other words, how do the adiabatic potentials $\varepsilon_k(Q)$ look like for displaced coordinates with respect to the $Q_i=0$ point? They can be obtained by estimating the effect of the vibronic interaction terms from Eq. (2.7) on the energy level positions ε_k' determined with Eq. (2.3). Starting from the total Hamiltonian, the secular equation is solved:

$$\begin{vmatrix} W_{11}-\varepsilon_k(Q) & W_{12} & . & W_{1n} \\ W_{21} & W_{22}-\varepsilon_k(Q) & . & W_{2n} \\ . & . & . & . \\ W_{n1} & W_{n2} & . & W_{nn}-\varepsilon_k(Q) \end{vmatrix} = 0 \qquad (2.12)$$

where $W_{km}(k \neq m)$ are given by (2.7). Assuming small displacements, second- and higher-order terms in (2.7) may be omitted and $W_{km}=\sum_i \alpha_{km}Q_i$. Here α_{km} are the vibronic coupling constants, k and m are the degenerate electronic levels, and Q_i are the modes along the displacements are made.

If at least one of $W_{km}(k \neq m)$ is nonzero, at least one of the roots ε_0 of Eq. (2.12) contains linear terms in the appropriate displacements Q_i. Consequently, the adiabatic potential $\varepsilon_k(Q)$ has no minimum at the point $Q_i=Q_i^{\,0}=0$ with respect to these displacements. This is illustrated in Fig. 2.1a for a two-fold degeneracy.

$\varepsilon_k(Q)$ loses here the meaning of potential energy of the nuclei in the mean field of the electrons, since the motions of the electrons and nuclei near the point of degeneracy cannot be separated.

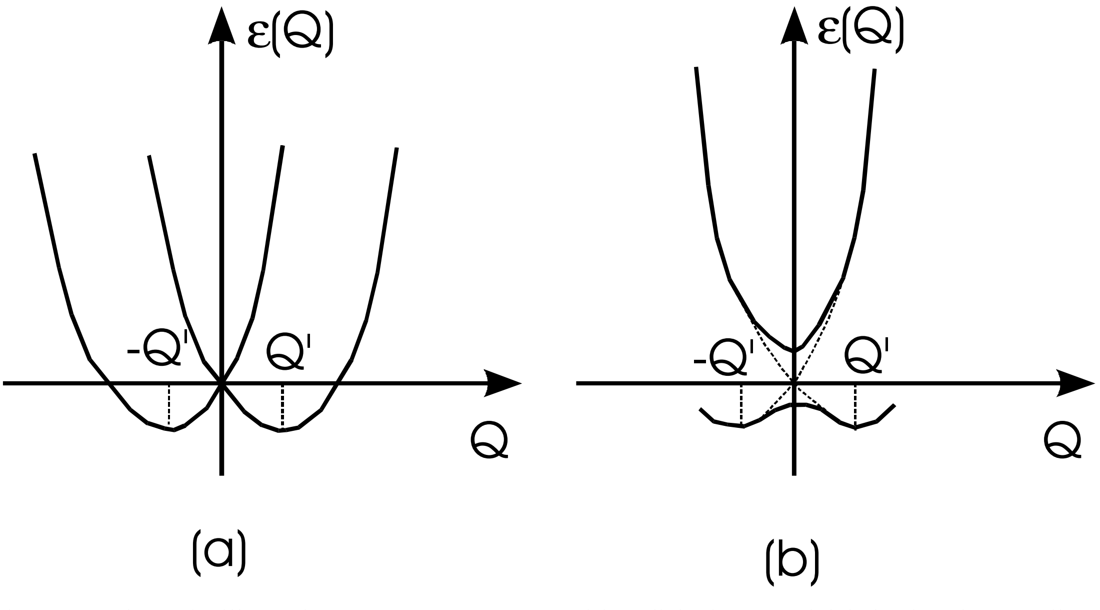

Fig. 2.1: Schematic illustration of two types of specific adiabatic potential behavior due to vibronic interactions: (a) Jahn-Teller effect in case of electronic degeneracy; (b) pseudo-Jahn-Teller effect in case of pseudo-degeneracy.

For linear molecules, the nontotally symmetric displacements are described as ungerade with respect to reflection, whereas the product of wave functions of the degenerate terms (coming from symmetry considerations) is always gerade with respect to the same symmetry operation. Consequently, all the linear $W_{km}(k \neq m)$ terms are zero, and only the quadratic terms in Eq. (2.7) could play a role. This effect is called Renner effect [6].

If the energy levels do not cross at Q_i=0 but they are very closely spaced, the molecule is still unstable in the sense of Jahn and Teller, and the terminology used is pseudo-Jahn-Teller effect. This is illustrated in Fig. 2.1b.

The (pseudo) Jahn-Teller vibronic coupling effect can be described by a model Hamilton operator H. This operator takes the form of a *n*x*n* matrix in the case of *n*-fold degeneracy. In the simplest case of two-fold degeneracy, H becomes:

$$\mathrm{H}=\begin{pmatrix} H_{11} & H_{12} \\ H_{21} & H_{22} \end{pmatrix} \qquad (2.13)$$

where the diagonal elements correspond to the pure adiabatic states, and the non-diagonal elements give the coupling between the two states.

2.2. Time-dependent formalism for absorption and Raman scattering

In the precedent paragraph only stationary states of the molecule and their coupling were presented, without taking time-dependent phenomena into account.

For an analysis of the processes related to relaxation and dissipation of energy let us assume that a system S is excited with a very short pulse (see Fig. 2.2). After excitation, the system S will relax and dissipate the excitation energy to the environment E. The relaxation is here regarded as an internal process of energy redistribution along the internal degrees of freedom of the system. In contrast, dissipation is activated by the coupling to the external degrees of freedom and is associated with unidirectional flow of excess energy into the surroundings. In most cases, the environment E is a macroscopic system and will not increase its internal energy considerably.

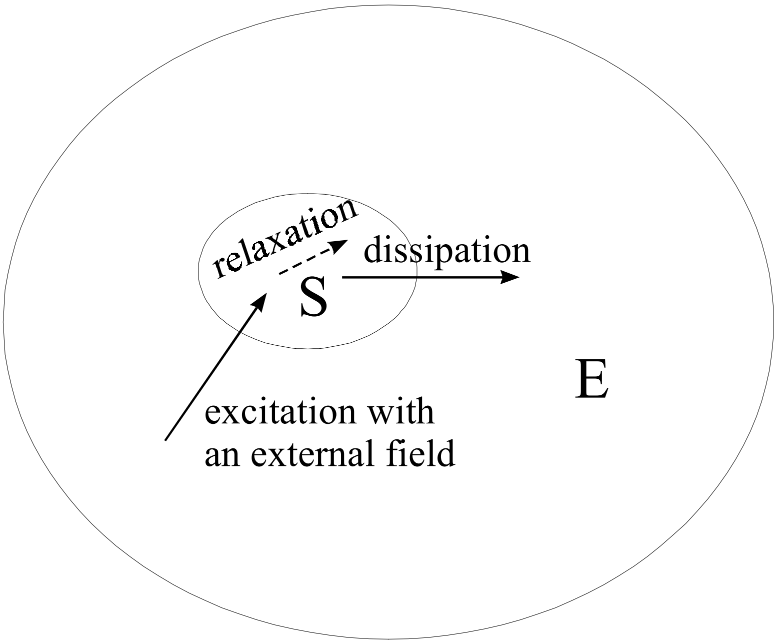

Fig. 2.2: Schematic view of physical processes that can take place after excitation with an external field.

The processes related to absorption, relaxation and dissipation have been treated within a variety of theoretical models. One of the most frequently used is the time-dependent semiclassical theory developed by Heller about twenty years ago [7], which neglect the dissipation processes.

The advantage of this theory is that it offers an intuitive picture of absorption, emission and Raman scattering in terms of nuclear wave packet movement on the potential surfaces. The wave packet dynamics corresponds to some specific vibrational motion that can be visualized like bond distances, angles, etc.

Let us take two adiabatic potential energy surfaces, each relevant for two vibrational degrees of freedom, x and y. Within the Born-Oppenheimer approximation one can write the vibrational wave function in the ground state $\chi(x,y)$ and vertically above it the wavefunction

$$\phi(x,y) = \mu(x,y) \cdot \chi(x,y) \qquad (2.14)$$

with $\mu(x,y)$ the electronic transition moment between the two surfaces. The vertical transition is known as a Franck-Condon transition, and can be understood as an almost instantaneous electronic transition, while the nuclei retain their position and momentum. The transition can be induced by photoexcitation, for example. After the electrons have made a transition, the nuclei experience new forces. They find themselves displaced relative to the equilibrium geometry in the new potential surface and will be the subject of specific dynamics. In other words, the wave packet on the upper potential surface $\phi(x,y)$ is a displaced non-stationary one, which will evolve according to the time-dependent Schrödinger equation:

$$i\hbar \frac{\partial \phi(t)}{\partial t} = H\phi(t) \qquad (2.15)$$

where H is the vibrational Hamiltonian for the upper surface

The absorption spectrum is:

$$\varepsilon(\omega) = C\omega \int_{-\infty}^{\infty} e^{i(\omega+E_0)t} \langle \phi(0) | \phi(t) \rangle dt \qquad (2.16)$$

where C is a constant, ω is the frequency of the incident radiation, and E_0 is the energy of χ. In this way, the absorption spectrum is the Fourier transform of the overlap $\langle \phi(0) | \phi(t) \rangle$. The overlap of the constant ground state wave function (at $t = 0$) with the time dependent wave function in the excited state give rise to minima and maxima (they interfere constructively or destructively) specific for each vibrational motion. Usually, a very broad absorption spectrum is observed, due to the time-energy Uncertainty Principle where the broadest feature in the spectrum comes from the shortest feature in the time. For a downfall of the wave packet $\phi(t)$ with a time constant T_1, the corresponding envelope will have the width $\Delta\omega = 1/T_1$. Spreading and dissociation of the wave packet at later times contribute to its progressive amplitude lowering, which determine the substructure in the absorption spectrum.

In the Raman scattering process, the intensity is related to the square of the polarizability α which can be defined in the time-dependent formalism like:

$$\alpha_{0\to n}(\omega) = \int_{0}^{\infty} e^{(i\omega-\Gamma)t} \langle \phi_n(0) | \phi(t) \rangle dt + \text{(nonresonant term)} \qquad (2.17)$$

where $|\phi_n\rangle = \mu|\chi_n\rangle$ is the wave function of the final state n obtained by the multiplication of the wave function of the initial state χ with the transition moment μ and Γ is a damping factor which represents the effect of dephasing due to coupling to other degrees of freedom not explicitly included in the wave functions ϕ_n. By comparing Eq. (2.17) with Eq. (2.16), it should be noted that the same dynamics of the same wave packet $\phi(t)$ is involved in both absorption and Raman scattering, but different final states ϕ_n are involved.

2.3. A formalism for ultrafast electron transfer in condensed matter

Electron transfer (ET) is one of the most common reactions in both chemistry and biology, especially in the form of oxidation and reduction reactions. The ET process is, like any other chemical reaction, a transition from a metastable initial state to a stable final state. The initial state can be prepared in two different ways: photoabsorption or electron injection from external sources. The subsequent ET causes a redistribution of the electrostatic field in the molecule, which leads to a new equilibrium configuration of the nuclei. The interplay between the ET and the accompanying nuclear rearrangement is the key to understand the mechanism of ET. Because the ET reaction occurs in an environment which can play an active role in the reaction, the influence of the specific medium has to be taken into account.

The main aim of this chapter is to present a theoretical background of the ET theory from the classical Marcus theory to the quantum-mechanical theories describing the role of intramolecular vibrations in the ultrafast ET reactions.

2.3.1. Milestones in understanding of ET mechanism in solution

The first observation of ET reactions in solution goes back in the nineteenth century, when Humphry Davy observed (1808) that passing ammonia over metallic potassium produces a fine blue color. The modern experimental basis for ET reactions in solutions began 1920 with studies of ionic oxidation reduction reactions. The understanding of ET process has been considerably improved by Franck and Libby in 1949 [8]. They showed that ET transfer rates in solution are determined by horizontal Franck-Condon factors, in analogy to radiative processes where the transition probabilities are determined by vertical Franck-Condon factors. Between 1956-1960 R. A. Marcus made use of potential energy surfaces and statistical mechanics to provide a detailed classical description of the ET process [9-13]. He reduced the many-dimensional potential energy surfaces for reactants and products to harmonic free energy curves which were function of a single reaction coordinate. The so-called Marcus inverted regime was thus predicted (see the Paragraph 2.2.2) and later experimentally proved. The incorporation of quantum effects into the ET rate was advanced by Levich and Dogonadze [14, 15]. A theoretical description of the role of intramolecular vibrational excitations accompanying ultrafast ET reactions has been made by Jortner and Bixon [16, 17]. Currently, numerous groups of scientists are trying to understand the ET mechanism at a microscopic (vibrational) level and to explore the coherence phenomena related to the ET [18]. Another direction of recent interest is the possibility to control ET and to use molecules as „molecular wire“ [18].

2.3.2. The classical Marcus theory of ET

Consider a unimolecular ET reaction:

$$D^+A^- \underset{k_{-ET}}{\overset{k_{ET}}{\rightleftarrows}} D\,A$$

The transition occurs between the donor D and acceptor A assuming the „horizontal“ Franck-Condon principle, i.e. the nuclear configuration of the reactant and product species must be the same at the point of transition state and the internal energy is conserved. The reactant D^+A^- has a potential energy which is a function of many nuclear coordinates (including solvent coordinates), resulting in a multidimensional potential energy surface. A similar surface has the product DA. In transition state theory, a reaction coordinate is introduced, so that the potential energy surface can be reduced to one- or a few-dimensional profile.

Marcus showed [9-13] that if the system is represented in a Gibbs (free) energy space, the Gibbs energy profiles along the reaction coordinate can be approximated as parabolas. The parabolic free-energy surfaces as a function of the reaction coordinate are illustrated in Fig. 2.3 for a variety of conditions. The curvatures of the reactant and product are assumed to be the same. The parameters shown in the diagram are: λ, the reorganization energy, which represents the change in free energy if the reactant were distorted to the equilibrium configuration of the product without transferring the electron; ΔG_0 which is the difference in free energy between the equilibrium configurations of the reactant and product states (the driving force) and ΔG^* which corresponds to the free energy of activation for ET. It is important to make the distinction between the ΔG^* and ΔG^+ which is the experimental free energy obtained from thermodynamic considerations in transition state theory.

From analytical geometry of intersecting parabolas it follows that:

$$\Delta G^* = \frac{\left(\lambda + \Delta G_0\right)^2}{4\lambda} \qquad (2.18)$$

According to classical transition state theory, the first-order rate constant k_{ET} is given by:

$$k_{ET} = \kappa_{el} \upsilon_n \exp(-\frac{\Delta G^+}{k_B T}) \qquad (2.19)$$

where κ_{el} is the electronic transmission coefficient which is related to the transition probability at the intersection of the two surfaces as determined by the Landau-Zener theory [19, 20] ($\kappa_{el} = 1$, for adiabatic and $\kappa_{el} \approx V_{el}^2$ for nonadiabatic ET, with V_{el} defined as the electronic coupling constant - see also the next paragraph), υ_n is the frequency of nuclear passage through the transition state (typically 10^{13} s^{-1}), ΔG^+ is the experimental free energy of activation, k_B the Boltzmann constant and T the temperature. Inserting (2.18) in (2.19), the classical Marcus equation is obtained:

$$k_{ET} = \kappa_{el} \upsilon_n \exp\left[-\frac{(\lambda + \Delta G_0)^2}{4\lambda k_B T} \right] \qquad (2.20)$$

Eq. (2.20) indicates that for $-\Delta G_0 < \lambda$, by increasing $-\Delta G_0$ the ET rate k_{ET} increase. This is the normal regime (Fig. 2.3a). For $-\Delta G_0 = \lambda$, k_{ET} reaches its maximum $k_{ET} = \kappa_{el} \upsilon_n$ (Fig. 2.3b). For $-\Delta G_0 > \lambda$, increasing further $-\Delta G_0$ the ET rate k_{ET} decreases, and the inverted regime is obtained (Fig. 2.3c). The effect of decreasing k_{ET} in the inverted regime can be explained physically as follows: increasing the driving force $-\Delta G_0$ to values larger than the reorganization energy λ leads to the increasing of the free energy of activation ΔG^*, i.e. barrier of the reaction.

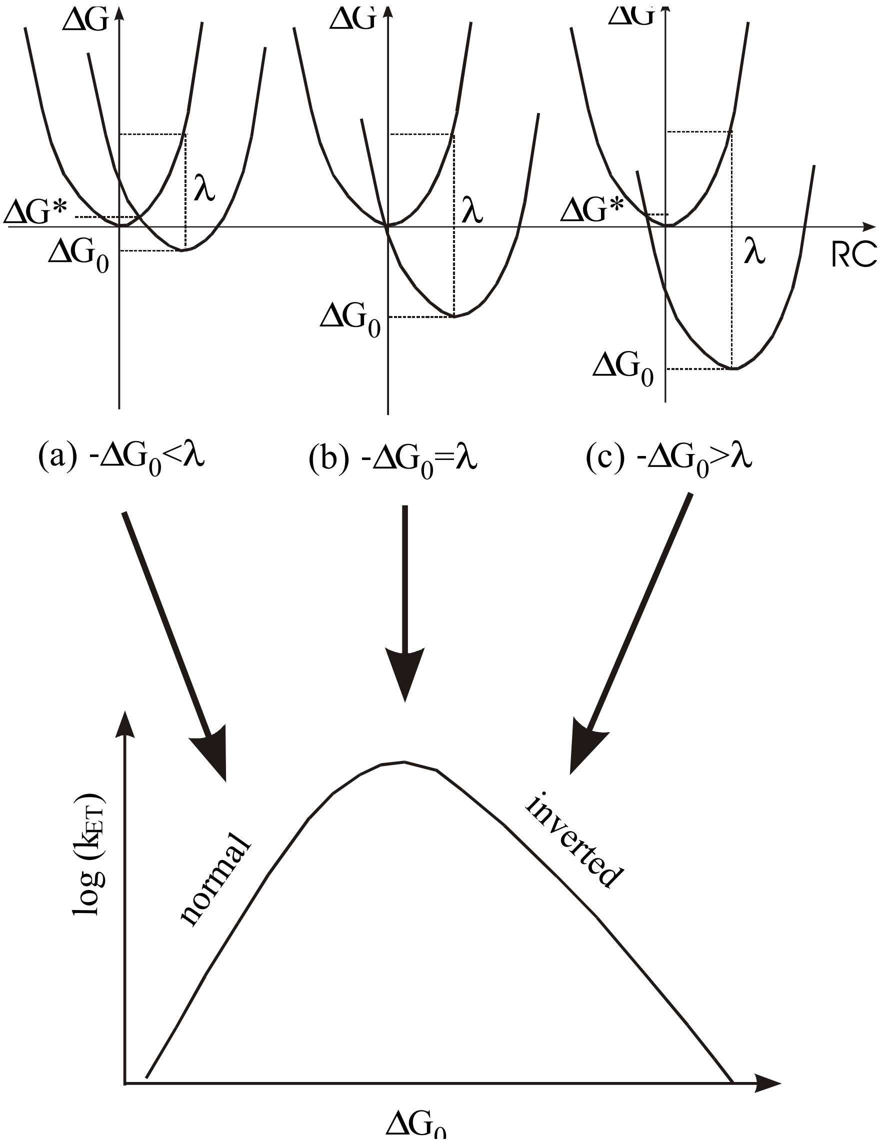

Fig. 2.3: Three free energy regimes after Marcus (top) and the corresponding dependence of the transfer rates on ΔG_0 (bottom). By increasing the free energy of reaction $-\Delta G_0$, the activation energy ΔG^* decreases leading to the increasing of the ET rate (normal regime). If $-\Delta G_0 > \lambda$, increasing further $-\Delta G_0$ leads to the increasing of ΔG^* and consequently to the decreasing of the ET rate (inverted regime). R and P represent the reactant and product, respectively. RC is the reaction coordinate.

2.3.3. Inner-sphere versus outer-sphere ET

Polar solvents could influence the ET reactions. The change of the charge distribution taking place during the ET process is very sensitive to the permanent dipole moment carried by polar solvent molecules. If the ET is not too fast, the solvent molecules react by formation of a polarization cloud around the transfer complex, which follow the ET reaction and influences the ET rate. To characterize this influence, the macroscopic dielectric properties of the solvent comprised in the dielectric function $\varepsilon(\omega)$ are used:

$$\varepsilon(\omega) = \varepsilon_\infty + \frac{\varepsilon_0 - \varepsilon_\infty}{1 + i\omega\tau_D} \qquad (2.21)$$

where $\varepsilon_\infty = n^2$ (n-refractive index of the medium) is the optical and ε_0 the static dielectric constant, ω is the light frequency and τ_D is the Debye dielectric relaxation time which is obtained by dielectric measurements.

If the ET is influenced mainly by solvent molecules, it is of outer-sphere type. The nuclear coordinates (and solvent degrees of freedom) which are coupled to the ET (i.e. are part of the reaction coordinate) are strongly perturbed by the solvent and the motion along the reaction coordinate becomes irregular, diffusion-like [21]. Consequently, the ET rate will be mainly determined by the inverse of the longitudinal dielectric relaxation time $\tau_L = \frac{\varepsilon_\infty}{\varepsilon_0}\tau_D$. On the other hand, the ET is of inner-sphere type whenever intramolecular nuclear motions are dominant. In this case the motion along the reaction coordinate is only weakly perturbed by the solvent, and thus it is called uniform motion [21].

The main questions related to the *outer-sphere ET* can be summarized as follows:

(i) the competition between ET and solvent dielectric relaxation. If the solvent dielectric relaxation is very fast (typically less than 1 ps), the ET time is comparable to the solvent dielectric relaxation time. This is the solvent controlled regime. For slow dielectric relaxation (tens of picoseconds), the role of intramolecular nuclear motions increase and thus the ET time is less than the solvent dielectric relaxation time.

(ii) the interrelationship between the ET dynamics and the dissipative properties of the polar medium;

The main questions related in particular to the *inner-sphere ET* are:

(i) to discern between active and spectator modes in the ET

(ii) the interplay between vibrational excitation during ET and the consecutive vibrational relaxation.

The distinction between inner-sphere and outer-sphere ET is reflected in the reorganization energy λ:

$$\lambda = \lambda_{in} + \lambda_{out} \qquad (2.22)$$

The solvent independent „inner“ term λ_{in} arises from structural differences between the equilibrium configurations of the reactant and product states. In the harmonic approximation, it can be written as:

$$\lambda_{in} = \frac{1}{2}\sum_i \bar{k}_i (r_i^{eq(R)} - r_i^{eq(P)})^2 \qquad (2.23)$$

where $\bar{k}_i$ is the reduced force constant for the i-th vibration, $r_i^{eq(R,P)}$ are the equilibrium bond lengths in the reactant and product states, respectively, and the sum is taken over all active intramolecular vibrations which are part to the reaction coordinate.

The solvent dependent „outer“ term λ_{out} is called solvent reorganization energy and arises from differences between the orientation and polarization of solvent molecules around $D^+A^-$and DA. It represents the energy necessary to reorient the solvent molecules around the new equilibrium geometry of the product, but neglecting the additional effects due to ET. By treating the solvent as a dielectric continuum, the following expression can be derived for λ_{out} [22]:

$$\lambda_{out} \cong B\left(\frac{1}{\varepsilon_{\infty}} - \frac{1}{\varepsilon_{s}}\right) \qquad (2.24)$$

where B is a solvent-independent parameter depending on the model chosen and the molecular dimensions. λ_{out} ranges from near zero for nonpolar solvents to 1.0 eV for polar solvents. It is also slightly temperature dependent, since both ε_{∞} and ε_{s} vary with temperature. But for most liquids, λ_{out} does not vary by more than 5% over a 100 K temperature range [22].

2.3.4. Adiabatic versus nonadiabatic ET

Two types of ET regimes can be distinguished according to the magnitude of the electronic coupling energy V_{el} between the reactant and product states, defined by:

$$V_{el} = \left\langle \Psi_0^R \middle| \hat{H}_{el} \middle| \Psi_0^P \right\rangle \qquad (2.25)$$

where the Ψ_o^R and Ψ_0^P are the diabatic electronic wave functions of the equilibrium reactant and product states, respectively, and $\hat{H}_{el}$ is the electronic hamiltonian of the system calculated for rigid nuclei (Born-Oppenheimer approximation). For large V_{el} splitting, the ET reaction follows always the lower surface, κ_{el} in Eq. (2.19) is equal to unity and the reaction is called adiabatic (Fig. 2.4 left). For very small V_{el}, the reactant and product surfaces do not interact significantly, the transition occurs only occasionally, κ_{el} in Eq. (2.19) is close to zero and the reaction is called non-adiabatic (Fig. 2.4 right).

The physical meaning of this separation can be seen by introducing the typical times for electronic motion $\tau_{el} = \hbar / |V_{el}|$ and vibrational motion $\tau_{vib} = 2\pi / \omega_{vib}$, where ω_{vib} is the vibrational frequency [21].

If $\tau_{el} << \tau_{vib}$ (V_{el} large) , the electron will move many times between the donor D and acceptor A before any change in the nuclear configuration occurs. Consequently, this is the adiabatic case in the sense of Born-Oppenheimer.

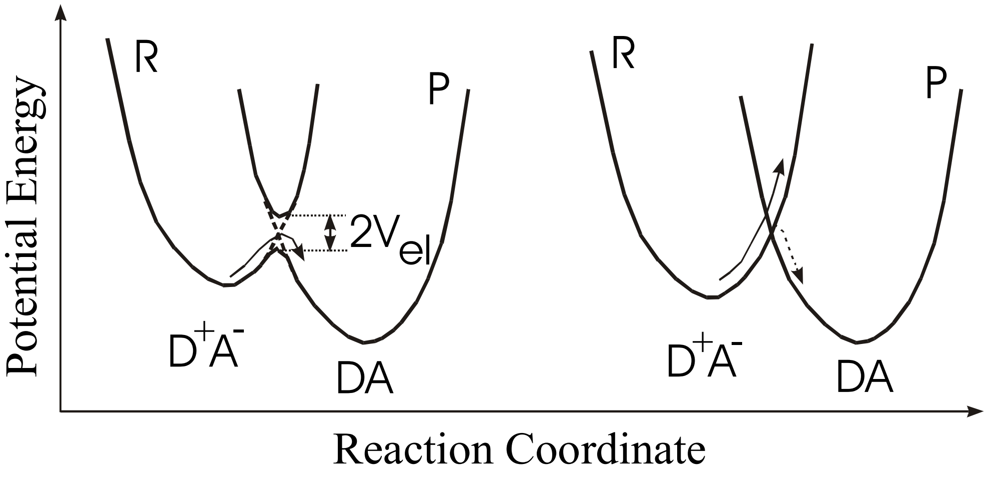

Fig. 2.4: Adiabatic (left) and nonadiabatic (right) ET V_{el} is the same as defined in Eq. (2.25). The paths for ET are shown. P and R are the product and reactant diabatic states, respectively.

If $\tau_{el} >> \tau_{vib}$ (V_{el} small), the vibrational motion is much faster than the electronic one and the reaction is non-adiabatic.

2.3.5. Microscopic ET rates using the Fermi's Golden Rule

The classical Marcus theory presented in Paragraph 2.2.2 fits well with the experiment in the case of adiabatic ET reactions. For non-adiabatic reactions, however, nuclear tunneling between the reactant and product surfaces has to be taken into account.
Nuclear tunneling means that the stationary vibrational wave-functions is not strictly localized in the potential energy surface of reactant, but tails of it reach into the areas of the potential energy surface of the product. Vibrational overlap between the two surfaces becomes of major importance. The overlap between different vibrational wavefunctions in the reactant and product states is shown schematically in Fig. 2.5. One can see that in the inverted regime nuclear tunneling plays a more important role than in the normal regime.

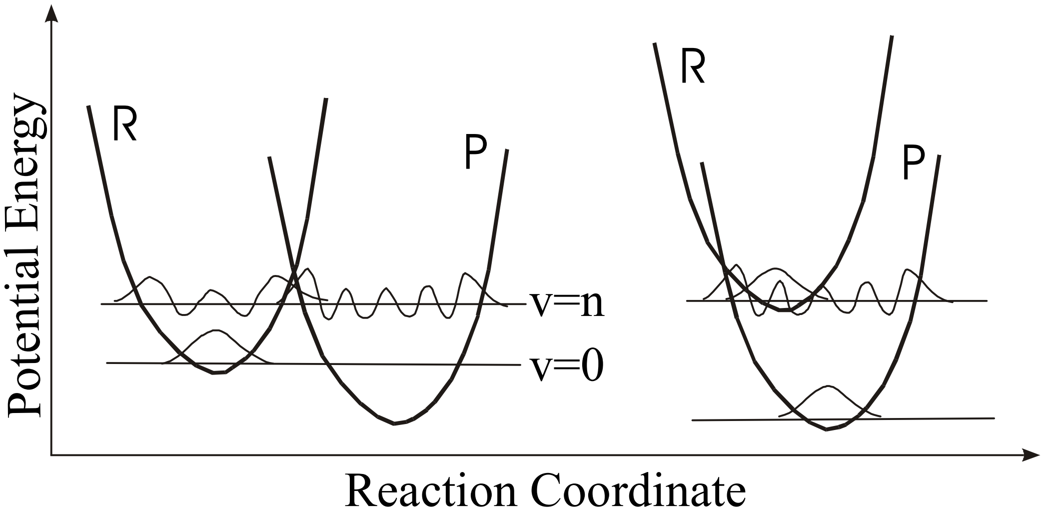

Fig. 2.5: Schematic view of the vibrational overlap between the reactant R and product P vibrational wavefunctions in the normal (left) and in the Marcus inverted regime (right). v represents the vibrational quantum number.

For the description of mode-selective ET, the concept of microscopic ET rate is introduced [18]. The transition rate constant k_i from an initial vibrational level i in the reactant state to a set of vibrational levels f in the product state is given in the time-dependent perturbation theory in the form of the Golden Rule expression:

$$k_i = \frac{2\pi}{\hbar} V_{el}^2 \sum_{fi} \left\langle \chi_{Pf}^0 \middle| \chi_{Ri}^0 \right\rangle^2 \delta(\varepsilon_{Pf} - \varepsilon_{Ri}) \qquad (2.26)$$

Here χ_{Pf}^0 and χ_{Ri}^0 are the vibrational wave functions for the equilibrium product f and reactant i states, δ is the Dirac delta function ensuring the energy conservation, ε_{Ri} and ε_{Pf} are the vibrational energies of the i-th vibrational levels in the reactant and f-th vibrational level in the product states, respectively. V_{el} is the same as defined in Eq. (2.25) and the sum is taken over all internal and solvent vibrational modes in the product state. $\left\langle \chi_{Pf}{}^{0} \middle| \chi_{Ri}{}^{0} \right\rangle^{2}$ are the Franck-Condon factors for levels i and f, representing the overlap between the two vibrational wavefunctions.

In some treatments [23] the solvent vibrations and the low frequency internal modes are considered classically, and thus the semiclassical Marcus equation can be written:

$$k_{ET} = \frac{2\pi}{\hbar} V_{el}{}^{2} (4\pi\lambda_{out} k_B T)^{-1/2} \sum_{f} \left\langle \chi_{Pf}^{0} \middle| \chi_{Ri}^{0} \right\rangle^{2} \exp\left[- \frac{\left(\Delta G_0 + \varepsilon_{Pf} - \varepsilon_{Ri} + \lambda_{out}\right)}{4\lambda_{out} K_B T} \right] \qquad (2.27)$$

If the relevant high-frequency vibrations in the reactant state are replaced by one averaged mode with the frequency υ, Eq. (2.27) transforms into [24]:

$$k_{ET} = \frac{2\pi}{\hbar} V_{el}{}^{2} (4\pi\lambda_{out} k_B T)^{-1/2} \sum_{n=0}^{\infty} \left[\frac{e^{-S} S^{n}}{n!} \right] \exp\left[- \frac{\left(\Delta G_0 + \lambda_{out} + nh\upsilon\right)}{4\lambda_{out} K_B T} \right] \qquad (2.28)$$

where n is an integer and $S = \lambda_{in} / h\upsilon$

For a complete description of mode-selective ET, the mode-specific Franck-Condon factors should be expressed. In the simples approximation, the solvent contribution can be introduced in the form of line-shape function.

References

[1] E. Teller, An historical note, in „The Jahn-Teller Effect in Molecules and Crystals“ (R. Englman, ed.), Wiley-Interscience, London (1972)

[2] H. A. Jahn and E. Teller, Proc. R. Soc. London, Ser. A **161 (**1937) 220

[3] I. B. Bersuker, in „The Jahn-Teller effect and vibronic interactions in modern chemistry“, Ed. John P. Fackler, Plenum Press, New York and London (1984)

[4] R. S. Mulliken, J. Chem.Phys. **23** (1955) 1997

[5] H. A. Jahn, Proc. R. Soc. London, Ser. A, **164** (1938) 117

[6] R. Renner, Z. Phys. **92** (1934) 172

[7] E. J. Heller, Acc. Chem. Res. **14** (1981) 368

[8] W. F. Libby, Abstract 117, 115th National Meeting of the American Chemical Society, San Francisco, CA, March (1949)

[9] R.A. Marcus, J. Chem. Phys. **24** (1956) 966

[10] R.A. Marcus, J. Chem. Phys. **24** (1956) 979

[11] R.A. Marcus, J. Chem. Phys. **26** (1957) 867

[12] R.A. Marcus, J. Chem. Phys. **26** (1957) 872

[13] R.A. Marcus, Discuss. Faraday Soc. **29** (1960) 21

[14] V. G. Levich, Adv. Electrochem. Electrochem. Eng. **4** (1966) 249

[15] R. R. Dogonadze, E. M. Kuznetsov, and V. G. Levich, Electrochim. Acta **13** (1968) 1025

[16] J. Jortner, M. Bixon; J. Chem. Phys. **88** (1988) 167

[17] M. Bixon, J. Jortner; J. Chem. Phys. **176** (1993) 467

[18] Electron Transfer From Isolated Molecules To Biomolecules, Parts 1 and 2. AdVances in Chemical Physics; M. Bixon, J. Jortner, Eds.; Wiley: New York, Vol. **106** and **107** (1999)

[19] L. D. Landau, Phys. Z. Sow. **2** (1932) 46

[20] C. Zener, Proc. Roy. Soc., (London) A **137** (1932) 696

[21] V. May, O. Kühn, in „Charge and Energy Transfer Dynamics in Molecular Systems“, Wiley-VCH Verlag, Berlin (2000) Chapter 6

[22] J. R. Bolton, and M. D. Archer, in „Electron transfer in inorganic, organic, and biological systems“, J. R. Bolton, N. Mataga, and G. McLendon Eds., Adv. in Chem. Series, Hardcover, **228,** (1991), 14.

[23] R. A. Marcus, N. Sutin, Biochem. Biophys. Acta **811 (**1985) 265

[24] J. Jortner, J. Chem. Phys. **64** (1976) 4860

3. Experiment

3.1. Theoretical considerations of the experiments

3.1.1. Introduction

The response of a medium to incident electromagnetic radiation is formulated in terms of induced macroscopic polarization. In the electric dipole approximation, the induced polarization may be written as a Taylor expansion on the strength of the applied electric field $E(r,t)$ [1]:

$$P(E) = \chi^{(1)}E + \chi^{(2)}:EE + \chi^{(3)}:EEE + ... \qquad (3.1)$$

$\chi^{(1)}$ is here the linear susceptibility, and the quantities $\chi^{(2)}$ and $\chi^{(3)}$ are the second- and third-order nonlinear susceptibilities, respectively. $\chi^{(1)}$ is a second-rank tensor describing optical linear processes like (linear) absorption or refraction, $\chi^{(2)}$ is a third-rank tensor describing three-wave interactions (like Second Harmonic Generation SHG, sum-and difference-frequency generation), and $\chi^{(3)}$ is a fourth-rank tensor describing the four-wave interactions (four-wave mixing) like for example third-harmonic generation or Coherent Anti-Stokes Raman Scattering (CARS).

At this point it should be mentioned that the susceptibilities from Eq. 3.1 are bulk quantities. They are related to the microscopic quantities α, β and γ named polarizability, the first and second hyperpolarizability, respectively.

Although higher order terms in the expansion (3.1) could play a role if working with very high incident intensities, for the purpose of this thesis their contribution can be neglected.

3.1.2. Raman scattering

3.1.2.1. Molecular polarizability

When an electric field with strength f is applied to a molecule, an induced dipole moment μ is created:

$$\mu = \alpha \cdot f \qquad (3.2)$$

Here, α is the molecular polarizability. In the general case, the vectors μ and f do not coincide, and equation (3.2) can be rewritten in the following form:

$$\begin{pmatrix} \mu_x \\ \mu_y \\ \mu_z \end{pmatrix} = \begin{pmatrix} \alpha_{xx} & \alpha_{xy} & \alpha_{xz} \\ \alpha_{yx} & \alpha_{yy} & \alpha_{yz} \\ \alpha_{zx} & \alpha_{zy} & \alpha_{zz} \end{pmatrix} \cdot \begin{pmatrix} f_x \\ f_y \\ f_z \end{pmatrix} \qquad (3.3)$$

where α_{ij} are the elements of the second rank polarizability tensor α, defined in a space-fixed coordinate system ($i,j=x,y,z$). α is a symmetrical tensor ($\alpha_{ij}=\alpha_{ji}$), and therefore has only six independent components. In this representation, the components of α depend on the space orientation of the molecule but not on the direction of the applied electric field.

For each symmetrical tensor, a special set of Cartesian coordinates *x'*, *y'*, and *z'* exists with respect to which the tensor can be diagonalized. α acquires then the following form:

$$(\alpha)=\begin{pmatrix} \alpha_{x'x'} & 0 & 0 \\ 0 & \alpha_{y'y'} & 0 \\ 0 & 0 & \alpha_{z'z'} \end{pmatrix} \qquad (3.4)$$

In this case, the induced dipole is parallel to the external field vector.

The tensor α is characterized with two invariants with respect to any reorientation of the molecule in space. These are the mean polarizability $\overline{\alpha}$ and the anisotropy γ:

$$\overline{\alpha}=(\alpha_{xx}+\alpha_{yy}+\alpha_{zz})/3 \qquad (3.5a)$$

$$\gamma^2=\left[(\alpha_{xx}-\alpha_{yy})^2+(\alpha_{yy}-\alpha_{zz})^2+(\alpha_{zz}-\alpha_{xx})^2+6(\alpha_{xy}{}^2+\alpha_{xz}{}^2+\alpha_{yz}{}^2)\right]/2 \qquad (3.5b)$$

It can be easily seen that γ vanishes for molecules possessing spherical polarizability.

If linearly polarized light is used to illuminate the sample, the scattered light may be depolarized to some extend, and contain radiation polarized either parallel (with intensity I) or perpendicular (with intensity $I_\perp$) with respect to the polarization of the incident beam.

In every scattering experiment, for rectangular geometries and by using polarized light, the depolarization ratio $\rho = I/\ I_\perp$ is defined, which can be correlated with the two invariants like in the following:

$$\rho=\frac{3\gamma^2}{45\overline{\alpha}^2+4\gamma^2} \qquad (3.6)$$

It should be emphasized that alternative sets of coefficients for γ and $\overline{\alpha}$ should be used for experiments with unpolarized (natural) light and different experimental geometries. Because $\overline{\alpha}$ vanishes for distortions belonging to non-fully symmetric species, the depolarization ratio becomes 3/4. On the other hand, ρ reaches its minimum for totally symmetric vibrations. Thus, the depolarization ratio offer the possibility for examining the symmetry of vibrational transitions.

3.1.2.2. Raman intensity and selection rules

The intensity of Raman lines is given by the changes in molecular polarizability during vibrational transitions. The α_{jk} polarizability matrix element for a transition from a vibronic initial state *i* to a vibronic final state f is given in quantum mechanics by:

$$(\alpha_{jk})_{if}=\rangle\Psi_f|\alpha_{jk}|\Psi_i\langle=\int_{-\infty}^{\infty}\Psi_f^*\alpha_{jk}\Psi_i d\tau \qquad (3.7)$$

where $\Psi_{i,f}$ are the vibronic wave functions of the initial and final states.

For small molecular vibrations, the polarizability of the molecule can be expanded in a Taylor series along the normal coordinates Q_i:

$$\alpha=\alpha_0+\sum_r\left(\frac{\partial\alpha}{\partial Q_r}\right)_0 Q_r+\frac{1}{2!}\sum_{r,s}\left(\frac{\partial^2\alpha}{\partial Q_r\partial Q_s}\right)_0 Q_rQ_s+\frac{1}{3!}\sum_{r,s,t}\left(\frac{\partial^3\alpha}{\partial Q_r\partial Q_s\partial Q_t}\right)_0 Q_rQ_sQ_t+.. \qquad (3.8)$$

α_0 is here the polarizability tensor in an equilibrium non-perturbed state. All the derivatives are taken at the equilibrium geometry of the molecule.

By combining Eq. (3.7) and (3.8) and neglecting the contribution from higher order terms, the following integral is obtained:

$$(\alpha_{jk})_{if} = (\alpha_{jk})_0 \int_{-\infty}^{\infty} \Psi_f^{\,*} \Psi_i d\tau + \left(\frac{\partial \alpha_{jk}}{\partial Q_i} \right)_0 \int_{-\infty}^{\infty} \Psi_f^{\,*} Q_i \Psi_i d\tau + ... \qquad (3.9)$$

The first term in Eq. (3.9) is responsible for Rayleigh scattering, and the second term gives rise to Raman scattering, if two conditions are fulfilled (under non-resonant conditions):

(i) the polarizability derivative $\left(\frac{\partial \alpha_{jk}}{\partial Q_i} \right)_0 \neq 0$, i.e., the polarizability of the molecule must change during a particular vibrational transition, and

(ii) the integral $\int_{-\infty}^{\infty} \Psi_f^{\,*} Q_i \Psi_i d\tau \neq 0$. The latter condition requires that the vibrational quantum number of the transition differs only by 1 for Stokes Raman scattering and -1 for anti-Stokes Raman scattering.

The intensity of the *i*-th Stokes Raman line is given by [2]:

$$I_i = I_0 N_{\omega_i} \frac{2^7 \pi^5}{3^2 c^4} \frac{\hbar}{\omega_i} (\omega_0 - \omega_i)^4 \frac{1}{1 - e^{-\hbar \omega_i / kT}} \sum_{j,k} (\alpha_{jk})_i^2 \qquad (3.10)$$

where I_0 and ω_0 are the intensity and frequency of the incident laser, respectively, N_{ω_i} is the number of molecules in the vibrational state i with the frequency ω_i, c is the speed of light, and $\hbar = h / 2\pi$ the Planck constant. The term $\frac{1}{1 - e^{-\hbar \omega_i / kT}}$ is the vibrational partition function and it is due to the contribution of „hot bands“, i.e. to transitions of the type $1 \rightarrow 2$, $2 \rightarrow 3$ etc. to the Stokes Raman intensity and of the type $2 \rightarrow 1$, $3 \rightarrow 2$ etc. for the anti-Stokes Raman intensity. Eq. 3.10 can be written in a simplified manner as:

$$I_i = I_0 N_{\omega_i} \sigma_i \qquad (3.11)$$

where σ_i is the Raman cross-section defined as:

$$\sigma_i = \frac{2^7 \pi^5}{3^2 c^4} \frac{\hbar}{\omega_i} (\omega_0 - \omega_i)^4 \frac{1}{1 - e^{-\hbar \omega_i / kT}} \sum_{j,k} (\alpha_{jk})_i^2 \qquad (3.12)$$

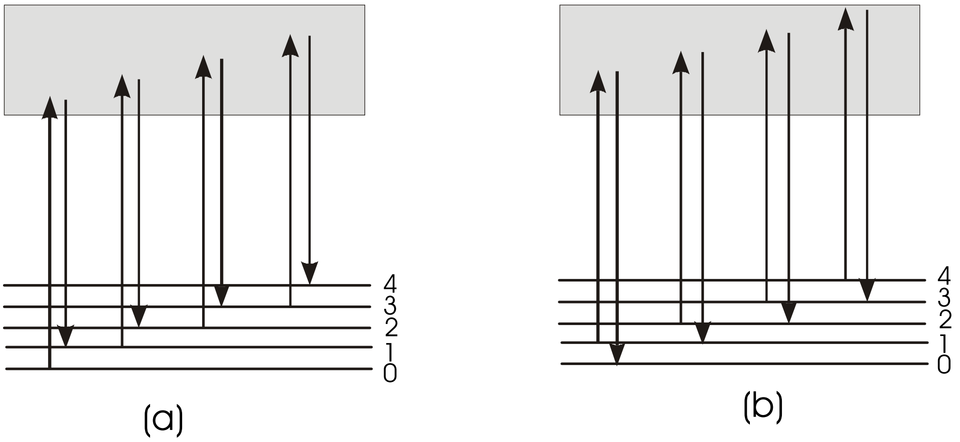

Fig. 3.1: Schema for Stokes (a) and anti-Stokes (b) Raman scattering. The vibrational levels are labeled with 0, 1, 2, ...

Anti-Stokes Raman scattering occurs only from excited vibrational levels, as shown in Fig. 3.1., and gives a direct indication of the population of the respective excited vibrational levels. Therefore, it is a very useful method in probing „hot“ molecules.

3.1.2.3. The Resonance Raman effect

If the excitation light frequency approaches to (pre-resonance condition) or equals (resonance condition) the frequency of an electronic transition of the molecule, the dependence of the molecular polarizability on the incident light frequency has to be considered. The molecular polarizability is than given by [2]:

$$(\alpha_{jk})_{if} = \sum_{v \neq i} \left(\frac{\langle v|M_k|i\rangle\langle f|M_j|v\rangle}{E_v - E_i - E_0 + i\Gamma} \right) \tag{3.13}$$

with E_v being the energy of the v-th vibrational state in the excited state, E_i the energy of the i-th vibrational state in the ground state, E_0 the energy of the incident light, Γ a phenomenological damping factor, M_k and M_j the respective transition dipole moment operators. From Eq. (3.13) it can be seen that if $E_0 = E_v - E_i$, some components of the molecular polarizability are strongly enhanced, and thus, some Raman lines increase in intensity hundreds or even thousands of times.

3.1.3. Coherent Anti-Stokes Raman Scattering (CARS)

3.1.3.1. General CARS

Investigation of vibrational spectra of molecules in condensed matter by using spontaneous Raman scattering is often very difficult due to the high fluorescence background coming from the solute or solvent. Measuring transient species is even more complicated because of (i) the overlap of the ground state Raman spectra with spectra originating from the transients, and (ii) radiative emission which is, in most cases, very high compared with the Raman intensity. Subtraction of the contributions from the ground state and background, respectively, should be made in this case.

Another possibility is to use nonlinear coherent techniques like CARS and Coherent Stokes Raman Scattering (CSRS), which are, in special cases, very useful. Specifically, the advantage comes from (i) the nonlinear dependence of the generated signal on the laser power which implies that short pulses with high power are more efficient, and (ii) the possibility of fluorescence suppression owing from the coherent nature of the emitted signal.

In the classical picture, the spontaneous Raman scattering is seen as a modulation of the oscillating dipole moment $p = \alpha E$ (α is the molecular polarizability and E is the monochromatic radiation field) by a molecular vibration ω, exhibiting Stokes ($\omega_S = \omega_{laser} - \omega$) and anti-Stokes ($\omega_{AS} = \omega_{laser} + \omega$) frequencies. Because the modulation is brought by the random-phased vibration of molecules, this emission is not coherent .

On the other hand, coherent Raman scattering comes from the forced molecular vibration generated by two different laser radiations E_1 and E_2 with the frequencies ω_1 and ω_2, respectively. The vibrational motion is generated in every molecule with a phase defined by the phase matching condition (Fig. 3.2). Consequently, Raman scattering due to this vibration forms a coherent radiation which propagates along the oscillating molecules. In this way, besides the incident frequencies ω_1 and ω_2, other frequencies $\omega_3=2\omega_1-\omega_2$ (for CARS) and $\omega_4=2\omega_2-\omega_1$ (for CSRS) are generated (see Fig. 3.2 and 3.3).

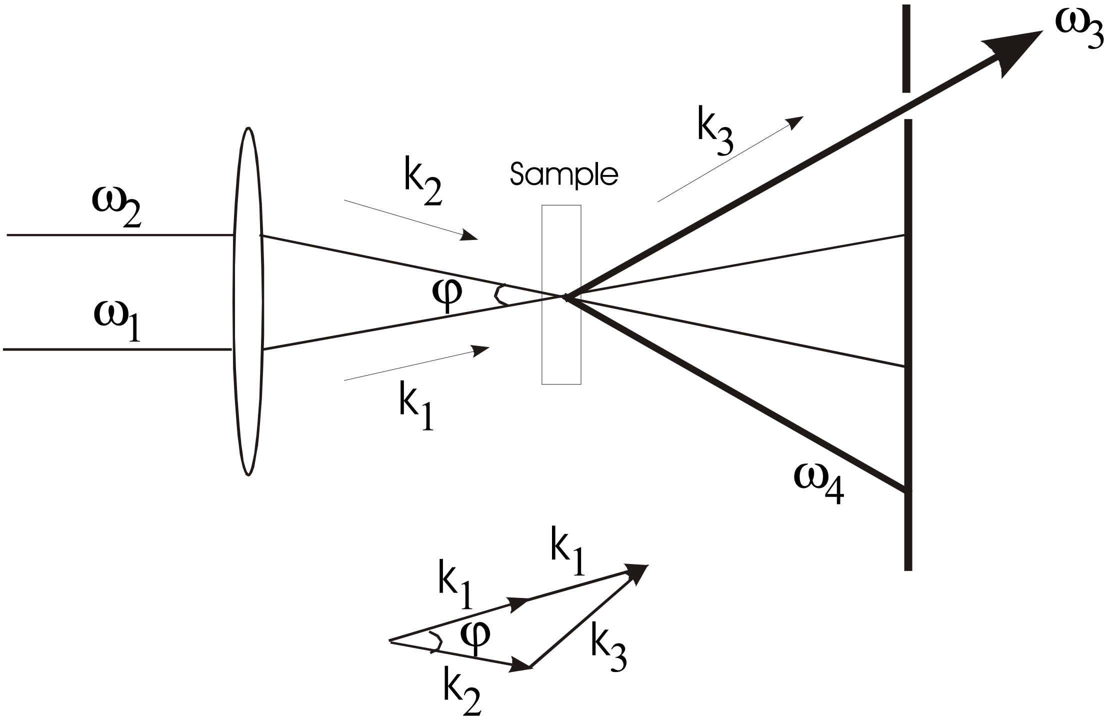

Fig. 3.2: Experimental schema of CARS and CSRS alignment (top) and the phase matching condition (bottom) for the wave vectors k_i

If one of the incident electric fields $E_1(\omega_1)$ has a fixed frequency ω_1, and the second field $E_2(\omega_2)$ is spectrally very broad and centered around ω_2, the generated CARS signal $E_3(-\omega_3,\omega_1,\omega_1,-\omega_2)$ contains more information than the spontaneous Raman spectrum. In addition to Raman frequencies and intensities, the third-order electronic hyperpolarizabilities γ can be derived.

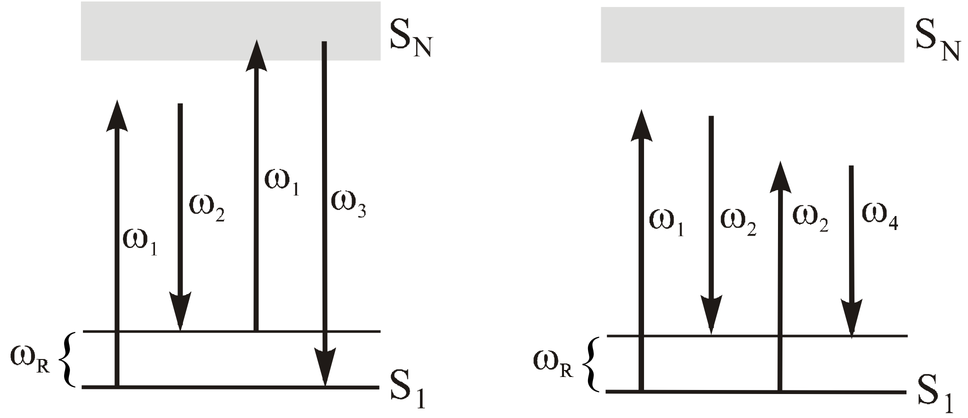

Fig. 3.3: Schema of the CARS (left) and CSRS (right) generation

Because the CARS spectrum occurs on a background coming from the electronic contribution of the solute and solvent (which reproduces the spectral distribution of the broad band dye laser), it is necessary to divide the spectral distribution of the CARS spectrum through the spectral distribution of the glass plate. Thus, the normalized CARS spectrum $E_3^N(-\omega_3,\omega_1,\omega_1,-\omega_2)$ is obtained. In a neat medium, it results from the modulus squared of the overall (molecular) third order hyperpolarizability γ^{FWM} [3] during the Four-Wave-Mixing (FWM) process:

$$E_3^N(-\omega_3,\omega_1,\omega_1,-\omega_2) \propto \left|\gamma^{FWM}(-\omega_3,\omega_1,\omega_1,-\omega_2\right|^2 = \left|\gamma^{NR} + \sum_R \frac{\gamma^R}{\delta_R + i\Gamma_R}\right|^2 \qquad (3.14)$$

CARS is measured at the signal-frequency $\omega_3 = 2\omega_1 - \omega_2$ around $\delta_R = \omega_R - \omega_1 + \omega_2$. *R* and *NR* means here Raman resonance and non-resonance, respectively, $\left|\gamma^R\right|/\Gamma_R$ is the Raman amplitude of the mode with the vibrational frequency ω_R and line width Γ_R. The susceptibilities γ^{NR} and γ^R are constants or - in the case of electronic resonance - they vary very slowly within the range of a Raman spectrum (depending on the detuning of the excitation frequencies from the comparatively broad electronic transitions [4]). In non-absorbing materials, such as most solvents used, laser frequencies are far from electronic resonance. In this case γ^{NR} and γ^R are real valued quantities. Near electronic resonance they become complex values [5, 6].

The total coherent Raman four-wave mixing spectrum at $\omega_3 = 2\omega_1 - \omega_2$ for a solute (which may be also a short living transient) in a solution is given by:

$$E_3^N(-\omega_3,\omega_1,\omega_1,-\omega_2) \propto \left|(1-c)\gamma_{solvent}^{FWM} + c\gamma_{solute}^{FWM}\right|^2 \qquad (3.15)$$

Here $c = N_{solute}/(N_{solute} + N_{solvent})$ is the relative concentration of the solute, (*N* is the number of molecules per cm^3). It is obvious from the expression (3.14) and (3.15) that the CARS spectrum contains interference terms between different contributions. As a consequence an isolated vibrational resonance is characterized by a constant (electronic) background (amplitude *A*), by a positive or negative dispersion-like shaped (*B*) and by a Lorentzian shaped (*C*) contribution:

$$E_3(\delta_R) \propto A + \frac{\delta_R B + C}{\delta_R^2 + \Gamma_R^2} \qquad (3.16)$$

C is always positive in the nonresonant case, and can be positive or negative under electronic resonance. Depending on the sign of the parameter C, dips or peaks in the CARS spectrum can be observed. Dips (i. e. $C < 0$) are generated with complex parameters only, indicating electronic resonance.

Due to interference with the electronic background the vibrational frequencies coincide neither with the spectral position of the peaks nor with that of the dips in the CARS spectra (see Eq. 3.16). Thus, a fitting procedure as outlined in Chapter 4 is applied to get Raman frequencies, intensities and phases as well as the electronic contribution to the hyperpolarizability [5, 6].

3.1.3.2. Polarization CARS

The nonlinear polarization responsible for CARS is:

$$P(\omega_3) = \chi^{(3)}(\omega_3)E_1^{\,2}(\omega_1)E_2(\omega_2)e^{-i\omega_3 t} + c.c. \qquad (3.17)$$

where $\chi^{(3)}(\omega_3)$ is the third order nonlinear susceptibility, which is a fourth rank tensor, most generally consisting of 81 components defined by:

$$P_i(\omega_3) = \chi^{(3)}_{ijkl} E_{1,j} E_{1,k} E^{*}_{2,l} e^{-i\omega_3 t} + c.c.$$

where *i, j, k, l*=1, 2, 3 represent Cartesian coordinates.
In the case of isotropic media (like for example in liquids and gases) there are only 21 nonzero components. Among them, for symmetry reasons, only two can be independent. They are designated as χ_{1111} and χ_{1221}, corresponding to the polarization schemes:
$P(\omega_1) \,||\, P(\omega_2) \,||\, P(\omega_3)$ and
$P(\omega_1) \perp P(\omega_2) \,||\, P(\omega_3)$, respectively. $P(\omega_i)$ represents here the linear polarization vector of ω_i radiation.

The polarization character of the CARS resonances, i.e., the CARS depolarization ratio can be expressed as [7]:

$$\rho^R = \frac{\chi_{1221}}{\chi_{1111}} = \frac{-5\gamma_a^{\,2} + 3\gamma_s^{\,2}}{45\bar{\alpha}^2 + 4\gamma_s^{\,2}} \qquad (3.18)$$

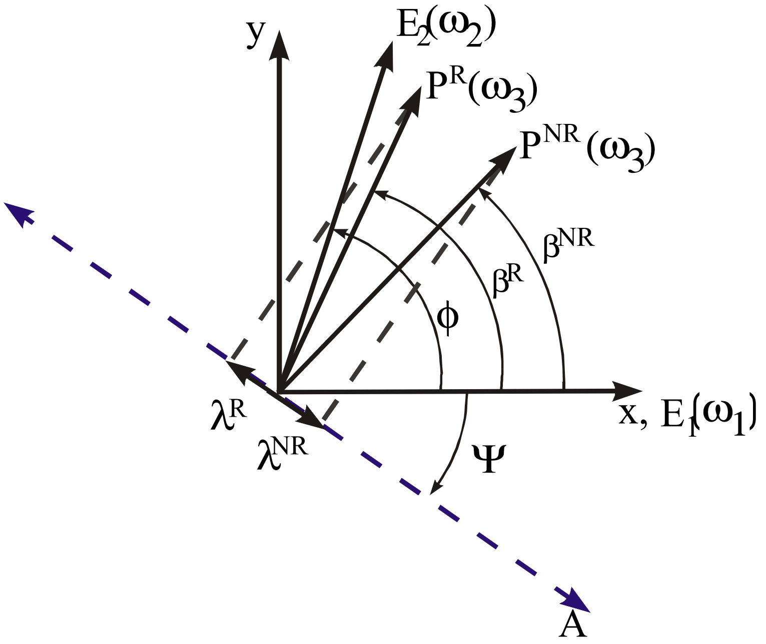

Fig. 3.4: Scheme of polarization CARS. $E_1(\omega_1)$ and $E_2(\omega_2)$ are the planes of polarization of the laser radiations at ω_1 and ω_2. $P^R(\omega_3)$ and $P^{NR}(\omega_3)$ are the planes of Raman resonant and Raman non-resonant contributions. λ^R and λ^{NR} are the projections of the polarizations of $P^R(\omega_3)$ and $P^{NR}(\omega_3)$ on the transmission plane Ψ of the polarizer.

with $\bar{\alpha}$ the mean polarizability as defined in Eq. 3.5a, γ_a and γ_s the antisymmetric and symmetric anisotropy (*R* in the superscript indicates Raman resonance). ρ^R is the analogue of the depolarization ratio known from spontaneous Raman scattering and allows to distinguish qualitatively the symmetry of vibrational modes. This is possible because, in general, the vibrational polarization vectors $P^R(\omega_3)$ and the polarization vector P^{NR} (*NR* indicate non resonance) of the electronic contribution of the third order susceptibility are all different.

ρ^R can be obtained by measuring γ^R with parallel and perpendicular polarization of the two laser beams at ω_1 and ω_2, respectively. However, a more convenient method often used to determine its value is by using a polarization CARS scheme, as shown in Fig.3.4.
The polarization vectors of the laser radiation with the frequencies ω_1 and ω_2 were chosen to form an angle of $\phi=71.5^0$ with each other. In this case, for $\rho^{NR}=1/3$ (from Kleinmann symmetry) β^{NR} becomes 45^0 (β^{NR} is the angle of polarization P^{NR} of the non resonant electronic background - see Fig. 3.4). By tuning the angle Ψ of the analyzer A to a position perpendicular to the plane of polarization $P^R(\omega_3)$ of the Raman resonances, where the Raman resonances disappear in the CARS spectrum (i.e., for $\Psi=90^o-\beta^R$, where $\lambda_R=0$), the depolarization ratios ρ^R of the vibrations R can be obtained using the expression $\rho^R=\frac{\chi^R_{1221}}{\chi^R_{1111}}=\frac{\tan\beta^R}{\tan\phi}$ [7, 8].
Another advantage of the polarization CARS scheme is that „background-free“ spectra can be obtained, i.e., spectra free of the electronic background. Tuning the angle of the analyzer A perpendicular to the polarization plane of the nonresonant background P^{NR} (i.e., for $\Psi=90^o-\beta^{NR}$, where $\lambda^{NR}=0$), the pure vibrational contributions can be seen, however, on a much lower signal level [7].

3.1.4. Second Harmonic Generation (SHG)

SHG has become, after the invention of pulsed laser systems, an important method used for the extension of the wavelength range in a lot of applications. Schematically, this nonlinear process is illustrated in Fig. 3.5.

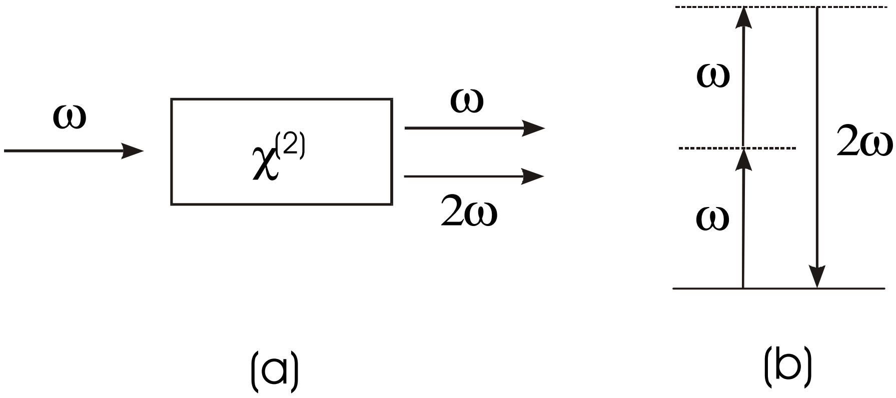

Fig. 3.5: Scheme of SHG generation in a nonlinear crystal

The nonlinear polarization responsible for SHG generation is:

$$P(2\omega)=\sum_{j,k}\chi_{ijk}E_j(\omega)E_k(\omega) \qquad (3.17)$$

where i, j, k=1, 2, 3 represent Cartesian coordinates. Symmetry considerations of the susceptibility tensor χ_{ijk} show that systems with macroscopic inversion symmetry posses only vanishing second-order coefficients $\chi_{ijk}=0$. Consequently, SHG, like other three order processes, is restricted to [9]:
(i) single crystals of certain crystal classes,

(ii) surfaces, and
(iii) systems where the inversion symmetry is broken by an electrostatic field or a density gradient.

The intensity of the new generated radiation can be evaluated for incident collimated plane monochromatic waves with the following equation [9]:

$$I_{SHG} = C \cdot \chi_{eff}{}^2 \cdot l^2 \cdot I_L{}^2 \cdot \left(\frac{\sin(\Delta k \cdot l/2)^2}{\Delta k \cdot l/2} \right)^2 \qquad (3.18)$$

Here C is a constant, l is the crystal or interaction length, I_L the intensity of the incident monochromatic wave, $\Delta k = k_{SHG} - 2k_L$ the mismatch between the SHG and fundamental wave vectors. For optimum SHG, perfect phase matching $\Delta k = 0$ is required, allowing large interaction lengths. A more realistic condition is $\Delta k \cdot l \leq 2.78$ [9]. Phase velocity dispersion effects ($k(\omega) = \frac{n(\omega) \cdot \omega}{c}$ with n-the refractive index, ω the frequency of the electromagnetic wave and c-the speed of light) makes efficient phase matching difficult. Using birefringent crystals, with polarization and orientation dependent refractive index, a long interaction length can be achieved, and high conversion efficiencies can be obtained. Assuming perfect phase matching, the following equation for the SHG conversion efficiency is obtained:

$$\eta = \frac{I_{SHG}}{I_L} = \tanh^2(\sqrt{C \cdot \chi_{eff}{}^2 \cdot I_L \cdot l^2}) \qquad (3.19)$$

The dependence of η on $\tanh^2$ function results in a slower increase of the conversion efficiency for conversion factors larger than 0.1.

For short pulses, the interaction length in nonlinear crystals is also limited by group velocity dispersion. The group delay (difference of the transit times) is [10]:

$$t_g = \frac{l}{c} \left[\lambda_L \left(\frac{dn}{d\lambda} \right)_L - \lambda_{SHG} \left(\frac{dn}{d\lambda} \right)_{SHG} \right] \qquad (3.20)$$

with c the speed of light. In the case of picosecond pulses, $t_g << t_p$ (t_p is the pulse duration) and these effects do not play any role in the conversion efficiency. In this limit, the new radiation obtained in the nonlinear process will have a slightly shortened duration by a factor of $\sqrt{2}$ compared with the duration of the incident pulse of Gaussian shape.

3.1.5. Stimulated Raman Scattering (SRS)

Another method used to extend the wavelength range for spectroscopy is stimulated Raman scattering. This effect, governed by the $\chi^{(3)}$ susceptibility, occurs at high

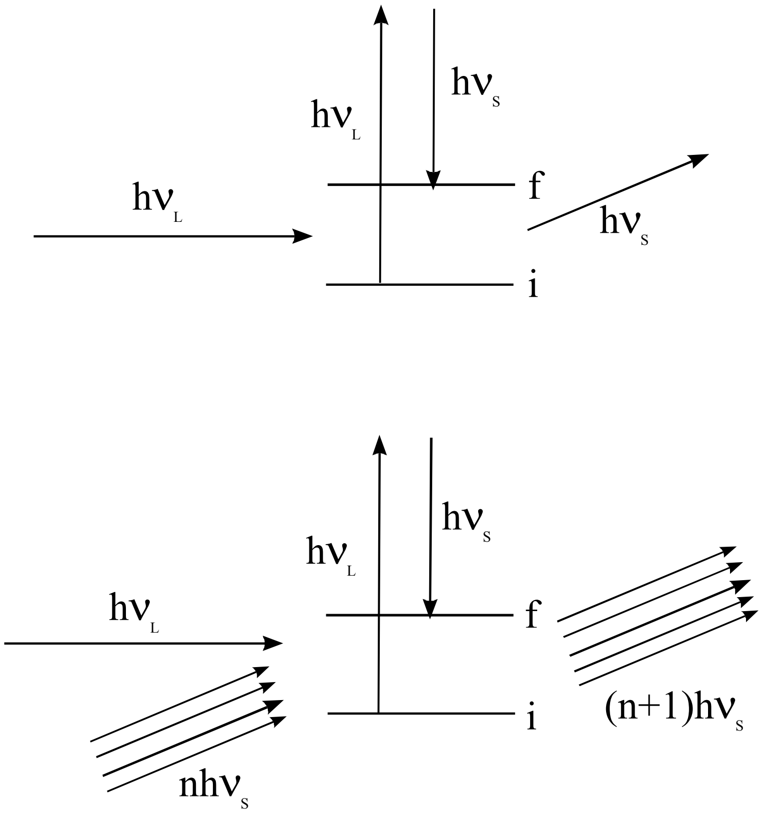

Fig.3.6: Schematic representation of the spontaneous (top) and stimulated (bottom) Raman scattering as a quantum process from the initial state i to the final state f.

incident intensities. It is a partially degenerate four-wave mixing process, where the two non-degenerate components are the laser frequency and a Stokes (or anti-Stokes) Raman line. A theoretical treatement of the SRS has been given by Bloembergen in 1967 [11]. A schematic diagram of the process is presented in Fig. 3.6.

According to [11], a light wave at frequency ω_S (the Stokes Raman wave) is incident on the material system simultaneously with a light wave at ω_L (the incident laser wave). A quantum $\hbar\omega_S$ is added to the wave ω_S, which thus becomes amplified, while the incident light beam looses a quantum $\hbar\omega_L$ and the material system is excited by a quantum $\hbar(\omega_L - \omega_S)$. The two level system involved in the stimulated Raman emission is described by an amplitude and a relative population change, equivalent to the off-diagonal and diagonal elements of the density matrix [12]. Under stationary conditions, an exponential amplification of an initial Stokes intensity $I_S(0)$ can be derived:

$$I_S(z) = I_S(0) \cdot e^{\gamma z} \qquad (3.21)$$

where $I_S(z)$ is the amplified Stokes intensity after passing the length z, and γ is the gain coefficient which includes the Raman polarizability, the dephasing time of the Raman line and the incident laser intensity.

For laser intensities of 10^9 W/cm^2, which are normally achieved for focused picosecond pulses, a gain coefficient $\gamma \cong 1$ cm^{-1} is obtained.

By using ultrashort laser pulses having a duration comparable with the Raman dephasing time, the interaction is less effective and deviations from Eq. (3.21) occur. In this case, higher pump intensities are required to obtain a good gain coefficient.

It should be pointed out that by using ultrashort laser pulses for generating SRS, the Raman amplification is often accompanied by other competing nonlinear effects like self-focusing and self-phase modulation.

Intense stimulated Raman emission has been observed in various liquids, liquid mixtures and crystals [13-16], with conversion efficiencies up to 50%. Even higher conversion efficiencies and a better pulse quality were obtained for several high pressure gases for both vibrational and rotational transitions [17, 18].

3.1.6. The pump-probe technique

A frequently used method in the time-resolved spectroscopy for investigating transient species is the pump-probe method. A pump pulse with high energy density interacts with the molecule under investigation and excites it to a higher state. The new state is a non-equilibrium one and will tend to achieve the potential energy minimum by relaxation. A second probe pulse of low energy density tuned to a wavelength so that it will be able to monitor the molecule in the new state, is spatially overlapped with the pump pulse with an adjustable delay time. By changing the delay between the pump and probe, one can monitor the changes taking place in the molecule. The characteristic spectra obtained from these transient species give specific information about the dynamics and changes in the molecular structure during the transition. The delay between the two pulses can be easily changed by varying the optical path for one of the two pulses with the help of delay lines which can achieve 1 μm resolution. For example, in air the light waves need ca. 3.3 ps to propagate through 1 mm and ca. 3.3 fs through 1 μm.

The excitation of the sample molecules with ultrashort (femtosecond) pump pulses creates coherent vibrational excitation of the Franck-Condon-active modes which have a period of vibration comparable or longer than the duration of the laser pulse. The delayed probing pulse monitor the subsequent dynamics of these vibrational modes. If the pump laser is resonant to an optically-allowed electronic transition in the molecule, coherence is generated in both ground and excited state vibrational manifolds. The theoretical treatment of the coherent effects visible in femtosecond pump-probe experiments has been done by Pollard et. al. in a series of papers at the beginning of the 90’s [19-22]. In these papers, the pump-probe experiments are described in terms of time-dependent overlap of bra and ket wave-packets generated by the pump and probe pulses, respectively [19-21]. Experimentally, the coherent effects are seen as oscillations in time of the measured spectroscopic property (for example transient absorption). These oscillations decay, in solutions, on a fs to ps time scale, due to anharmonic coupling to other vibrational modes.

In experiments with pulses of picosecond duration, coherent effects do not play a major role, and for the interpretation of the pump-probe time-dependent results an incoherent treatment under the form of rate equations can be used, as presented in the following.

Taking the cross-correlation between the pump and the probe lasers as $l(t)$, and the time-evolution of the system $r(t)$, it is possible to write the measured response function of the system in the form of a convolution function:

$$S(t) = \int_{-\infty}^{\infty} l(t') \cdot r(t-t') dt' = \int_{0}^{\infty} l(t-t') \cdot r(t') dt' \qquad (3.22)$$

If the time scale of the process under investigation is much larger than the pulse duration, the laser pulses can be approximated with δ-functions. In this case, the time response of the system can be simplified to a sum of exponential functions:

$$S(t) = \sum_i c_i e^{\alpha_i t} \qquad (3.23)$$

In particular, the measurement procedure for time-resolved resonance Raman and CARS spectra of transient species or excited states follows the scheme:
(i) excitation of the molecule in the absorption band for preparation of the transients,
(ii) probing of the transients by resonance Raman or CARS, i.e., the probe laser wavelength is chosen to match an absorption band of the respective transient.

The time resolution in the experiment is, for picosecond pulses, limited only by the duration of the laser pulses, i.e., by their cross-correlation time. Group velocity dispersion of the laser pulses does not play a role in this case.

3.2. Experimental set-up

3.2.1. Generation of the picosecond laser pulses

3.2.1.1. The synchronously pumped dye laser

If a laser active medium is excited and the laser medium is placed between two parallel mirrors, a set of frequencies will oscillate depending on the gain bandwidth and the loss in the cavity. Transversal and longitudinal modes can be observed as field distribution normal to the resonator axis and an infinite set of eigenfrequencies separated in frequency by c/2L, respectively, where L is the optical length of the cavity and c the speed of light. If the longitudinal modes are somehow forced to maintain a fixed phase and amplitude relationship, the laser output will consist of trains of regularly spaced pulses, which are called mode-locked pulses. These pulses have a temporal width which is approximately equal to the reciprocal of the spectral bandwidth, and a temporal periodicity equal to 2L/c. To give an example, for a resonator length of 2 m, pulses of about 100 ps duration will be generated with a periodicity of 76 MHz. These values are very similar with the parameter values of the Nd:YAG mode-locked laser used for the experiments carried out in our laboratory.

Two methods are used for mode-locking: (i) active mode-locking, which means sinusoidal modulation of phase or loss by active elements (for example acousto-optical crystals) introduced into the optical cavity that are driven at the frequency corresponding to the mode spacing, and (ii) passive mode-locking, where saturable absorbing elements (dyes or even gases and solids) are inserted in the cavity.

A very successful method used for a long time for generation of tunable picosecond pulses is the synchronously mode-locking of dye lasers. Synchronous mode-locking is a method of actively mode-locking, where mode-locking is achieved by pumping with a mode-locked laser [23]. Because the modulation of the gain medium by the short pumping pulse provides the coupling mechanism, it is very important to carefully match the cavity lengths of the pump and dye lasers. In this way, the gain of the dye laser is modulated at a cavity round trip. The rise time of the gain modulation is approximately equal with the time integral of the pump pulse, and is thus more effective in mode-locking than the sinusoidal loss modulation.

The laser close to threshold saturation switches the gain off, and consequently, the pulse duration of the dye pulse will be much shorter than that of the pump laser.

In fact, the first observation of synchronous mode-locking in Rhodamine-6G was made by Soffer et al. in 1968 [24] by using a mode-locked Nd:glass laser as an optical pump. The same procedure was later used by numerous groups (see for example [25]) to produce tunable picosecond pulses from dye lasers, and has also been used for the experiments presented in this thesis.

A continuous-wave Nd:YAG laser (Quantronix 4216) was mode-locked by an acousto-optical loss modulator, giving rise to pulses of 1064 nm with a duration of about 100 ps - measured with a fast photodiode - at a repetition rate of 76 MHz. These pulses were further frequency doubled in a KTP crystall to 532 nm and used for synchronously pumping a dye laser. Tunable dye laser pulses with energies up to 1 nJ/pulse were generated with the same repetition rate as the pumping laser. The duration of these pulses was measured with a procedure described in the next paragraph.

3.2.1.2. Characterization of the synchronously pumped dye laser pulses

In every time-resolved experiment it is important to know the duration of the laser pulses. For the experiments carried out here, the auto-correlation technique is applied.

The laser radiation is split into two beams of equal intensity, with the help of a beam-splitter. The two beams take different optical paths relative to each other, before they are focused onto a nonlinear crystal under phase-matching conditions. By nonlinear mixing of the two radiations, the second harmonic is generated. The time evolution of the new frequency is the correlation function of the two incident radiations:

$$I_{SHG}(t) \approx \int_{-\infty}^{\infty} I(t-t')I(t')dt' \qquad (3.24)$$

The SHG signal can be monitored on an oscilloscope. By calibrating the divisions on the oscilloscope, it is possible to determine the correlation width defined as the Full Width at Half Maximum (FWHM). The real pulse duration can be further obtained from Eq. (3.24), with the pulse shape characteristic in each particular experiment. For example, in the case of Gaussian pulses, the pulse duration is given by the correlation width divided by the factor 1.44 [9].

The duration of the pulses obtained in our experiment is 1.5-8 ps, depending on the mismatch between the cavities of the Nd:YAG and dye laser lengths.

3.2.1.3. Amplification of mode-locked picosecond light pulses

The picosecond pulses obtained from a synchronously pumped dye laser do not exceed 1 nJ/pulse in energy. Instead, pulses up to 200 μJ are required in our experiment, and this demands for amplification of these pulses.

The dye amplifier build in our laboratory has been realized according to the design made by Perry et al. [26] and Dolce et al. [27]. It consists of three dye cells of 1, 4 and 10 mm length in the first, second and third stage, respectively, pumped by the second harmonic of a 50 Hz Nd:YAG regenerative amplifier (Continuum RGA-50).

The dye concentrations were approximately 1x10^{-3}, 2.5x10^{-4} and 1x10^{-4} M/l, and the pumping beam diameters approximately 0.5, 3 and 8 mm in the first, second and third stage, respectively. Variable delay lines composed of prisms mounted on translation stages are used to maintain precise timing of the pump pulse and the dye pulse in each stage. By carefully choosing the dye in each cell, the amplifier is tunable from 575 to 610 nm, when using rhodamine 6G for the seed laser, and from 680 to 740 nm, when using pyridine2 in the seed laser. To reduce the contribution of Amplified Spontaneous Emission (ASE) to the amplified signal, in the third stage a dye has been used which has the maximum of absorption band shorter than that of the dyes in the first and second stages. For example, to obtain a maximum of amplification at 600 nm with an ASE contribution lower that 5%, sulphorhodamine 101 was used in the first and second stages, and sulphorhodamine B in the third stage. The total amplification is about 2x10^5, which is distributed over the individual stages as follows: 1x10^3 in the first, 33 in the second and 6 in the last stage.

Picosecond pulses up to 200 µJ energy per pulse are obtained after amplification.

3.2.2. CARS set-up

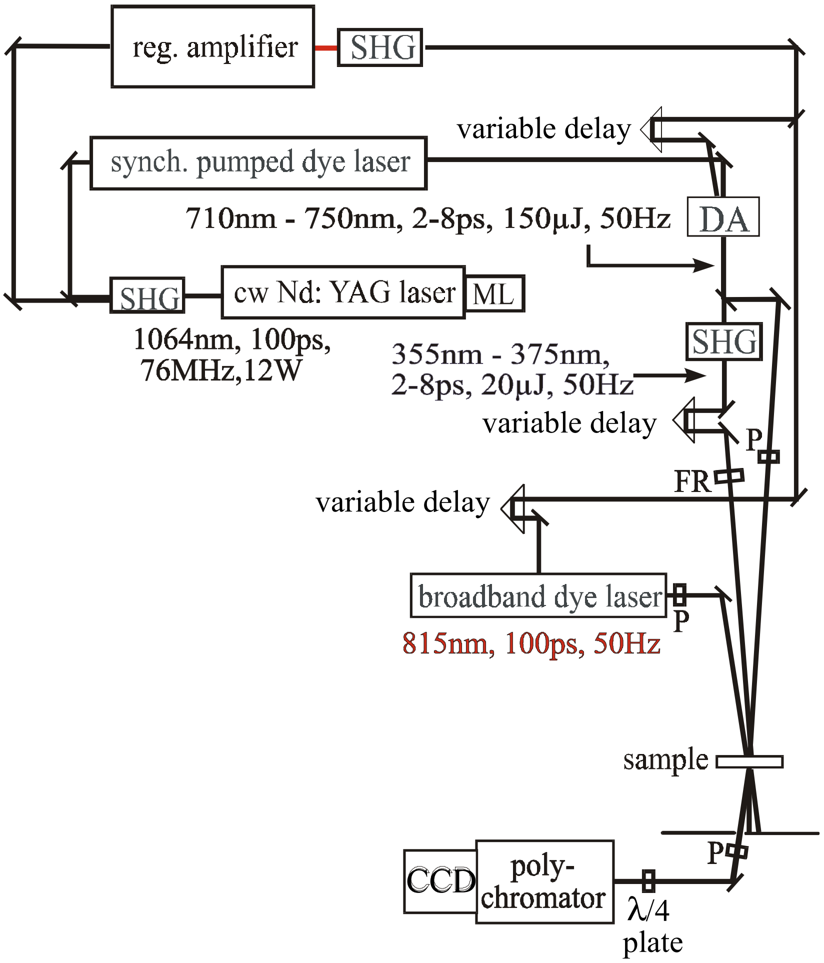

Fig. 3.7: Picosecond time-resolved CARS spectrometer. DA is a three-stage dye amplifier, FR is a Fresnel romb, P is polarizer, F symbolized filter and CCD is a Charge Coupled Device.

The experimental apparatus used for CARS measurements is presented in Fig. 3.7. The frequency doubled radiation of about 100 ps time duration at 532 nm originating from the mode locked Nd:YAG laser is used for synchronously pumping a dye laser, which delivers pulses of 1.5-8 ps with 76 MHz repetition rate at 710 nm (with pyridine2 as laser dye). These pulses were amplified up to 200 μJ by the three stage dye amplifier described in the preceding paragraph.

For photoexcitation of the DPH sample, either pulses of the frequency doubled dye laser radiation or the third harmonic of the regenerative amplifier were used. For CARS generation, a small portion (5 %) of the dye laser pulse was mixed with the radiation of a broad band dye laser which was directly pumped by the second harmonic of the regenerative amplifier. Broad band CARS signals obtained in this way were recorded, after spatial filtering and dispersion by a polychromator (SpectraPro 275, focal length 275 mm, with a 2400 l/mm or with a 1200 l/mm grating), with a liquid nitrogen cooled CCD-camera (Spectroscopy and Imaging, LN/CCD 1100PB/UVAR CCD, backilluminated).

Spectra were recorded without and with additional UV radiation, with different delays between UV excitation and CARS probing. In addition, CARS spectra of a thin (0.5 mm) glass plate were recorded. In the frequency range 1000 cm^{-1} - 2000 cm^{-1} this CARS spectrum is dominated by the constant electronic contribution of glass γ. Consequently, it reproduces the spectral distribution of the broad band dye laser. All the spectra are normalized to this reference.

The investigations were carried out with parallel polarization between all beams. For determination of frequencies of very broad vibrational bands and of the depolarization ratios of the CARS resonances, the polarization-sensitive CARS scheme was applied, as described in 3.1.3.2 [7, 8, 28], to suppress interference with the electronic background in the spectra. For an improved suppression of the Raman-nonresonant background, we used an additional phase compensator (λ/4 plate) in front of the analyser to minimize residual ellipticity of P^{NR}.

3.2.3. Raman set-up

Both stationary resonance Raman scattering, as well as time-resolved anti-Stokes resonance Raman measurements, were carried out with a spectrometer based on the picosecond dye laser system used for the CARS measurements (see Fig. 3.8). The difference is that the dye used in the synchronously pumped dye laser was rhodamine 6G, which provides pulses at 606 nm with spectral width of 15-20 cm^{-1} (FWHM) and 3.2 ps duration. The pulses were amplified by the three stage dye amplifier described in paragraph 3.2.1.3, resulting in an energy per pulse of approximately 150 μJ. Pulses of 10 μJ were generated at 303 nm by frequency doubling in a BBO crystal of 2 mm length. The signal detection was the same as for the CARS set-up, with the difference that for Raman spectra with 606 nm excitation a notch filter was placed in front of the polychromator to reduce stray light originating from the laser beam. Raman spectra with 303 nm excitation were recorded without additional spectral filtering. The spectral resolution is mainly limited by the spectral width of the probe pulse (15-20 cm^{-1} for 606 nm and 20-30 cm^{-1} for 303 nm excitation, respectively).

Stationary Stokes Raman spectra were recorded in quartz cells (10x10 mm^2) without stirring. Time-resolved Raman spectra were recorded in free flowing jets of 0.1 mm thickness (for ethanol and propylene carbonate solutions) or of 0.3 mm thickness for the glycerol triacetine solution. The energy of the probe pulses used for recording the Raman spectra of B-30 solutions was below 10 µJ. In order to avoid multiple interaction with individual molecules, the pump beam was focused onto the sample by a cylindrical lens resulting in a relatively large irradiated area of about 0.15x1 mm^2. At tenfold lower energies of the probing pulses (<1 µJ) we checked possible changes in the Raman pattern compared to the higher energy level. No such changes were observed, confirming that contributions from populated excited electronic states were negligible. Spectra were accumulated up to 200 seconds.

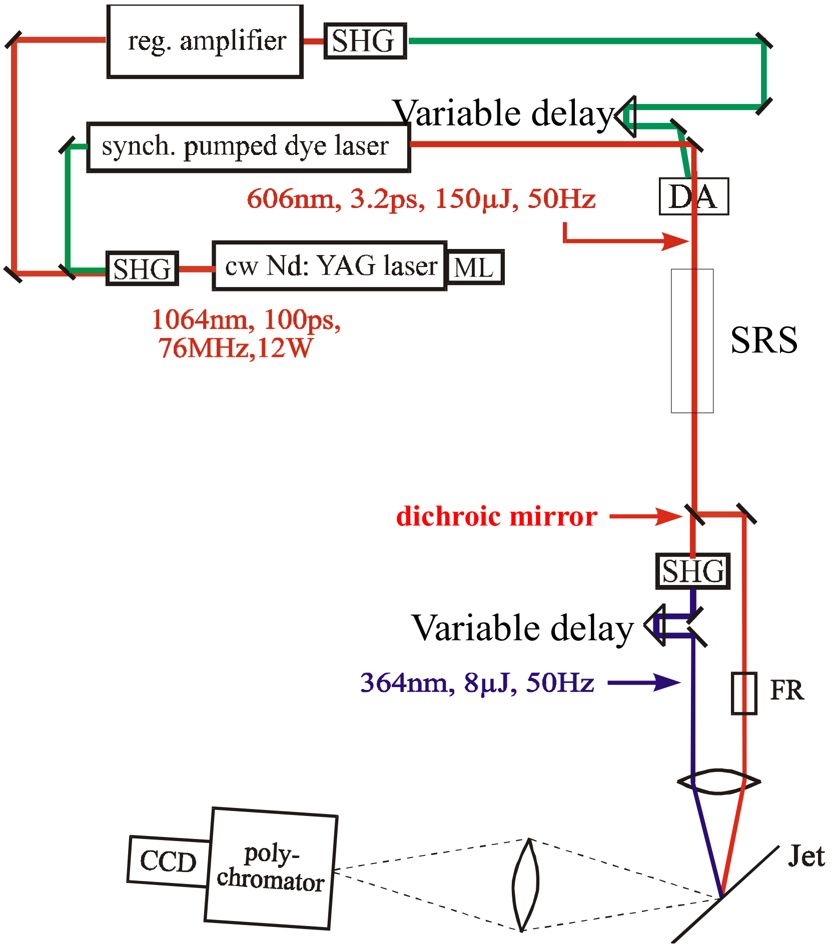

Fig. 3.8: Picosecond time-resolved Raman spectrometer. DA is a three-stage dye amplifier, FR a Fresnel romb, P polarizer, F filter and CCD is a Charge Coupled Device. SRS is the cell for new frequency generation by Stimulated Raman Scattering .

Measurements of the Raman spectra in the excited singlet state of B-30 need the extension of the pump and probe wavelenghts. This was realized by using the SRS effect. Using methane under high-pressure (60 bar), stable laser emission shifted with 2917 cm^{-1} by the first Stokes component of the methane gas was obtained. A conversion of about 50% from the 600 nm incident laser to the 740 nm SRS output has been achieved. This radiation was further frequency doubled in a BBO crystal of 2 mm length. In this way, pulses of about 5 µJ were generated at 370 nm.

3.2.4. Measuring of the time resolution in the experiment

The time resolution in the experiment was measured with the cross-correlation method. This method is similar with the auto-correlation method which was described in paragraph 3.2.1.2. The difference is that by the cross-correlation method two pulses of different colors are mixed resulting in a signal which depends on the time-delay between the respective pulses.

Cross-correlation traces of pulses of different wavelengths were measured by recording the time-resolved stimulated emission from a solution of sulforhodamine 101 in methanol excited by the 303 nm pulses. The small signal amplification $-\Delta A = \log(T/T_0)$ of the probe pulse at 606 nm was measured as a function of delay time relative to the pump (T, T_0: sample transmission with and without excitation, respectively). By differentiating (-ΔA), a cross-correlation width (FWHM) of about 4.9 ps has been measured. The pulse duration and the zero delay between the pump and probe pulses have been optimized by sum-frequency mixing and by optical Kerr effect in CS_2 (relaxation time ca. 1 ps).

The cross-correlation recorded by amplification in sulphorhodamine solution and by sum-frequency mixing in a KDP crystal are shown in Fig. 3.9.

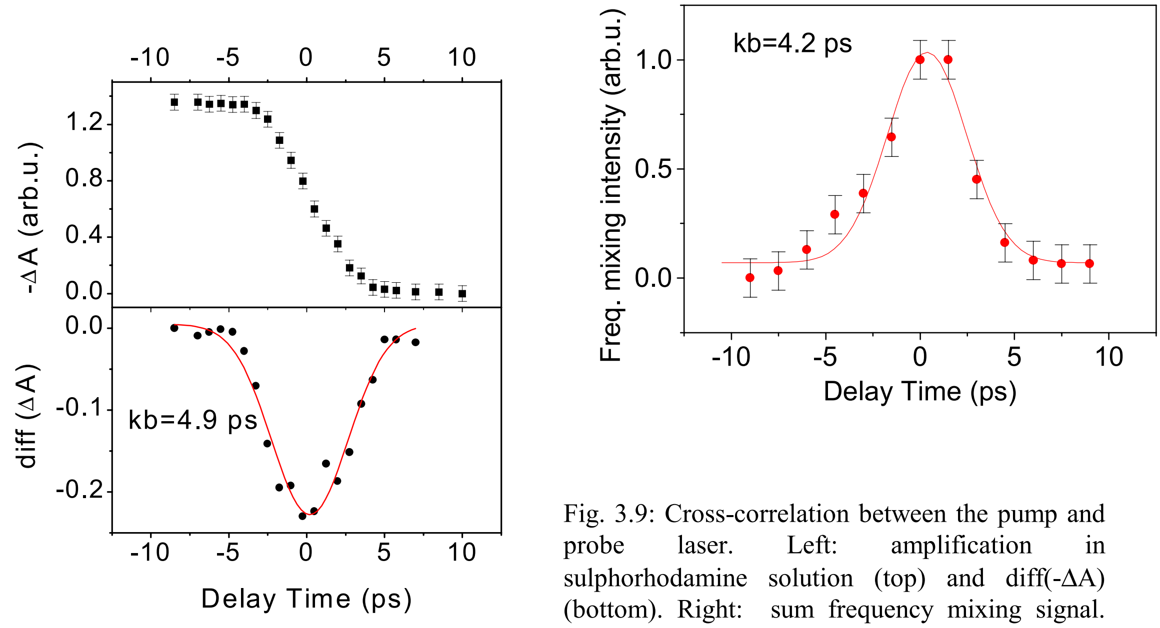

Fig. 3.9: Cross-correlation between the pump and probe laser. Left: amplification in sulphorhodamine solution (top) and diff(-ΔA) (bottom). Right: sum frequency mixing signal. Solid lines represent the fit with Gaussian expressions. Cross-correlation values are given in the inserts.

References

[1] R. W. Boyd, in *„Nonlinear Optics"*, Academic Press, New York (1992)

[2] J. A. Koningstein, in *„Introduction to the theory of the Raman effect*", D. Reidel Publishing Company Dordrecht-Holland (1972)

[3] J.W. Nibler and G.V. Knighten; in *"Raman Spectroscopy of Gases and Liquids"*, Topics in Current Physics 1, ed. A. Weber, (1979) 253

[4] M. Pfeiffer, A. Lau, W. Werncke; *J. Raman Spectrosc.* **15** (1984) 20

[5] J.W. Fleming, C.S. Johnson; *J. Raman Spectrosc.* **8** (1979) 284

[6] M. Pfeiffer, A. Lau, W. Werncke; *J. Raman Spectrosc.* **17** (1986) 425

[7] J.L. Oudar, R.W. Smith, Y.R. Shen, *Appl. Phys. Lett.* **34** (1979) 758.

[8] S.A. Achmanov, A.F. Bunkin, S.G. Ivanov, N.I. Koroteev, *Sov. Phys. JETP* **47** (1978) 667

[9] Laubereau, in *„Ultrashort Laser Pulses - Generation and Applications"* editor W. Kaiser, Topics in Applied Physics, Volume **60** (198) 37

[10] W.H. Glenn, *IEEE J. QE*-**5** (1969) 284

[11] N. Bloembergen, *Am. J. of Physics*, Vol. 35, No.**11** (1967) 989-1023

[12] J.A. Giordmaine and W. Kaiser, *Phys Rev* **144 (**1966) 676

[13] S. L. Shapiro, J. A. Giordmaine, K. W. Wecht, *Phys Rev Lett* **19 (**1967) 1093

[14] C. G. Brett, , H. P. Weber, *IEEE J. QE*-**4** (1968) 807

[15] M. J. Colles, *Opt. Commun.* **1 (**1969) 169

[16] J. R. Maple, J. T. Knudtson, *Chem. Phys. Lett* **56** (1978) 241

[17] M.E. Mack, R. L. Carman, J. Reintjes, N. Bloembergen, *Appl. Phys. Lett.* **16** (1970) 209

[18] I. R. Loree, , C. D. Cantrell, D. L. Barker, *Opt. Commun.* **17** (1976) 160

[19] W.T. Pollard, C.H. Brito Cruz, C.V. Shank, R.A. Mathies, *J. Chem. Phys.* **90** (1989) 199

[20] W. T. Pollard, S. Y. Lee, R. A. Mathies, *J. Chem. Phys.* **92** (1990) 4012

[21] W. T. Pollard, H. L. Fragnito, J. Y. Bigot, C. V. Shank, R .A. Mathies, *Chem. Phys. Lett.* **168** (1990) 239

[22] W. T. Pollard, S. L. Dexheimer, Q. Wang, L. A. Peteanu, C. V. Shank, R.A.Mathies, *J. Phys. Chem.*, **96** (1992) 6147

[23] D. J. Kuizenga, A. E. Siegman, in *„FM and AM Mode-Locking of the Homogeneous Laser"*, *IEEE J. Quantum Electron.* **QE-6** (1970) 694

[24] B. H. Soffer, L. W. Linn, *J. Appl. Phys.* **39** (1968) 5859

[25] L. Goldberg, C. Moore, *Appl. Phys. Lett.* **27** (1975) 217

[26] M. D. Perry, O. L. Landen, J. Weston, and R. Ettlebrick, *Optics Lett*. **14** (1988) 42

[27] W. Dolce, B. Yang, M. Saeed, L. F. DiMauro, and G. Scoles, *Appl. Phys. B* **56** (1993) 43

[28] N. I. Koroteev, A. P. Shkurinow, B. N. Toleutaev; in *„Coherent Raman Spectroscopy“*, ed. G. Marowski, V.V. Smirnow, Springer Proceedings in Physics 63; Springer Verlag (1992) 186

4. Vibronic coupling in the first excited singlet state of DPH

4.1. Motivation

Diphenylpolyenes belong to the class of polyenes, and they are very interesting as they can serve as models for retinoids and carotenoids. The physiological function of these pigments is triggered by its photoexcitation and include isomerization and energy transfer. Efficient utilization of a limited number of photons, as well as dissipation of excess energy delivered by photons, are here of primary importance. Coupling between the electron and nuclear motions is the main mechanism which assure the functionality of these molecules.

In particular, diphenylhexatriene (DPH) is one of the most widely used fluorescent probes in studies of biological membranes [1]. A high fluorescence quantum yield in hydrophobic environments, but negligible fluorescence in water, as well as a lifetime of the excited state dependent of the environmental properties, makes this molecule very attractive for studies regarding the membrane's role in the cell life.

Another interesting property of diphenylpolyenes is their high third order optical nonlinearity γ in the electronic ground state, which can be further increased after electronic excitation [2-4]. These properties, and the very fast response time of the nonlinearities (which are related to the delocalization of the π-electron systems in the molecules), make them interesting from technological point of view.

Another interesting feature of diphenylpolyenes, related to their functionality, is the reversal of the 1^1B_u and 2^1A_g levels as the lowest excited singlet state with increasing chain lengths and an increasing gap between the two states for longer polyenes [5,6] (Fig. 4.1). In trans-stilbene (TS), the primarily excited 1^1B_u state also represents the lowest excited singlet state. In DPH, however, the 2^1A_g state is located slightly below the 1^1B_u state [7] with a small gap depending mainly on solvent polarizability [7,8]. In DPO, the 2^1A_g - 1^1B_u gap amounts to approximately 2000 cm^{-1} [7,9]. It grows with increase of the polyene chain length. The optical transition between the 1^1A_g and the 2^1A_g electronic states is forbidden (see Paragraph 2.1.3). Consequently, photoexcitation of the 2^1A_g state is possible only via 1^1A_g - 1^1B_u excitation, which is optically allowed.

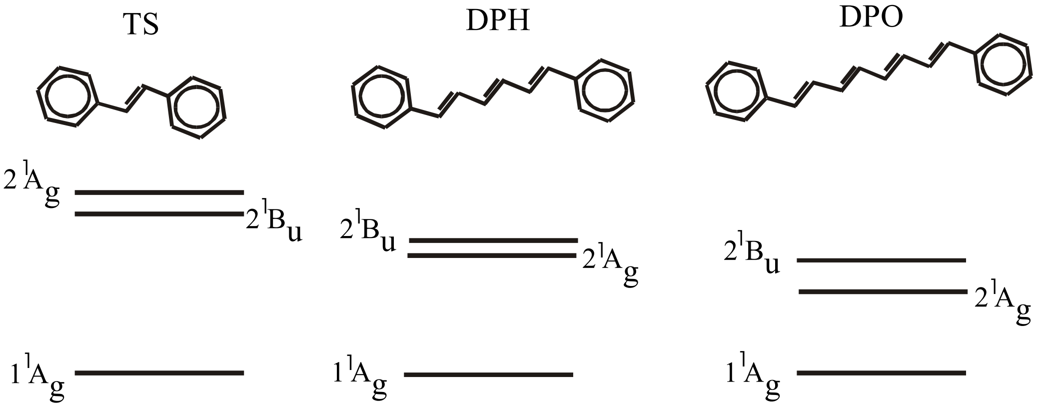

Fig. 4.1: Molecular structure and ordering of the three lowest electronic levels in trans-stilbene (TS), diphenylhexatriene (DPH) and diphenyloctatriene (DPO).

Since for about twenty years it is known that the totally symmetric C=C stretching vibration of the polyenic chain strongly couples the 1^1A_g and 2^1A_g electronic states [7-12], which represent - for polyenes longer than butadiene- the S_0 and S_1 states, respectively. Vibronic coupling causes the vibrational frequency of this vibration in the S_0 state to be shifted down and in the S_1 state to be shifted up by an amount of ca. 100 cm^{-1}. These anomalously strong shifts beyond the range of the C=C stretching frequencies can be described without assuming any changes of the corresponding bond orders, and are explained by vibronic coupling between the two electronic states [11].
Recently, it has been shown quantitatively that the radiationless 2^1A_g - 1^1A_g transfer rate in β-carotene is directly related to the vibronic coupling strengths of the C=C stretching mode to the electronic transition, i.e. vibronic coupling plays a dominant role in 2^1A_g - 1^1A_g internal conversion [12]. Internal conversion between the primarily optically pumped 1^1B_u (S_2) level to the 2^1A_g (S_1) level is even faster than the 2^1A_g - 1^1A_g transfer, occurring on a femtosecond time scale [13]. The mechanisms involved in this fast transfer are not fully understood [14]. The energy gap between 1^1B_u and 2^1A_g is much smaller than that between 2^1A_g and 1^1A_g favoring vibronic coupling effects. However, in symmetric polyenes, coupling of these two excited states by an a_g mode, e. g., by the totally symmetric C=C stretching mode, should not be effective because of symmetry reasons. In contrast, it has been shown that in diphenylbutadiene investigated in gas phase, the optically forbidden transition between 1^1A_g and 2^1A_g gains oscillator strength from the allowed 1^1A_g - 1^1B_u transition via 1^1B_u - 2^1A_g vibronic coupling by a low frequency b_u mode [15]. Consequently, asymmetric low frequency modes should be taken into account for 1^1B_u - 2^1A_g vibronic coupling in other polyenes, too. On the other hand, 1^1B_u - 2^1A_g vibronic coupling effects by the totally symmetric C=C stretching vibration of the chain have been observed in the first excited state of asymmetric polyenes, as well as in β-carotene [16]. For this molecule, which is assumed to belong to the C_{2h} symmetry group in the ground state, it has been argued that in the first excited singlet state, symmetry distortions may occur. Therefore, the observed coupling effects were explained as a result of deviation from the symmetry.
Because of their chemical stability, diphenylpolyenes are very suitable as models for studying vibronic coupling [17, 18]. Like in other (not too short) polyenes, the optically accessible 1^1B_u state (S_2) is located above the 2^1A_g electronic state (S_1), and the gap becomes closer with decreasing chain lengths [19]. It almost disappears in the case of DPH. Furthermore, this low gap can be tuned significantly in changing the polarizability of the solvent [20]. The latter effect occurs because the S_2 state is more polarizable than the S_1 state and changes its energy from one solvent to another, but S_1 does not. Because the energy gap between the two electronic states is one of the factors determining the strength of the vibronic coupling, the S_1-S_2 coupling should be influenced by changing solvents, while the S_0-S_1 coupling should remain nearly unchanged.
In DPH the trans-cis-trans (tct)- and cis-trans-trans (ctt)-photoisomers have been isolated as primary photoproducts [21], and it has been reported that the yield for isomerization increases in polar solvents [22]. As a consequence, the excited-state geometries determining the pathways of photoisomerization should be affected significantly by solvent polarity.

The excited singlet states of DPH populated after photoexcitation have been mainly investigated by time-resolved fluorescence [23,24] and transient absorption spectroscopy [25-27]. However, both the assignments of the transient absorption bands, as well as the kinetics towards an excited-state equilibrium mixture, are still the subject of controversy. It is very difficult to obtain any structural information from the broad and structureless bands of the excited-state absorption of DPH. Alternatively, vibrational spectroscopy is suitable for determining the structure of the probed state.

We use time-resolved resonance CARS and polarization CARS for the study of the excited electronic states of DPH, in order to:

i) get structural information about the excited states in different environments. This is achieved by combining our experimental results with a normal coordinate analysis on a semi-empirical PM3 level;

ii) determine the time duration until equilibrium between the excited electronic states has been established;

iii) get information about the mixing character between the two excited electronic states.

4.2. Photophysics of DPH

The molecular structure of DPH, together with the excitation and probe scheme, is depicted in Fig. 4.2. The molecule is a linear polyene with three double bonds and two terminal phenyl rings, and belongs to the C_{2h} point symmetry group. The delocalization of the π-electron system along the chain gives rise to a large value of the second-order hyperpolarizability γ. On the other hand, the existence of an inversion center determines the zero-value (in the dipole approximation) of the hyperpolarizability β. The lowest band in the absorption spectrum (Fig. 4.3) is due to the S_0-S_2 transition near 350 nm. That means in molecular orbital language the promotion of a single electron from the highest occupied molecular orbital (HOMO) to the lowest unoccupied molecular orbital (LUMO). The existence of an 2^1A_g state below the 1^1B_u state has been established by many high resolution one- and two-photon spectroscopic studies on samples at low temperature [7]. For room temperature solutions, the 1^1B_u state is only slightly higher in energy than the dipole forbidden 2^1A_g state, and should be thermally repopulated. This is the reason for observing a weak fluorescence emission from the 1^1B_u state. Deactivation of the optically active 1^1B_u state to the lowest excited 2^1A_g state occurs on a 500 fs time scale, as being determined by the changed transient absorption signal near 650 nm [28] (see also Fig. 4.2). The assignment of this transient absorption around 650 nm to excited state electronic transitions is not fully elucidated. Assignments to both the 2^1A_g - n^1B_u as well as the 1^1B_u - n^1A_g transitions have been reported [25, 28], and it has been argued that the lowest excited singlet has some B_u character as well [22]. The gap ΔE between the two excited states is about 1000 cm^{-1} [29] and can be varied by about 500 cm^{-1} in choosing solvents with different polarizability α [20]. The lifetime of the lowest excited electronic state has been measured by time-resolved fluorescence spectroscopy, showing a single exponential decay with $\tau = 13.1$ ns in cyclohexane solution [1].

In Fig. 4.2, the wavelength for photoexcitation (λ_{UV}) and the frequencies for CARS probing ($\omega_1, \omega_2, \omega_3$) near the transient absorption around 650 nm are shown schematically. CARS probing is carried out at the transient absorption band, to obtain selective resonance enhancement for the detection of vibrations originating from the excited electronic state.

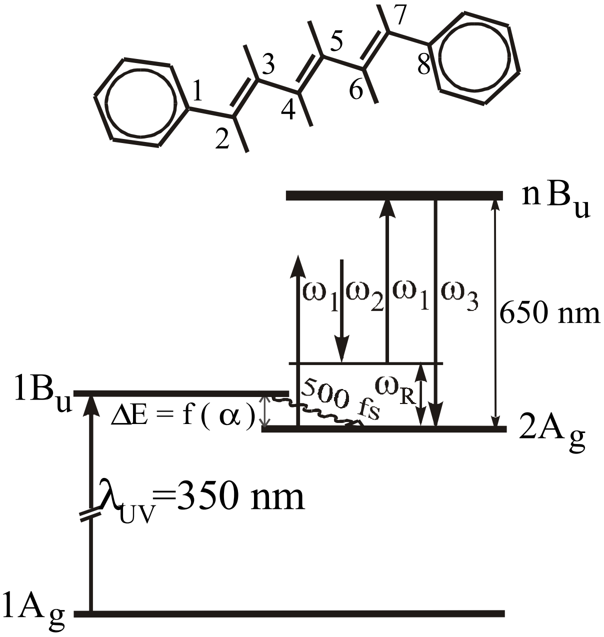

Fig. 4.2: Molecular structure of diphenylhexatriene (DPH). Photoexcitation to the 1^1B_u state by a pulse at λ_{UV}=350 nm and CARS probing of a vibrational resonance ω_R of the excited electronic state are illustrated. The relaxation from the 1^1B_u to the 2^1A_g state occurs in about 500 fs. For simplicity, the excited state absorption is indicated as a 2^1A_g - n^1B_u transition only.

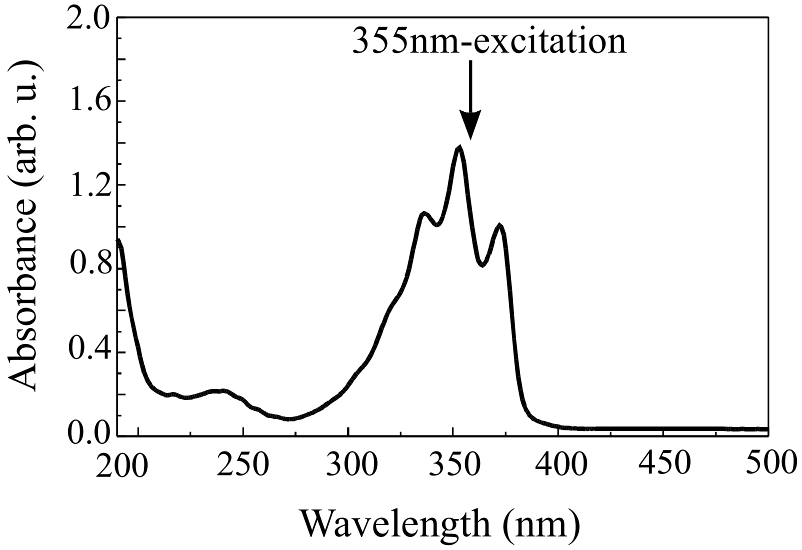

Fig. 4.3: Absorption spectrum of DPH dissolved in cyclohexane (10^{-3} M). The excitation wavelength is marked with an arrow.

In Fig. 4.3 is shown a typical absorption spectrum of DPH dissolved in cyclohexane at a concentration of 10^{-3} M.

4.3. Results

4.3.1. Raman spectra in ground state and time-resolved CARS spectra in excited states

The resonance CARS spectra presented here are obtained with the experimental set-up described in paragraph 3.2.2.

An excited-state CARS spectrum of DPH dissolved in cyclohexane (concentration 10-3 M) in the frequency range of 1000-1900 cm-1, obtained with excitation at □1 =710 nm, is shown in Fig. 4.4.a. The spectrum was recorded with a temporal pulse width of 8 ps and a time delay between excitation at 355 nm and CARS probing of 20 ps. The vibrational resonances of the excited DPH (Fig. 4.4.a) are indicated by arrows. They show pronounced dips, with an additional slight dispersion-like contribution of the shape occurring within the electronic four-wave mixing background. In contrast to the DPH ground state spectrum, where only a few intense Raman lines are located near 1200 and 1600 cm-1, a much greater variety of vibrational resonances can be observed, which are of comparable intensities (see Fig. 4.4.b). These resonances cover the whole frequency region. Obviously, in the range 1050 cm-1 - 2000 cm-1 the excited state CARS spectrum exhibits a completely changed pattern compared to the electronic ground state, indicating a changed geometry. It is interesting to observe that compared to the frequencies of the C=C stretching region around 1600 cm-1 in the electronic ground state, there are strong vibrational resonances which are either down shifted (probably as a result of a decreased C=C bond order in the excited state) or unusually upshifted (as a result of dominating S0-S1 vibronic coupling) in their vibrational frequencies. It should be noted that the solvent CARS line shapes of the solution are also affected by UV pumping, occurring on a strongly enhanced four-wave mixing background. The most surprising experimental result is, however, the observation of two "high-frequency modes" at 1620 and 1780 cm-1 marked with thick arrows in Fig. 4.4.a. These lines are extremely frequency broadened. Vibrational frequencies, intensities and line widths of the excited-state spectrum were obtained by a fitting procedure [30]. The fit was carried out in three steps:

(i) First, the CARS spectrum of the DPH solution without UV excitation was fitted.
(ii) From a fit of rather isolated solvent CARS lines, which change their shapes and their CARS line/background intensity ratio after UV excitation, the excited-state electronic hyperpolarizability of DPH has been determined.
(iii) Taking into account the electronic hyperpolarizability of DPH, as determined before, the CARS line shapes of excited-state DPH were fitted to get their frequencies and intensities.

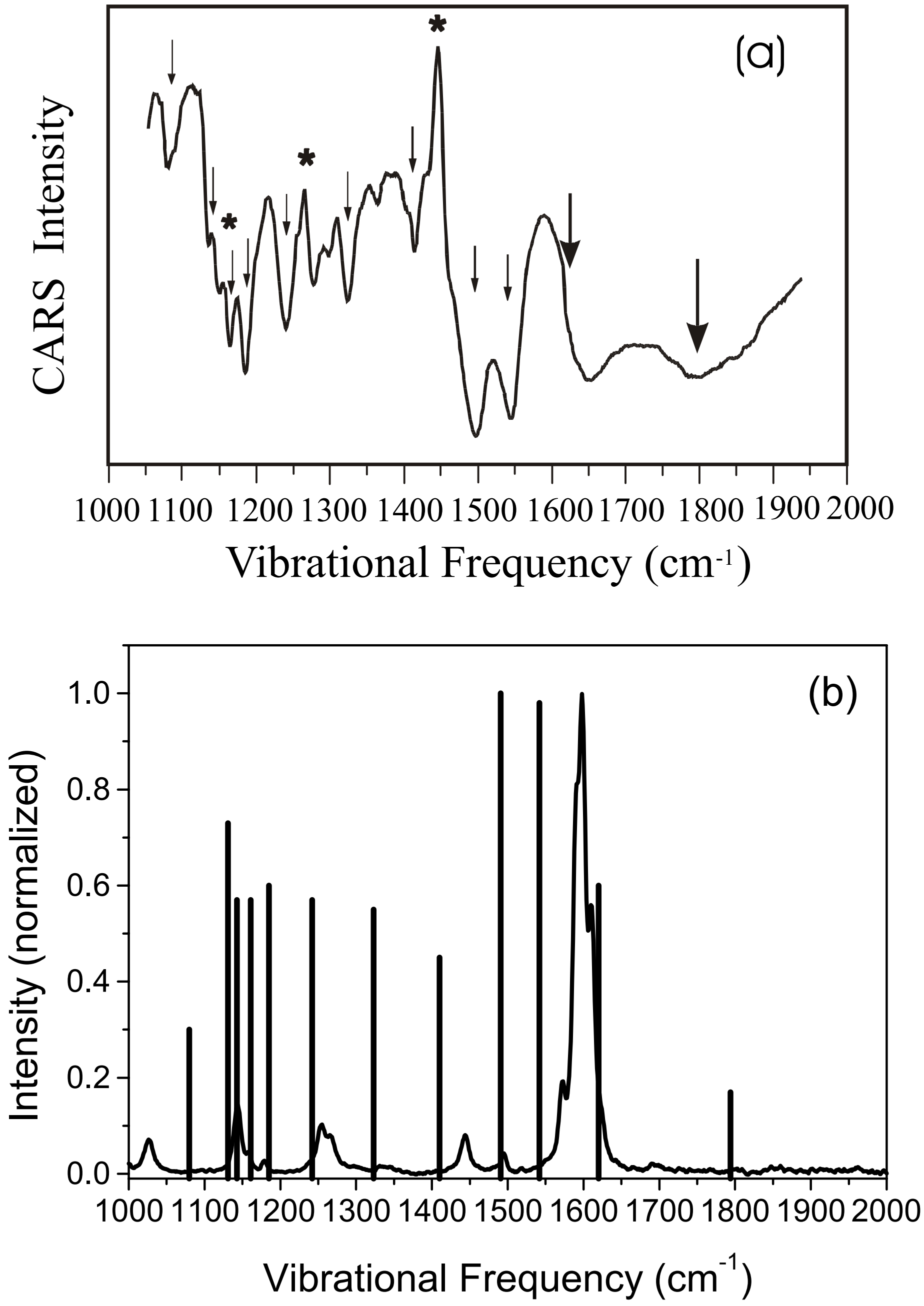

Fig. 4.4: Excited state resonance CARS spectrum (a) of DPH dissolved in cyclohexane (10^{-3} M) recorded in the frequency range 1050-2000 cm^{-1}, and the Raman spectrum of the electronic ground state (b)-solid line, together with the CARS intensities determined from fit shown for comparison in (b)-column bars.

By applying this procedure, it is possible to obtain with a good accuracy [±5 cm^{-1}] the spectral parameters of the narrow CARS resonances, marked with thin arrows in the CARS spectrum in Fig. 4.4.a. However, fitting of the broad CARS resonances above 1600 cm^{-1} contains considerable uncertainty. This fact is due to spectral drifts of the four-wave mixing background after excitation with respect to the reference spectrum, resulting in artificial changes of the shapes of the broad dips.

Fitted CARS frequencies and relative cross-sections determined in cyclohexane solutions in the frequency range of 950-2000 cm^{-1} are summarized in Table 4.2 (see paragraph 4.4.1.), and represented as column bars in Fig. 4.4.b. The corresponding spontaneous Raman data of the electronic ground state of DPH dissolved in carbon tetrachloride are given for comparison in Fig. 4.4.b. Relative Raman cross-sections are also calculated as I_{raman}/Γ_R for the Raman bands (Γ_R is here the half-width of the Raman line and R means Raman resonance) and $|\gamma^R|/\Gamma_R$ for the CARS bands (γ^R is the third-order hyperpolarizability of the CARS band) - see also 3.1.2.

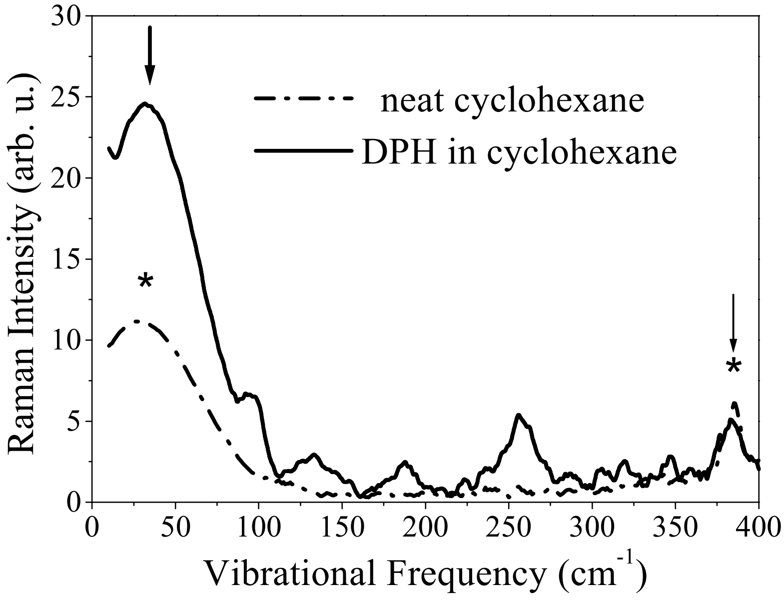

Fig. 4.5: Resonance Raman spectrum of DPH in the low-frequency range (λ_{excit}=334.5 nm), corrected for 0K with the Bose-Einstein formula. For comparison, the spectrum of the neat solvent is given. The solvent lines are marked by (*), the DPH Raman line which serves for normalizing to the solvent line is marked with a thin arrow and the DPH Raman line of interest is marked with a thick arrow.

In Fig. 4.5 the corrected resonance Raman spectrum of DPH dissolved in cyclohexane is presented, together with the Raman spectrum of neat cyclohexane. The spectra measured in the low frequency range 10-400 cm^{-1} were recorded using the 334.5 nm line of an Ar^{2+} laser for excitation. They were corrected by dividing them through the Bose-Einstein factor $n(\omega,T)+1$, in order to determine the contribution to the Raman spectrum at 0 K. Here, $n(\omega,T)$ is the thermal population of the ω-th vibrational mode, and is described by $n(\omega,T)=[\exp(\hbar\omega/k_B T)-1]^{-1}$, with and k_B the Boltzmann constant. This correction takes into account that at room temperature, for low frequency vibrations, higher vibrational levels i are populated and contribute to the Raman signal due to their high Raman cross-sections $\sigma_i = i\sigma_{i-1} = i!\sigma_0$, where σ_0 is the Raman cross-section for the lowest vibrational level.

The solvent has only a single broad peak at 29 cm^{-1} in the low frequency range. DPH gives the dominant contribution in this region with a broad low-frequency mode at 35 cm^{-1}. Additional narrower lines below 300 cm^{-1} are observed at 64, 97, 135, 187 and 257 cm^{-1}.

4.3.2. Depolarization ratios of the Raman vibrations

In order to identify the symmetry of the observed vibrations in the excited state of DPH, the depolarization ratios of the respective vibrations were determined by a polarization CARS scheme described in paragraph 3.1.3.2. The excitation has been done with circularly polarized light at 355 nm, and the CARS spectra were recorded 50 ps after excitation. The polarization CARS experiment was carried out with an angle $\phi=71.5^0$ between the planes of polarizations of the two incident laser beams by rotating the transmission plane of the analyser A (see Fig.3.4). The depolarization ratios were calculated, as described in paragraph 3.1.3.2, by finding the angle β^R where the CARS signal for the respective Raman resonance vanishes.

CARS spectra of pure cyclohexane (left hand side) and of the DPH solution ($5x10^{-4}$ M), recorded 50 ps after excitation with the 355 nm excitation pulse (right hand side), are shown in Fig. 4.6. Raman resonances are indicated by dashed lines. The spectra a, A, d, D of Fig. 4.6 have been obtained with $\Psi=0^o$ and $\Psi=90^o$, respectively. Due to cross terms between λ_R and λ_{NR} in Eq. (3.15), the strong cyclohexane vibration at 1447 cm^{-1} occurs in both spectra as a dispersion-like shaped peak within the four-wave mixing background. In contrast, the excited state CARS lines of DPH occur as slightly asymmetric dips, which are due to the close resonance with the excited state transition around 650 nm generating a complex value for λ^R. At $\Psi=35^o$, it can be seen that the lineshape of the cyclohexane vibration becomes again dispersion-like, but with an opposite sign than for $\Psi=0^o$ and $\Psi=90^o$. This feature arises because the projections λ^R and λ^{NR} at $\Psi=35^o$ (see Figs. 3.4 and 4.6.b) point to opposite directions, resulting in negative sign of the respective cross terms in equation (3.14) compared to the positive sign obtained for $\Psi=0^o$ or $\Psi=90^o$, where λ^R and λ^{NR} point to the same direction. Furthermore, the positions of peaks and minima of the excited state vibrational resonances are nearly exchanged. The strengths of the Raman resonances show a pronounced minimum at the angle $\Psi=25^o$, resulting in depolarization ratios $\rho^R \sim 0.72$ for these lines. For the solvent line at 1447 cm^{-1} the measured depolarization ratio of 0.7 is in accordance with the data reported in the literature [31]. The small peak in Fig. 4.6.c is probably due to a weak shoulder of the cyclohexane Raman line being observed in the spontaneous Raman spectrum which may be polarized differently from the main peak. Residual structures in the spectrum in Fig. 4.6.C are caused by a weak induced birefringence in the sample. Drifts in the base line are mainly due to imperfect reference spectra. Similar depolarization ratios ρ^R values of about 0.72 in the excited state of DPH were obtained in the whole frequency range under investigation (1000-1900 cm^{-1}) and are summarized in Table 4.1.

It is useful to compare these values with the corresponding values in the ground state. The determination of the depolarization ratios of the Raman vibrations in the ground state have been done for DPH dissolved in acetone (because of better solubility -

concentration $1*10^{-2}$ M) by excitation with the linear polarized light of an argon laser at 458.08 nm. The emitted Raman signal was measured in a rectangular geometry in the directions parallel and perpendicular to the direction of the polarization of the laser light, and the depolarization ratios were calculated according to $\rho = I_{||}/I_{\perp}$. The results are shown in Table 4.1.

As can be seen in Table 4.1, the vibrations in the excited states are considerably less polarized than the corresponding vibrations in the electronic ground state. A depolarization ratio below 0.75 for all the observed Raman resonances in the excited state as well as for the Raman lines in the electronic ground state indicates that the modes should be of predominant a_g symmetry in the frequency range under consideration.

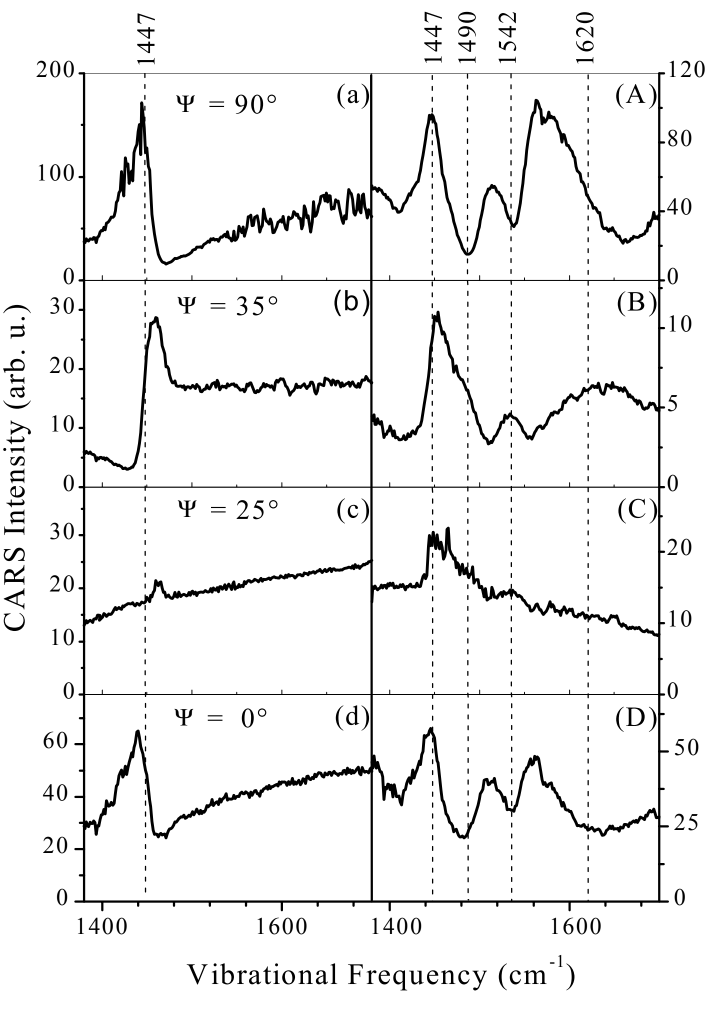

Fig.4.6: Polarization CARS spectra of cyclohexane (spectra a, b, c, d) and excited state polarization CARS spectra of DPH dissolved in cyclohexane in a concentration of $5x10^{-4}$ M (spectra A, B, C, D). The spectra of DPH have been recorded at 50 ps time delay after excitation at 355 nm with circularly polarized light. The CARS spectra were measured with an angle $\phi = 71.5^{\circ}$ between the planes of polarizations of the laser beams of the frequencies ω_2 and ω_1 respectively. Spectra were recorded with different transmission planes Ψ of the analyzer.

Table 4.1: Depolarization ratios of the electronic ground state and of the first excited state of DPH. Spectra of the electronic ground state and depolarization ratios were obtained from DPH dissolved in acetone ($1*10^{-2}$M) and measured at an excitation wavelength of 458.08nm. CARS frequencies of the first excited singlet state of DPH ($5*10^{-4}$ M in cyclohexane) were recorded with 50 ps time delay after photochemical excitation at 355nm. For CARS generation we used an excitation wave length λ_l=710nm. Depolarization ratios ρ^R of the excited electronic state were obtained in determining the planes of polarization: $\Psi=90^0-\beta^R$ for suppression of the CARS lines.

Electronic ground state		First excited singlet state	
ω_R (cm^{-1})	ρ^R	ω_R (cm^{-1})	ρ^R
		1795	0.7±0.07
		1620	0.72±0.05
1607	0.325±0.015		
1595	0.325±0.015		
1588	0.39±0.02		
1570	0.39±0.02		
		1542	0.71±0.05
		1495	0.73±0.05
		1420	0.70±0.06
		1330	0.72±0.06
		1310	0.72±0.05
		1290	0.73±0.07
1253	0.39±0.02		
		1245	0.70±0.05
		1192	0.72±0.06
1178	0.455±0.02		
		1172	0.74±0.07
1157	0.52±0.02		
		1158	0.72±0.07
1144	0.39±0.02		
		1143	0.68±0.09

4.3.3. Background free CARS measurements

4.3.3.1. Background free CARS measurements of DPH in octane

Because the exact characterization of the Raman resonances from the fit of the very broad CARS shapes is subject of some uncertainties, the polarization CARS scheme (see paragraph 3.1.3.2) has been used as an additional method to confirm the position of the two very broad CARS bands of DPH. The spectra obtained for DPH dissolved in octane without and with background suppression are presented in Fig. 4.7.a and 4.7.b, respectively. Background free CARS spectra are obtained with the plane of the analyzer A perpendicular to the polarization plane of the nonresonant background PNR (see Fig. 3.4). The strong asymmetric CARS bands (4.7.a) transforms under these conditions in almost symmetric maxima (4.7.b), which give the real vibrational frequencies like in a spontaneous Raman experiment.

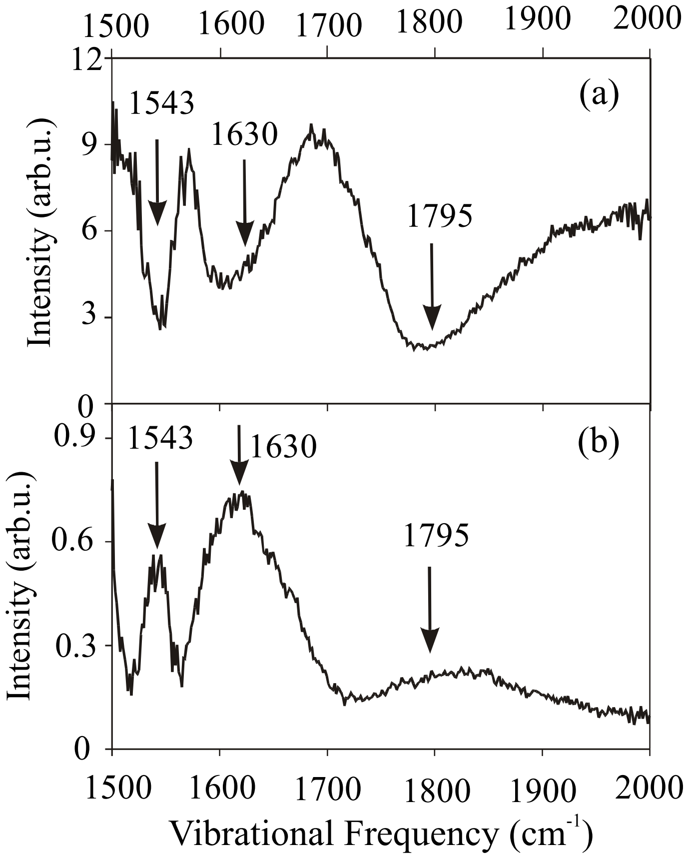

Fig. 4.7: Resonance CARS spectra of DPH in octane (5x10^{-4} M) measured under normal conditions (a) and with the background-free technique (b).

4.3.3.2. CARS measurements of DPH in different solvents

The solvent influence on the frequency of the observed Raman resonances was further studied. Six solvents (methanol, acetone, hexane, octane, cyclohexane and dimethylsulfoxide) were chosen, which differ in their polarities, viscosities, and polarizabilities. Moreover, a mixture of glycerol and methanol was prepared in the volume proportions glycerol/methanol 10%, 20%, 30% and 40%. The polarity induces a change in the dipole moment of the molecule, the viscosity makes the molecule more rigid, and the polarizability changes the energy gap between the first and second excited states.

The analysis of the spectra shows that only minor changes of the excited state frequencies (less than 10 cm^{-1}) and of the relative intensities were observed in the frequency range 1000-1550 cm^{-1} for various solvents. However, the two broad Raman resonances above 1600 cm^{-1} undergo considerable changes. Fig. 4.8 depicts the background free excited state spectra of DPH dissolved in dimethylsulfoxide and in methanol, respectively, in the frequency range 1550-1900 cm^{-1}. They show strong shifts of these broad bands.

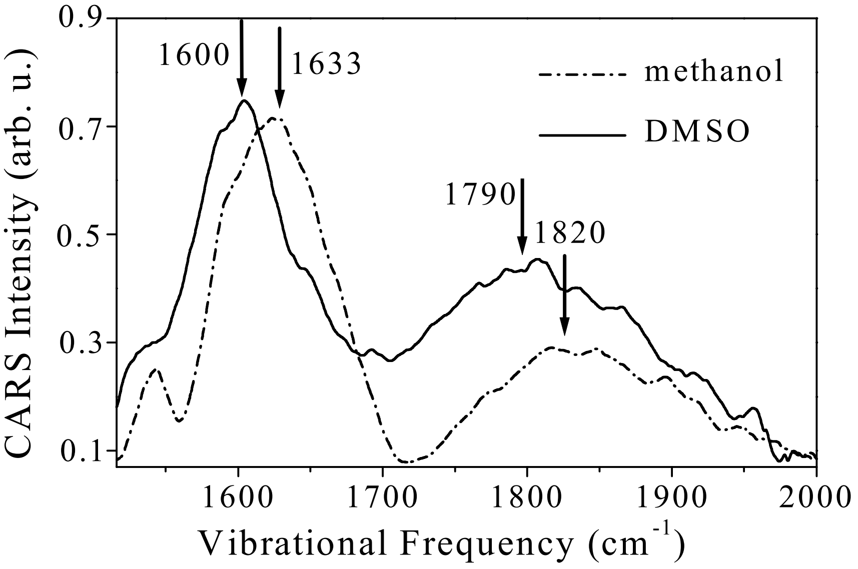

Fig. 4.8: Background-free CARS spectra of DPH after photochemical excitation obtained in the frequency range 1550-1900 cm^{-1}. Dashed line: DPH (5x10^{-4} M/l) dissolved in methanol; solid line: DPH (5x10^{-4} M/l) dissolved in dimethylsulfoxide.

A detailed analysis carried out in the six solvents mentioned before shows a clear correlation of these shifts with the solvent polarizability (Fig. 4.9) and no correlation with the solvent polarity or viscosity (Fig. 4.10).

In contrast to the shifts observed for the two vibrations in the excited singlet state, we did not observe any solvent dependent shifts of the Raman frequencies of DPH in the electronic ground state. Additionally, the vibration at 1754 cm^{-1} of the excited singlet state of DPO - the analog of the 1780 cm^{-1} band in DPH - does not show any significant frequency shift in changing the solvent. The main difference between DPO and DPH is the higher gap between the first and second excited states (about 2000 cm^{-1}) in DPO. Therefore, the shifts observed in DPH gives an indication that specific effects should occur.

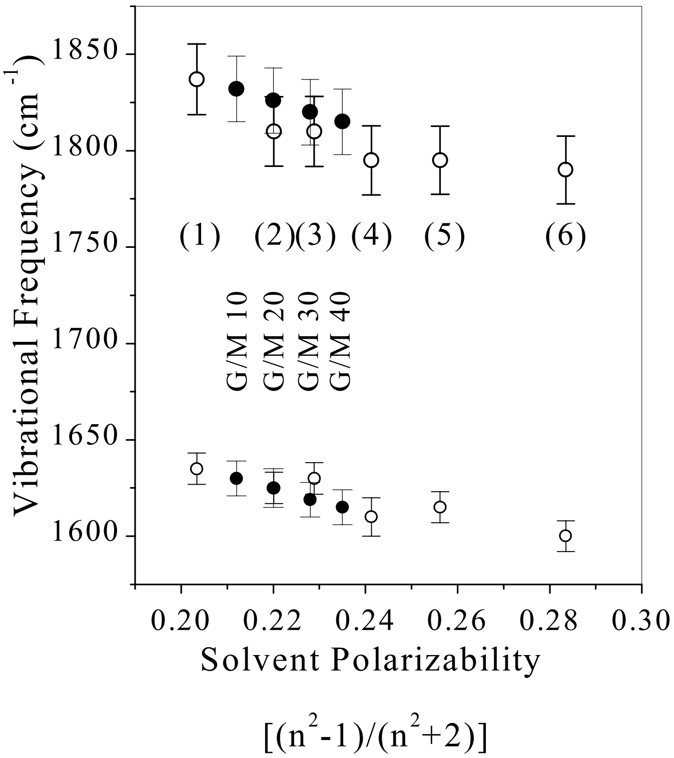

Fig.4.9: Dependences of the two high-frequency vibrations above 1600 cm^{-1} of the excited electronic state of DPH on polarizability of neat solvents (°) and of mixture of glycerol and methanol (·). The solvents used are: (1) methanol, (2) acetone, (3) hexane, (4) octane, (5) cyclohexane, (6) dimethylsulfoxide, G/M 10=10 vol% glycerol in methanol, G/M 20=20 vol% glycerol in methanol, etc.

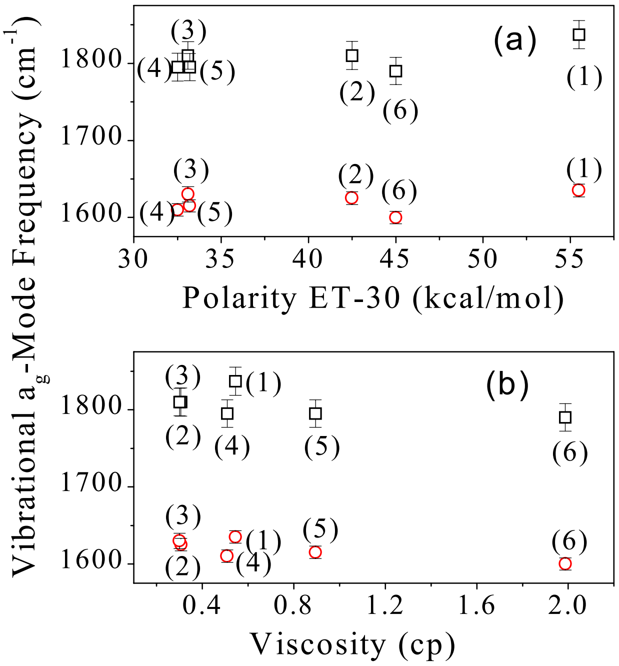

Fig.4.10: Dependences of the two high-frequency vibrations above 1600 cm^{-1} of the excited electronic state of DPH on solvent polarity (a) and viscosity (b). The solvents used are: (1) methanol, (2) acetone, (3) hexane, (4) octane, (5) cyclohexane, (6) dimethylsulfoxide.

4.3.4. Kinetics of the CARS spectra

In order to gain further information about the origin of the Raman bands in the excited singlet states of DPH, we measured the time evolution of the intensities of these bands.

Fast kinetic measurements are shown in Fig. 4.11. The CARS spectra of DPH dissolved in cyclohexane (concentration $1*10^{-3}$ M) were obtained with different time delays between the pump laser at 363 nm and the CARS probe at 726 nm. In this experiment, pulses of 2 ps duration have been used. From the spectra, it can be clearly seen that:

(i) The CARS dips grow immediately after excitation, i.e., limited by our instrumental response.

(ii) The relative intensity of the vibrational resonances does not change with the delay.

(iii) The spectra remain unchanged for long delays up to 200 ps.

These facts indicate that the Raman bands belong to the same electronic state, which should be the optically allowed 1^1B_u **and** the long living (about 13 ns) 2^1A_g electronic states. This is another indication of mixing between the two excited states.

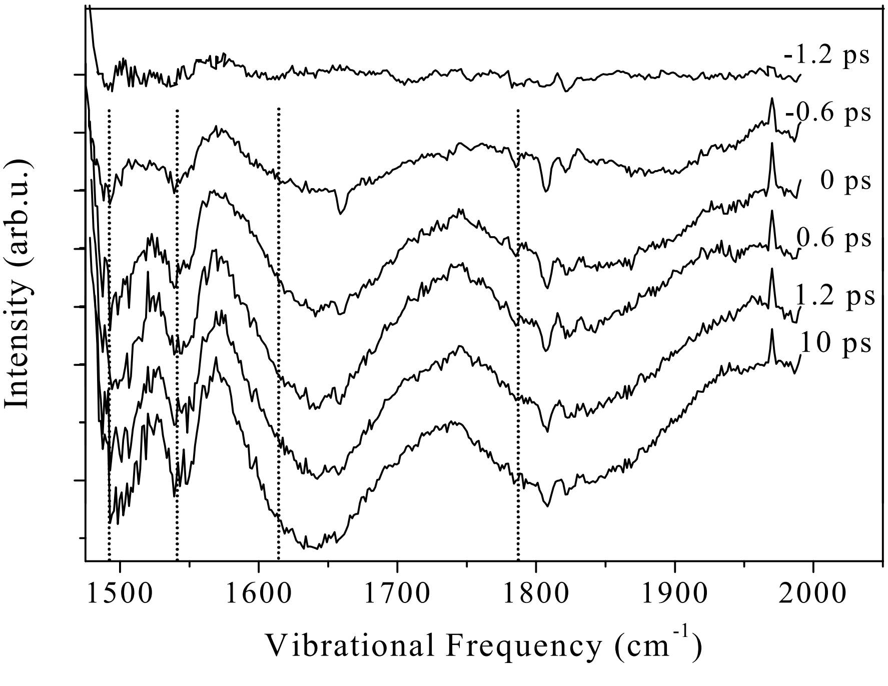

Fig.4.11: Excited-state resonance CARS spectra of DPH dissolved in cyclohexane (10^{-3} M) recorded at 726 nm to different delays after UV (363 nm) excitation.

4.4. Discussion

4.4.1. Molecular geometry and assignment of the Raman frequencies in the ground and excited states

MNDO-Configuration Interaction (CI) semi-empirical calculations done by Pfeiffer et al. [33] with the MOPAC93 package [36] indicate a plane molecular geometry in the ground state, due to π–electron delocalization. This affirmation is supported by other authors [32]. The planarity at nearly C_{2h} symmetry seems to be preserved during the transition in the first and second excited singlet states [33]. Within this symmetry, intense Raman lines are expected to occur only for modes belonging to the A_g species (see paragraph 2.1.1.3). In the spectral range of interest (850–1650 cm^{-1}), these are in-plane stretching vibrations of the C—C skeleton (ν-modes), in-plane deformations of the CH bonds (δ-modes) and modes related to the breathing vibration α-A_{1g} mode of the benzene ring (at 991 cm^{-1} in isolated benzene). The strongest Raman lines in the ground-state spectrum of DPH nearly coincide with frequencies of hexatriene, which were assigned by Langkilde et al. [34]. Analysis of the potential energy distribution (PED), derived from normal mode calculation for DPH [33], shows that most of the modes between 880 and 1607 cm^{-1} are highly localized in either the chain- or benzene subsystems. Only three modes of the A_g species between 1200 and 1350 cm^{-1} exhibit a mixture between chain- and ring-stretching modes. The benzene modes characterized by their species under D_{6h} symmetry are degenerate modes which are split according to the attachment of benzene to the polyenic chain [35]. The modes related to the hexatriene segment are named by numbering of the A_g modes for this molecule. The assignment given in the right column of Table 4.3 for the ground-state vibrations is based on the calculations done by Pfeiffer et al. [33].

Table 4.2. Comparison of Raman spectra of DPH dissolved in cyclohexane electronic ground state with transient resonance CARS spectra originating from the first excited singlet state. An assignment related to Raman spectra of hexatriene (hx) and benzene (bz) is presented.

CARS, excited state		Raman, ground state		Assignment related to Raman spectra of hexatriene (hx) [34] and benzene (bz) [35]
ν (cm^{-1})	$\lvert\gamma^R\rvert/\Gamma_R$ (au)	ν (cm^{-1})	I_{raman}/Γ_R (au)	
		880	2	bz.α_A_{1g}
970	13			
		999	11	hx.ν_{11}
1080	30			
1131	73			
1143	57	1144	31	hx.ν_{10}
		1157	22	bz.δ_E_{2g}
1160	57			
1185	60	1178	21	bz.δ_E_{2g}
1240	57			

		1253	22	hx.ν_g, ν_9
		1295	3	bz.ν_B_{2u}
1322	55			
		1331	4	bz.ν_B_{2u}
1410	45			
		1446	15	bz.ν_E_{1u}
		1496	6	bz.ν_E_{1u}
1490	100			
1542	98			
		1570	19	bz.ν_E_{2g}
		1588	77	hx.ν_6
		1595	100	hx.ν_5
		1607	38	bz.ν_E_{2g}
1620	60			
1795	17			

4.4.2. Bond order equalization in the first and second excited state

The semi-empirical calculations done by Pfeiffer et al. [33] give also information about the bond orders of the skeletal bonds, i.e., about the geometry of the molecule in both ground and excited singlet states. This subject will be discussed in the following.

In order to reproduce the correct term ordering of the 2^1A_g and 1^1B_u excited states, it is necessary to include double excitation in the CI calculation. The calculation can be confined to the two highest occupied levels of the ground state configuration, and to the two following lowest unoccupied molecular orbitals. These four molecular orbitals are practically determined by the π-electron system of the hexatriene backbone. They belong (with increasing energy) to the b_u, a_g , b_u and a_g symmetry species, respectively. Compared to the closed-shell configuration for the 1^1Ag state, the second excited singlet of 1^1B_u type is nearly perfectly a configuration with singly excited HOMO → LUMO transition. The first excited singlet of 2^1A_g type can be described as a combination of two singly excited configurations HOMO → LUMO+1, HOMO-1 → LUMO and one doubly excited closed-shell structure (HOMO, HOMO → LUMO, LUMO). Applying the PM3-Hamiltonian and the CI option OPEN (4,4) Pfeiffer et al. [33] obtained a gap between the 1^1B_u and the 2^1A_g state of about 2000 cm^{-1} (that is nearly the same as obtained from experiment [6, 7]), and a correct ordering of the two excited states.

The calculated geometry gives strong changes of bond lengths in the π-chain for the two states in comparison to the ground state condition, as shown in Fig. 4.12.

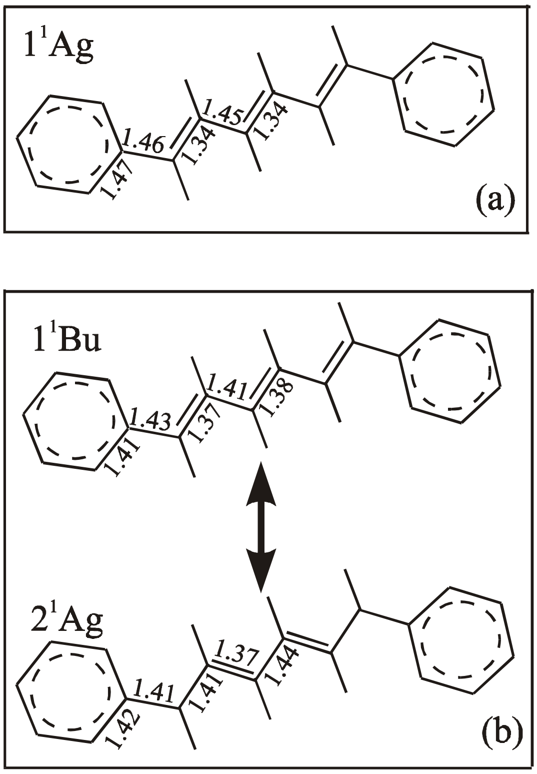

Fig.4.12: Calculated bond length of DPH along the π-chain. (a)-electronic ground state; (b) local minima of the 2^1A_g and 1^1B_u excited electronic states. The arrow between these two states indicate mixing.

The ground state geometry of DPH exhibits a pronounced alternation of C_i—C_{i+1} bond lengths between neighboring bonds in the chain, which is typical for a polyenic structure. The Bond Length Alternation (BLA) given by BLA=$2\frac{r_{i+1}-r_i}{r_{i+1}+r_i}$, with r_i the bond lengths, becomes BLA$\cong$0.08. Both excited states show decreased bond orders of double bonds. However, in contrast to the 1^1B_u state, where the bonds tend to equalize (BLA=0.02), in the 2^1A_g state two bonds are found as pronounced double bonds, but with a reversal of the former double- and single-bond positions.

According to Pfeiffer's calculations [33], one can expect upshifts of some tens of wavenumbers of the vibrational frequencies of the chain normal modes containing a high degree of single-bond C-C stretching motions (about 1150–1300 cm^{-1} in the electronic ground state), while those vibrations which are strongly localized in the phenyl rings exhibit only small shifts of some wavenumbers. In the C=C double-bond stretching region of the chain (about 1600 cm^{-1} in the electronic ground state), considerable down shifts of some tens of wavenumbers are calculated. These trends hold for the 2^1A_g and 1^1B_u states as well. Quantitatively, the calculated down shifts in the double-bond region are stronger for the 2^1A_g than for the 1^1B_u state. The exception from those "well behaving modes", which shift down if the bond order of the double bonds is decreased, is one totally symmetric double-bond stretching vibration. For this vibration, upshifts of 211 and 84 cm^{-1} were calculated for the 2^1A_g and 1^1B_u excited states, respectively [33].

4.4.3. Origin of the Raman resonances

Now it is important to discuss the origin of the excited-state CARS spectra. Under off-resonance excitation conditions and for DPH concentrations below 10^{-3} M/l, CARS lines from DPH molecules in the electronic ground state can hardly be observed. The lower concentrations of molecules in the excited states can only be detected by resonance CARS spectroscopy. This is due to the signal enhancement which is achieved by using a transient electronic resonance of the excited state. The appearance of CARS lines of the excited DPH as dips further confirm resonance enhancement due to the absorption band of the excited electronic state near 650 nm.

If the assignment of the 650 nm transient absorption as a pure 2^1A_g - n^1B_u electronic transition [25-27] were correct, then the CARS spectra should originate from the 2^1A_g state. Consequently, one upshifted frequency should be observed, due to the 1^1A_g-2^1A_g vibronic coupling. However, two CARS resonances are observed upshifted to 1620 and 1760 cm $^{-1}$ in the excited DPH molecules dissolved in cyclohexane. These frequencies nearly coincide with calculations predicting two upshifted totally symmetric C-C double-bond vibration, one for the 1^1B_u and the other one for the 2^1A_g electronic state [33].

Furthermore, vibrational resonances detected in the fluorescence excitation spectra of long-chain polyenes observed in the range of 1750–1800 cm are due to the 2^1A_g electronic state [10]. It is known that this strong upshift occurs because of 1^1A_g –2^1A_g vibronic coupling [10, 11]. The excited-state CARS spectra of DPO shows only one rather sharp vibrational resonance at 1755 cm^{-1} in that region [17], which nearly coincides with one excited-state vibration of DPH at 1780 cm^{-1}. On the other hand, the excited-state Raman spectrum of DPB has been attributed to the 1^1B_u or to a mixed electronic state [18]. In this molecule only one very broad line at 1650 cm^{-1} has been observed corresponding to a frequency at 1620 cm^{-1} calculated for the 1^1B_u state [37]. This resonance coincides with the other up-shifted vibration of the excited DPH. Thus, one can conclude that the observed vibrations in DPH belong to the 1^1B_u and to the 2^1A_g electronic states.

In the next step, it has to be distinguished between a 1^1B_u - 2^1A_g thermalized mixture [7] and an excited singlet of mixed 1^1B_u and 2^1A_g character. Assuming two separate excited electronic states after primary population of the 1^1B_u state, fast energy transfer to the 2^1A_g or to the mixed state is expected. The transfer time (500 fs [28]) is faster than our time resolution. However, the transfer from the hot but thermalized excited electronic states to the solvent cage should occur on a 10 ps time scale [38, 39]. Assuming a gap of 1000 cm^{-1} between the excited states in the cyclohexane solution, a thermal population of the 1^1B_u state at room temperature below 0.1% of that of the 2^1A_g population should result [27]. Consequently, the initially populated 1^1B_u state should dramatically drop to a value far below the detection limit for the vibration belonging to the 1^1B_u state after about 10 ps (which is a usual thermalization time in liquids). In contrast, the time-resolved vibrational spectra show that the relative strength of the vibrational resonances attributed to the A_g and B_u electronic states are independent on the delay and that only one excited state is populated. The growth in the population of this electronic state is finished at least after 1–2 ps, which is in accordance with the result of Atom Yee [28]. Furthermore, in changing the solvent and hence the gap between the 2^1A_g and 1^1B_u electronic states, a strong alteration of the relative strength of vibrations belonging to different electronic states has to be expected, according to a changed Boltzmann equilibrium. In contrast, the main effect is the frequency decrease of the two broad Raman resonances with increasing solvent polarizability (Fig. 4.9). Because the gap

2^1A_g - 1^1B_u narrows with increasing polarizability of the solvent, the dependence in Fig. 4.9 gives evidence of a mixed 2^1A_g - 1^1B_u excited state.
This will be discussed in the following paragraph.

4.4.4. Mechanisms of vibronic coupling

In his book about vibronic coupling mechanisms [40], Bersuker has shown that the adiabatic approximation can be applied only if $\hbar\omega << |\varepsilon_m' - \varepsilon_k'|$, where the term on the left side is the energy quantum of vibrations in the electronic state under consideration (k or m) and ε_m' and ε_k' represents the electronic energy levels m or k. Because the gap between the first and second excited state of DPH is about 1000 cm^{-1}, it is obvious that the adiabatic approximation cannot be applied and vibronic coupling effects have to be considered.
For a discussion of the vibronic coupling mechanism, the major experimental findings are reviewed here. First, **two** unusually upshifted bands have been observed in DPH with frequencies higher then 1600 cm^{-1}. The second interesting aspect is the decrease of their frequency with increasing solvent polarizability, i.e., with decreasing the 2^1A_g - 1^1B_u gap. If the molecule keeps a planar configuration, and the C_{2h} symmetry is maintained in the excited state, coupling between the 2^1A_g and 1^1B_u states by the a_g mode is symmetry forbidden, as discussed in paragraph 2.1.1.3. In the following, two mechanisms of vibronic coupling will be discussed, which are able to explain the appearance of the two upshifted vibrational frequencies, as well as their solvent dependence. These are: **(i)** distorsion of symmetry by two rotamers and **(**ii**)** vibronic coupling by a b_u-type vibrational mode influencing the potential of the high-frequency a_g mode.

4.4.4.1. (i) Coexistence of two species in the 2^1A_g state

In the following, the possibility of molecular symmetry distortion and its influence on vibrational spectra will be discussed. In this model, the two vibrational frequencies of the same vibrational mode originate from two different species (for example two rotamers) in the 2^1A_g state, both deviating from C_{2h} symmetry (due to the twisting of the backbone). In this case, vibronic coupling by an a_g mode is not strictly forbidden [16] and conformational dependent coupling constants of the two rotamers can generate two frequencies belonging to the same C=C stretching motion. Because of the very small gap, even with rather small coupling constants, vibronic coupling can be quite effective. Both vibrational frequencies are expected to shift down with decreasing gap between the two excited electronic states, as they belong to the lower of the two excited singlet states, i.e., to the 2^1A_g state. Frequency broadening can be caused by conformational distributions around the two equilibrium geometries. Other vibrational modes which do not couple the two excited electronic states are not expected either to be shifted in solvents of different polarizabilities, nor unusually frequency broadened due to conformational distributions.
However, according to the electronic structure calculations (MOPAC93 [36]) presented in the paragraph 4.4.2, and because of the pronounced π-electron delocalization, DPH is planar in the electronic ground, as well in both excited electronic states, maintaining C_{2h} symmetry. Furthermore, the existence of two different species seems to be unlikely

because the observed kinetics (rise of the CARS lines originating from S_1 and fluorescence decay [1]) give no hints for two separate species in the excited state.

4.4.4.2. (ii) Model of vibronic coupling with an asymmetric low-frequency mode

In the following, a model of vibronic coupling will be presented, which is based on the pseudo Jahn-Teller effect. This model was developed by Pfeiffer et al. [33]. It can reproduce the potentials of the high frequency a_g mode, resulting in two upshifted frequencies.

4.4.4.2.1. Determination of the modes responsible for vibronic coupling

Symmetry considerations require that vibronic coupling between the 2^1A_g and 1^1B_u states is mediated by vibrational modes of b_u type only. For the 1^1A_g –2^1A_g coupling, only a_g -type modes are admitted, and it can be expected that the modes with the largest origin shift, i.e., with the strongest Raman activity will contribute substantially. The equilibrium geometries of the 2^1A_g and 1^1B_u states differ markedly from that of the ground state. By decomposing the nuclear displacements in normal coordinates the dominantly contributing modes can be identified. Atomic positions are calculated optimizing the geometry for the respective electronic state on the quantum chemical level characterized in section 4.4.1. By taking the normal coordinates calculated for the ground state, the relative intensities of the excited states in-plane modes are given in Fig. 4.13. The modes are numbered by increasing wavenumbers. For both final geometries, Fig. 4.13 shows that in the low frequency region there is a dominating contribution from just one low-frequency b_u mode calculated at 40 cm^{-1} in the ground state. The same normal mode appears in both excited states with slightly shifted frequency at 42 cm^{-1} in the $1B_u$ and 49 cm^{-1} in the $2A_g$ state. In the high frequency region there is one dominant contribution from the high-frequency totally symmetric C=C a_g stretching mode. The corresponding normal coordinate represents a vibration with antiphased elongation in all neighboring C-C bonds of the polyenic chain. This mode is known to give the largest origin shift value along the π-chain and generally results in the strongest bands in the resonance Raman spectra of the polyenes. Both low- and high-frequency modes are marked with arrows, and their geometry is shown in the upper part of Fig. 4.13. The b_u mode is the zero-node string mode of the polyenic chain. The applied semiempirical calculation of vibrational frequencies reproduces the experimental frequencies in the low-frequency range with an accuracy better than 10%. Therefore, the broad intense band observed at 35 cm^{-1} in the ground state spectrum (Fig. 4.5) is proposed as the candidate for the b_u coupling mode.

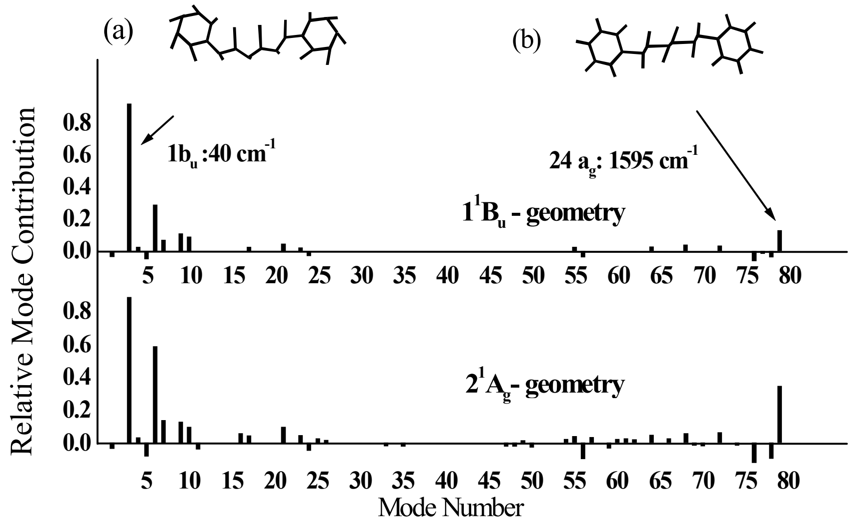

Fig. 4.13: Decomposition of geometrical displacements in the two lowest excited singlet states according to normal coordinates of in-plane modes. Modes number 3 and 78 are those taken as involved in the vibronic coupling.

4.4.4.2.2. Pseudo-Jahn-Teller effect in the excited states of DPH

Based on the calculations presented in the preceding paragraph, a 3-state model has been chosen to describe vibronic coupling in the case of DPH, with two active coupling modes (normal coordinates Q_1 for the a mode at 1595 cm^{-1} , Q_2 for the b$_u$ mode at 40 cm^{-1}). It is the generalization of the two-state, one-mode model of coupling between 1^1A_g and 2^1A_g states, which was developed to reproduce the upshift of the 1600cm^{-1} mode in the excited state relative to its ground state frequency [11]. Within the three-state model, the effective two-dimensional potential energy surface $E(Q_1, Q_2)$ has been estimated by diagonalization of the diabatic Hamiltonian

$$H_{diab} = \begin{pmatrix} H_0 & \alpha_{01}Q_1 & 0 \\ (\alpha_{01}Q_1)^* & H_1 & \alpha_{12}Q_2 \\ 0 & (\alpha_{12}Q_2)^* & H_2 \end{pmatrix}$$

(4.1)

The indices denote the electronic singlet states involved (index 0 for the 1^1A_g ground state, 1 and 2 for the excited 2^1A_g and 1^1B_u states, respectively). The vibronic coupling constant α_{01} is set equal to the value derived by Orlandi and Zerbetto for hexatriene [41] ($|\alpha_{01}|$=1.65 eV A^{-1} amu $^{-1/2}$). The estimates within the Pariser-Parr-Pople (PPP) method give for α_{12} a value approximately one order of magnitude lower than that, and it is set to 0.2 eV A^{-1} amu$^{-1/2}$. Within this approximation, there is no vibronic coupling between the 1^1A_g –1^1B_u states through the b$_u$ mode. The harmonic approximation is chosen for the diabatic potentials. Thus, the potentials in the two (uncoupled) excited singlet states can be written as:

$$V_{2Ag}(Q_1,Q_2) = \frac{1}{2}\left[\omega_{1\_2Ag}^2(Q_1 - Q_{1\_2Ag})^2 + \omega_2^2 Q_2^2\right] \qquad (4.2)$$

$$V_{1Bu}(Q_1,Q_2) = \frac{1}{2}\left[\omega_{1\_1Bu}^2(Q_1 - Q_{1\_1Bu})^2 + \omega_2^2 Q_2^2\right] + \Delta_{12} \qquad (4.3)$$

where Q_1 and Q_2 are the elongations of the a$_g$ mode and of the b$_u$ mode, respectively, Q_{1_2Ag} and Q_{1_1Bu} are the positions of the diabatic minima of the corresponding potentials (mass normalized origin shifts), and Δ_{12} is the gap between the two minima. Vibronic coupling between the states is performed by a linear coupling ansatz $V_{2Ag,1Bu} = \alpha_{12} Q_2$.

Coupling results in the two dimensional potential.

$$V(Q_1, Q_2) = \frac{V_{2Ag} + V_{1Bu}}{2} \pm \sqrt{\left(\frac{V_{2Ag} - V_{1Bu}}{2}\right)^2 + (\alpha_{12} Q_2)^2} \tag{4.4}$$

Under these conditions a double well potential along the Q_1 coordinate in the first excited singlet state is generated by a pseudo-Jahn-Teller mechanism. It arises from coupling of both potentials (Eqs. 4.2 and 4.3) in assuming a sufficiently large shift between the minima $d = (Q_{1\_2Ag} - Q_{1\_1Bu}) / \sqrt{m_1^{eff}}$. For an estimated value of $d = 0.18$ Å, two minima arise in the potential of the lowest excited singlet state.

In Fig. 4.14.a and 4.14.b is shown the double minimum potential of the two vibronically coupled states for the totally symmetric C=C stretching mode. As a result, the same vibrational mode give rise to two vibrational frequencies, one in the potential minimum of the 2^1A_g excited state, and the other one in the potential minimum of the 1^1B_u excited

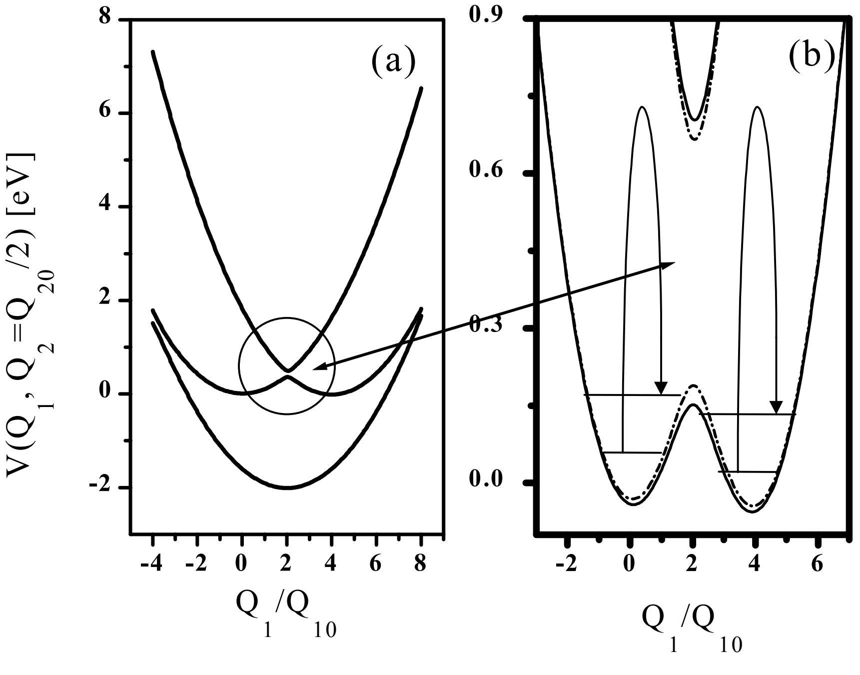

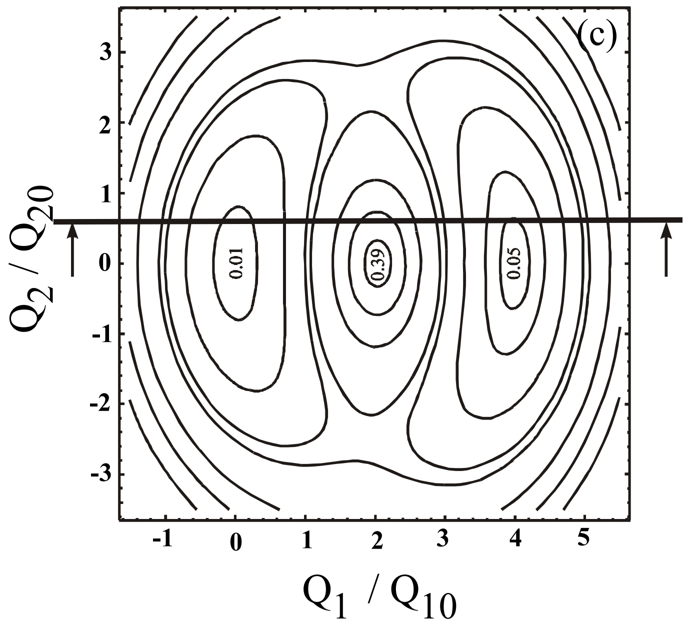

Fig. 4.14: (a) Effective potential for the totally symmetric C=C stretching coordinate around 1700 cm^{-1} in the two vibronically coupled states. In the 2^1A_g state the pseudo-Jahn-Teller effect leads to a double-well potential; (b) Enlarged segment of the range of avoided level crossing between the 1^1B_u and 2^1A_g singlet states. The dashed line represents the potential curve for a smaller gap. Horizontal lines indicate the energy positions for the lowest vibrational levels in the respective diabatic potentials (left 1^1B_u - section, right 2^1A_g - section). The assumed Raman transitions are indicated; (c) Contour diagram of the effective 2-d vibrational potential for the first excited singlet state of DPH resulting from strong vibronic coupling (the cut at $Q_2= Q_{20}/2$ represents the lower potential in (b).

state. From the curvature of these minima, the two frequencies of the quasi bound vibrational levels around the Q_{1_2Ag} and Q_{1_1Bu} minima have been determined. Fig. 4.14.c shows also a contour diagram of the effective 2-d vibrational potential for the excited singlet states of DPH resulting from strong vibronic coupling.

The observed dependence of vibrational frequencies on the solvent polarizability can be explained by the following considerations. In transparent solvents, the effective vibronic coupling between the excited states in the first approximation varies with the Lorenz-Lorentz molar refraction according to the relation:

$$\frac{\alpha_{12}^2}{\Delta_{12}} = \left[\frac{\alpha_{12}^2}{\Delta_{12}}\right]_{vacuum} (1+\beta\frac{n^2-1}{n^2+2}) \qquad (4.5)$$

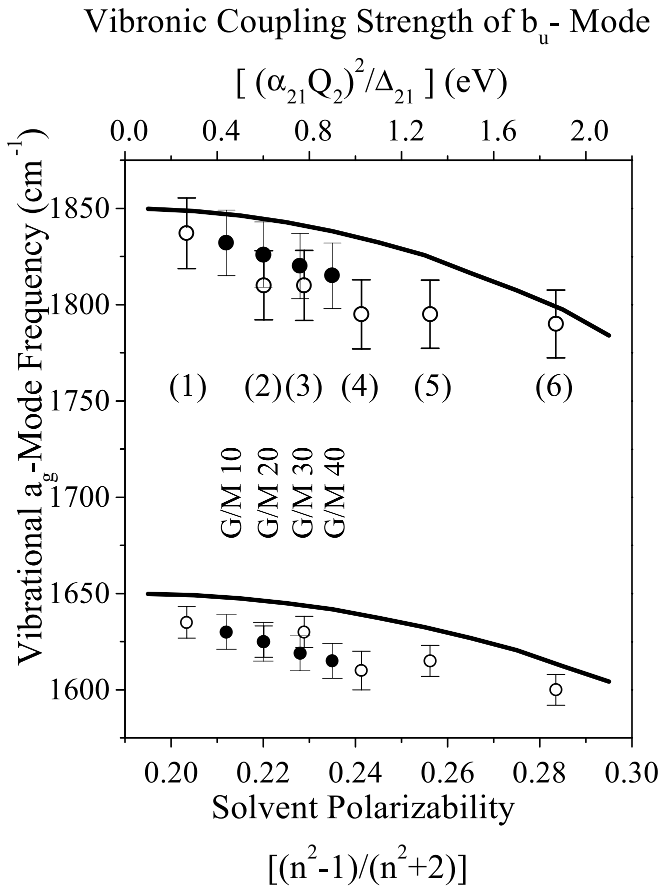

Fig.4.15: Dependences of the two high-frequency vibrations above 1600 cm^{-1} of the excited electronic state of DPH on the polarizability of neat solvents (|) and of mixture of glycerol and methanol (ʃ). The solvents used are: (1) methanol, (2) acetone, (3) hexane, (4) octane, (5) cyclohexane, (6) dimethylsulfoxide, G/M 10=10 vol% glycerol in methanol, G/M 20=20 vol% glycerol in methanol, etc. Straight lines represent calculated frequency dependences on the vibronic coupling strength of the bu-mode between the excited electronic states.

The equation is derived applying Hudson's rule [20] for the dependence of the effective coupling element $\alpha_{12} / \Delta_{12}$ on the solvent refractive indices n. Here, β is a positively valued parameter related to the transition dipole and polarizability properties of the solute molecule. Applying Eq. (4.5) in combination with Eq. (4.4), the observed frequency shifts versus solvent polarizability are reproduced qualitatively, as shown in Fig. 4.15. The two minima arise from the originally diabatic potentials of the 2^1A_g and of the 1^1B_u potentials. This also explains the close correspondence of the two vibrational frequencies measured in DPH either to the excited state frequency observed in DPO at 1755cm^{-1} (assigned to the 2^1A_g state [17]) or to the band in DPB at 1620cm^{-1} measured after electronic excitation which has been assigned to the 1^1B_u or to a mixed $1^1B_u/2^1A_g$ state [18]. This double minimum appears in the case of DPH through vibronic coupling by the b_u mode under the condition of nearly zero gap between the two lowest excited singlet states. Based on this model, the anomalous character of the two bands in the C=C stretching range with respect to solvent shift and high spectral broadening were inter-preted as a pseudo Jahn–Teller-like vibronic coupling in the excited state of DPH [33].

4.4.4.2.3. Frequency broadening by vibrational coupling under the condition of the pseudo-Jahn-Teller effect

Within the proposed model, there is a simple explanation for the broadening of the two high-frequency stretching bands. It results from the excited state dynamics proceeding predominantly within the two-dimensional subspace of molecular vibrational coordinates, as given by the contour-diagram in Fig. 4.14.c. Fig. 4.14.a and 4.14.b give the cut through the potential at $Q_2=Q_{20}/2$ with a double well along the Q_1 coordinate. Vibronic coupling of the 2^1A_g and 1^1B_u states by the low-frequency b_u mode, according to the coupling scheme of Eq. 4.1, results in an anharmonic coupling between the Q_1 and the Q_2 coordinates. The periodic variation of the Q_1 potential during the oscillation in the Q_2 mode modifies the Q_1 curvature and leads to a broadening of the bands for the high-frequency oscillation. The lowering of the saddle point at maximum elongation of the Q_2 mode may lead to a cross over of the primarily excited wavepacket from one valley of the Q_1 potential to the other, and thus, periodically varying the probability of finding the molecule at each region of the potential.

The modulation of the Q_1 potential with the cycle of the low-frequency oscillation yields a Fourier transform representing a spectral broadening $\Delta\omega_{\square} \approx \omega_2$. □□As spectral broadening and solvent effects for vibrational modes are absent for all other modes, one can assume that the essential coupling in the excited state could be confined to the two coordinates Q_1 and Q_2 . The other modes shall be described by independent normal coordinates.

4.5. Conclusions

In conclusion, two up-shifted and extremely broad Raman resonances have been observed in the excited state of DPH, with frequencies higher than 1600 cm^{-1}. The measured frequencies in different solvents show a clear dependence on solvent polarizability, but no dependence on viscosity or polarity of the solvent. These effects are not observed in related diphenylpolyenes, like DPO or diphenylbutadiene.

Moreover, it has been shown that there is no difference in the kinetics of the observed modes.

The two broad Raman resonances are assigned to the totally symmetric C=C stretching vibration, based on semiempirical calculations and similarity of the frequencies with the frequency of this mode in related polyenes (DPO and diphenylbutadiene). The same considerations suggest that the up-shift of the frequencies is due to S_0-S_1 vibronic coupling.

From the observed polarizability dependence of the frequencies of the C=C stretching mode, which is essentially a dependence on the gap between the S_1 and S_2 excited singlet states, and from the kinetics measurements, one gets evidence of S_1-S_2 vibronic coupling.

These findings are rather unusual, as it is believed that, because of symmetry reasons, such effects should not occur. Two explanations for the experimental findings are presented:

1. Simultaneous existence of two rotamers in the first excited singlet state. In this case, small distorsions of the symmetry are reflected in the vibrational spectra, due to their influence on the vibronic coupling effects, which are further influencing the vibrational spectra.
2. Distorsion of the potential of the totally symmetric C=C mode by a low frequency b_u mode. According to this model, coupling of the two excited singlet states by a low frequency asymmetric mode generates a double minimum for the C=C stretching coordinate in the lowest excited singlet state. Consequently, the two frequencies originate from this mode. Furthermore, anharmonic coupling between the two modes (high- and low-frequency) leads to strong frequency broadening of the C=C stretching bands.

Because these effects appear under the condition of nearly degenerate excited singlet states, this explanation was identified with a pseudo-Jahn-Teller model.

Under the viewpoint that vibronic coupling is believed to control the S_2-S_1 relaxation, our investigations should contribute to an understanding of the S_2-S_1 dynamics occurring on a fs time-scale.

References

[1] T. Parasassi, G. De Stasio, R.M. Rusch, E. Gratton; *Biophys. J.* **59** (1991)

[2] V.F. Kamalov, N.I. Koroteev, B.N. Toleutaev, A.P. Shkurinov, U. Stamm, *J. Phys Chem.* **93** (1989) 5645.

[3] D.C. Rodenberger, J.R. Heflin, A.F. Garito, *Nature* **359 (**1992) 309

[4] J. Oberle, G. Jonusauskas, E. Abraham, C. Rulliere, *Opt. Commun.* **124** (1996) 616

[5] B.S. Hudson, B.E. Kohler, *Annu. Rev. Phys. Chem.* **25** (1974) 437

[6] B.S. Hudson, B.E. Kohler, K. Schulten, in: „Excited States“, Ed. E.C. Lim, Vol. 6 Academic Press, New York (1982) 1

[7] T. Ithoh, B.E. Kohler, *J. Phys. Chem.* **91** (1987) 1760

[8] H.L.B. Fang, R.J. Thrash, G.E. Leroi, *Chem. Phys. Lett.* **57** (1978) 59

[9] B.S. Hudson, B.E. Kohler, *J. Chem. Phys.* **59** (1973) 4984

[10] R.A. Auerbach, R.L. Christensen, M.F. Granville, B.E. Kohler; *J. Chem. Phys.* **74** (1981) 4

[11] G. Orlandi, F. Zerbetto, M.Z. Zgierski; *Chem. Rev.* **91** (1991) 867

[12] H. Nagae, M. Kuki, J.-P. Zhang, T. Sashima, Y. Mukai, Y. Koyama; Proc. IX. Int. Conf. Time-Resolved Vibrational Spectroscopy May 16-21 (1999)

[13] A.P. Shreve, T.K. Trautmann, H.A. Frank, T.G. Owens; A.C. Albrecht; *Biochim. Biophys. Acta* **1058** (1991) 280

[14] A.N. Maxpherson, T. Gillbro; *J. Phys. Chem. A* **102** (1998) 5049

[15] J.F. Pfanstiel, B.B. Champagne, W.A. Majewski, D.F. Plusquellic, D.W. Pratt; *Science* **245** (1989) 737

[16] T. Noguchi, H. Hayashi, M. Tasumi, G.H.J. Atkinson; *J. Phys. Chem.* **95** (1991) 3167

[17] A. Kasama, M. Taya, T. Kamisuki, Y. Adachi, S. Maeda; in: J. Atkinson (Ed), *Time Resolved Vibrational Spectroscopy*, Gordon and Breach, New York (1987) 304

[18] D.L. Morris. T.L. Gustafson; *Appl. Phys. B* **59** (1994) 389

[19] S.M. Bachilo, C.W. Spangler, T. Gillbro, *Chem. Phys. Lett.* **283** (1998) 235

[20] J.R. Andrews, B.S. Hudson; *J. Chem. Phys.* **68** (1978) 4587

[21] K. Lunde, L. Zechmeister, *J. Am. Chem. Soc.* **76** (1954) 2308.

[22] J. Saltiel, D.H. Ko, A. Fleming, *J. Am. Chem. Soc.* **116** (1994) 4099.

[23] J. Saltiel, D.F. Sears Jr., Y.P. Sun, J.O. Choi, *J. Am. Chem. Soc.* **114** (1991) 3607

[24] Th.C. Felder, K.J. Choi, M.R. Topp, *Chem. Phys*. **64** (1982) 175

[25] R.A. Goldbeck, A.J. Twarowski, E.L. Russel, J.K. Rice, R.R. Birge, E. Switkes, D.S. Kliger, *J. Chem. Phys*. **77** (1982) 3319.

[26] C. Rulliere, A. Declemy, *Chem. Phys. Lett*. **135** (1987) 213

[27] E.F. Hilinski, W.M. McGowan, D.F. Sears Jr., J. Saltiel, *J. Phys. Chem*. **100** (1996) 3308

[28] W. Atom Yee, R.H. O'Neil, J.W. Lewis, J.Z. Zhang, D.S. Kliger; *Chem. Phys. Lett*. **276** (1997) 430

[29] H.L.B. Fang, R.L. Trash, G.E. Laroi; *Chem. Phys. Lett*. **57** (1978) 59

[30] M. Pfeiffer, A. Lau, W. Werncke; *J. Raman Spectrosc*. **17** (1986) 425

[31] B. Schrader, in „*Raman/Infrared Atlas of Organic Compounds*“; VCH Verlagsgesellschaft, Weinheim, VCH Publishers, New York (1989) E1-01

[32] J.N. Murrell, in *„The Theory of the Electronic Spectra of Organic Molecules“* Spottisworch, Ballantyne and Co. Ltd., London (1963)

[33] M. Pfeiffer, W. Werncke, S. Hogiu, A. Kummrow, A. Lau; *Chem. Phys. Lett*. **295** (1998) 56

[34] F.W. Langkilde, R. Wilbrandt, O.F. Nielsen, D.H. Christensen, M. Nicolaisen, *Spectrochim. Acta A* **43** (1987) 1209

[35] G. Herzberg, in „*Molecular Spectra and Molecular Structures*“,Vol. II, Infrared and Raman Spectra of Polyatomic Molecules, Lancaster Press USA (1945)

[36] MOPAC 93 Fujitsu Ltd., Tokyo, Japan (1993)

[37] B. M. Pierce, R. R. Birge, *J. Chem. Phys*. **86** (1982) 2651

[38] T. Elsaesser, W. Kaiser, *Annu. Rev. Phys. Chem*. **42** (1991) 83

[39] J. Qian, S.L. Schultz, G.R. Bradburn, J.M. Jean, *J. Luminesc*. **60/61** (1994) 727

[40] I. B. Bersuker, in *„The Jahn-Teller effect and vibronic interactions in modern chemistry“*, Plenum Press, New York (1984).

[41] G. Orlandi, F. Zerbetto, *Chem. Phys*. **108** (1986) 187

5. Mode specific vibrational kinetics after intramolecular electron transfer in Betaine-30

5.1. Motivation

Betaine-30 (B-30) is a molecule undergoing ultrafast intramolecular electron transfer in condensed phase [1, 2]. In the electronic ground state, B-30 has a high dipole moment which is substantially reduced upon electronic excitation to the first excited singlet state. The absorption to this state exhibits a charge transfer character. Relaxation of the first excited singlet state involves back-electron transfer (back-ET) restoring the charge distribution of the ground state.

According to time-resolved absorption measurements of Barbara and co-workers [2-5], the back-ET times of B-30 vary from 0.6 ps up to about 100 ps depending on the temperature and the solvent. It has been observed that in rapidly relaxing solvents -like acetonitrile, propylene carbonate (PC) etc.- the back-ET time $\tau_{\text{back-ET}}$ is close to the solvation times τ_s. These conditions are rationalized as „solvent controlled regime“, where solvent reorientation during the excited state lifetime of the solute strongly accelerates back-ET by lowering the excited state potential energy surface (see also paragraph 2.2.3). In solvents with slower τ_s (e.g. glycerol triacetine (GTA), alcohols etc.) the back-ET transfer time is shorter than the solvent response, and hence back-ET occurs under the condition of a „frozen“ solvent shell.

According to classical Marcus theory of ET [6], the fastest rates of back-ET are expected near the turning point between the „inverted“ and „normal“ regime, where the free energy of activation of the reaction approaches zero. For B-30, it has been shown that the back-ET occurs in the inverted regime [1, 2], i.e., the ΔG^0 energy gap between the excited and ground state is larger than the solvent reorganization energy λ (see Fig. 2.3). For a theoretical description of ET rates, the model of Marcus and Sumi [7] has been used, where the action of a low frequency mode together with a classical solvent degree of freedom is considered (see paragraph 2.3.5). For B-30, however, this model predicts much lower back-ET rates than observed experimentally [4]. Jortner and Bixon have shown that additional intramolecular high frequency modes, which are treated quantum-mechanically, have to be taken into account for calculating these rates more accurately [8,9]. The back-ET rate is then given as a sum of rates from all occupied levels of the reactant state to all vibrational levels of the product state [9] (see also Fig. 1.2). Combining these two approaches in a hybrid model, Barbara et al. were able to reproduce the back-ET kinetics in a wide range of different environments [4].

Nonequilibrium vibrational excitations should occur for intramolecular vibrational modes which are involved in back-ET, i.e., are part of the reaction coordinate. For back-ET times faster or at least comparable to the time scale of intramolecular redistribution of vibrational energy (IVR), one expects pronounced excess populations of these modes via back-ET. The excess populations decay by IVR and by simultaneous or subsequent flow of energy to the surrounding solvent (i.e. vibrational cooling). B-30 represents an interesting model system for such studies as the ET time varies substantially with the solvent. As a result, vibrational dynamics can be studied both for solvent controlled ET, as well as for ET controlled by intramolecular couplings.

It has to be noted that IVR includes (i) intra-mode energy transfer along the ladder of excited levels in a certain mode as well as (ii) inter-mode vibrational energy transfer (see also paragraph 5.2). Early picosecond pump-probe absorption spectroscopy suggested that IVR in large molecules is completed on a subpicosecond time scale [10]. Subsequent vibrational cooling of the vibrational-thermalized solute molecule to the solvent proceeds within some tens of picoseconds. In contrast, more recent absorption measurements with improved time resolution and sensitivity indicated non-thermal distributions up to several picoseconds [11,12]. However, this type of experiment does not allow to gain information about the selective population of vibrational modes, because of the usually broad and structureless absorption bands of large molecules in solution.

Time-resolved vibrational spectroscopy represents a technique directly addressing the dynamics of nonequilibrium vibrational populations. Nonlinear changes of vibrational absorption on the v=0 to v=1 transition and/or on the anharmonically shifted v=1 to v=2 transition give insight into the mode specific population dynamics. Using this technique, intra-mode vibrational relaxation of the $C\equiv O$ stretching vibration after back-ET in the $[Co(Cp)_2^+/Co(CO)_4^-]$ ion pair has been observed [13]. In a different approach, vibrational populations of Raman active modes are monitored by anti-Stokes Raman spectroscopy [14-18]. Here, the anti-Stokes Raman signals originate exclusively from excited vibrational levels, in most cases from the population of the v=1 level.

So far, there are very limited information on the vibrational dynamics of B-30. Resonance Raman spectroscopy provides insight into the dynamics of modes which are strongly involved in the intramolecular vibronic coupling, i.e., the group of modes which is expected to contribute predominantly to back-ET.

In this thesis, a detailed study of vibrational dynamics during and after back-ET in B-30 is presented, both for the „solvent controlled regime“ as well as under conditions of a „frozen“ solvent. Modes with strong origin shifts of the excited state potential are identified by resonance Raman spectra in the charge transfer absorption band. From time-resolved anti-Stokes Raman spectra vibrational excess populations have been determined and - as soon as thermal equilibrium between Raman active modes has been established - vibrational temperatures. The results indicate selective excitation of Raman active modes within the first few picoseconds. Differences in the excitation behavior of several modes are clearly pronounced for fast relaxing solvents. Thermal equilibrium between the Raman-active modes is established within 10 to 15 ps after back-ET. It results in higher vibrational temperatures in slowly relaxing compared to fast relaxing solvents.

5.2. Absorption spectra and photophysics of the molecule

The molecular structure of B-30 in the electronic ground state is presented in Fig. 5.1. The different dipole moments of the molecule in polar and nonpolar solvents, and the changes of the dipole moments after absorbing of one photon with hν energy, are shown schematically. The back-ET is marked by b-ET. The charge transfer reaction of B-30 as illustrated in Fig. 5.1 is „direct", i.e., excitation within the CT band is directly accompanied by the transition from a strongly charge separated ground state to a more neutral first excited singlet (Franck-Condon) state. Dipole moments in the electronic ground state and in the S_1 state of 16 D and 6 D, respectively, have been determined experimentally [19].

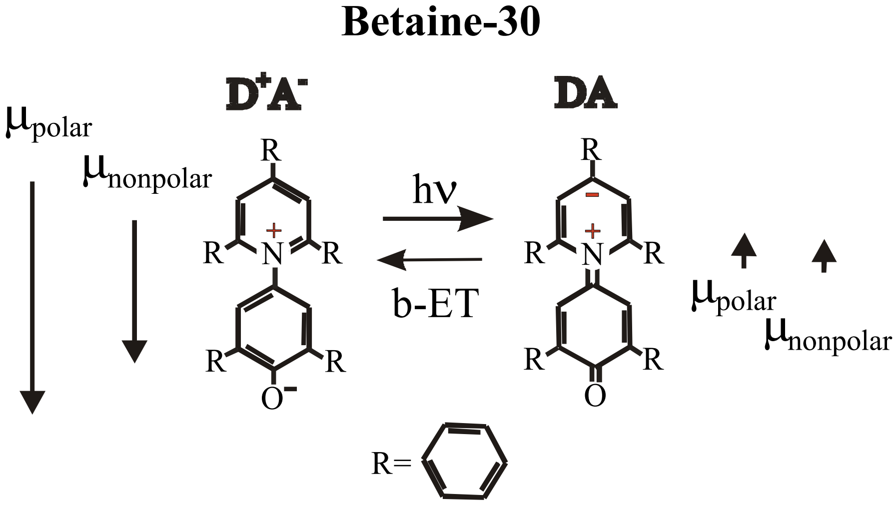

Fig.5.1: Molecular structure of B-30

Absorption spectra of B-30 in different solvents (in GTA, PC and Ethanol (ETH)) are plotted in Fig. 5.2.

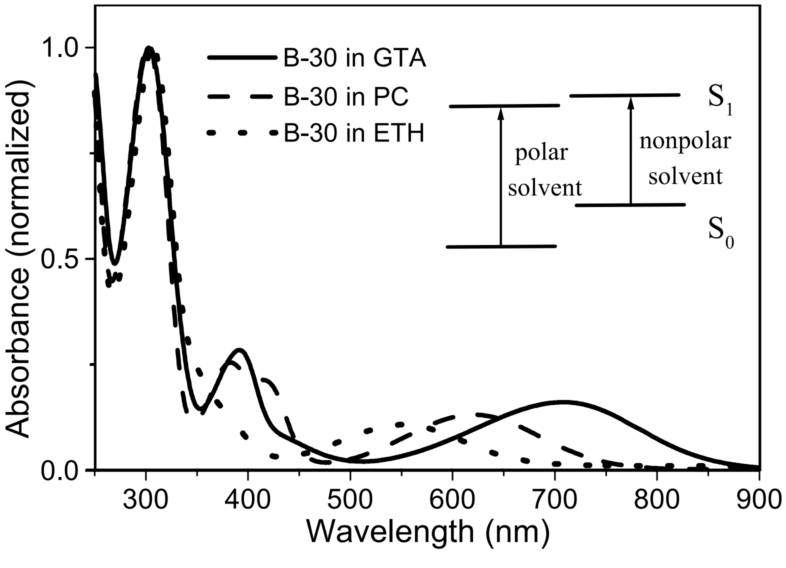

Fig. 5.2: Absorption spectra of Betaine-30 in Glycerol triacetate (GTA), Propylene Carbonate (PC) and Ethanol (ETH). In the insert is marked the change in the position of the potential surfaces of the ground state (S_0) and first excited singlet state (S_1).

The position of the broad band between 500 nm and 700 nm is solvent dependent, indicating the strong charge transfer character of the lowest electronic transition (CT band). This behavior has been used to define the empirical E_T^{30} polarity scale [20]. The position of the strong band around 300 nm is not solvent dependent and is assigned to a transition to a locally excited (LE) electronic state. In the insert, the change in the position of the potential surfaces of the ground and first excited singlet state is shown. Because the dipole moment in the ground state is about three times the dipole moment in the excited state, the potential surface of the ground state is more sensitive to the changes of the environment polarity.

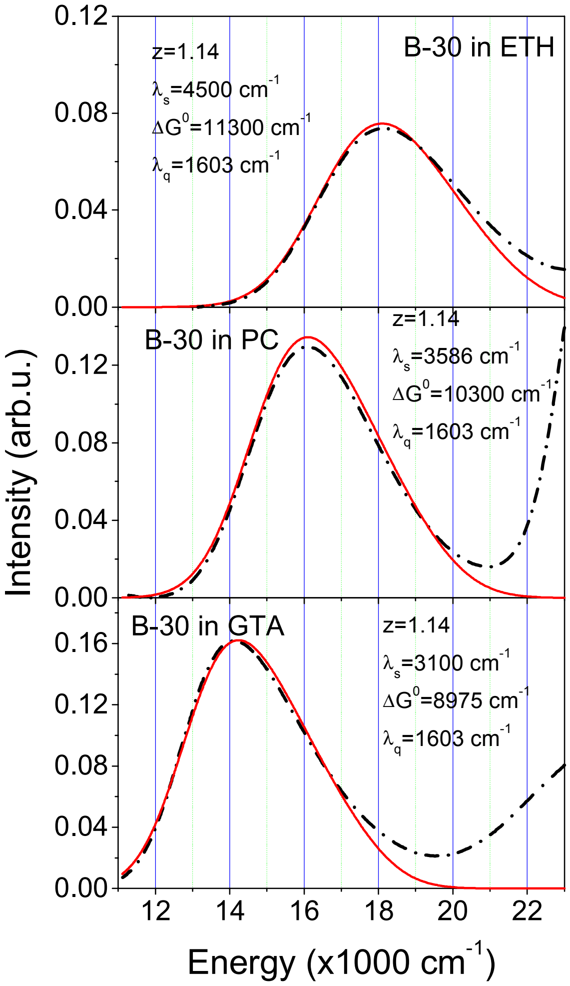

Fig. 5.3: Fit of the CT absorption band of B-30 dissolved in ETH, PC and GTA. Dot line: experimental curve; solid line: fit with Eq. 5.1. The parameters obtained from the fit are seen in the inserts.

The static CT absorption band has been fitted to a line shape model by using the same formalism described in paragraph 2.3.5, which includes one classical (λ_s) and one high-frequency (λ_q) degree of freedom. The form of the absorption line shape is therefore a sum of Gaussians in a Franck-Condon distribution, as follows:

$$I(\nu)=\sum_k \frac{e^{-S}S^k}{k!}\exp\left[-\frac{(\nu-(\lambda_s-\Delta G^o+k\lambda_q))^2}{4\lambda_s k_B T}\right] \tag{5.1}$$

where $S = z^2/2$ is related to the origin shift parameter z, k is positive and integer and represents the vibronic quantum number, λ_s is the total classical reorganization energy, ΔG^o the free energy of reaction, and λ_q is the frequency of the quantum vibrational mode, which was chosen as 1603 cm^{-1}, i.e., equal to the highest frequency mode observed in the Raman spectrum. The parameters obtained from the fit of the CT absorption band of B-30 dissolved in ETH, PC and GTA are given in the inserts of the Fig. 5.3. Obviously, the asymmetry of the absorption band is due to the Franck-Condon progression. The high-frequency region in Fig. 5.3 is dominated by the absorption to a higher electronic state.

In Fig. 5.4. the photophysical processes occurring in B-30 after photoexcitation are shown schematically.

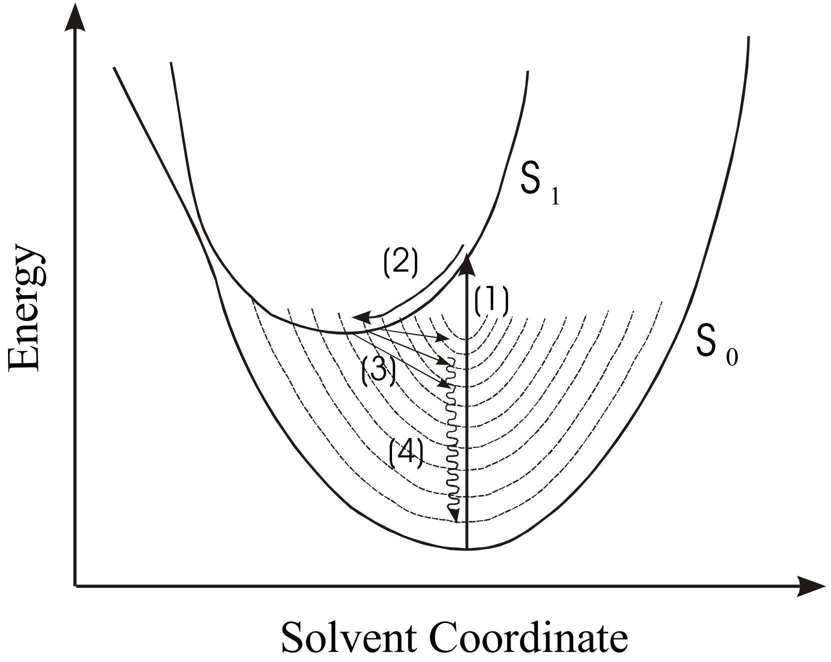

Fig. 5.4: Photophysics of B-30: (1) direct excitation in the CT band, (2) reorganization in the excited state, (3) back-ET and (4) vibrational relaxation.

The very fast excitation in the CT band (step 1) is followed by solvation in the excited singlet state (step 2). The time duration τ_S of this process is solvent specific and depends strongly on the temperature. At room temperature, τ_S lies between 0.5 ps for acetonitrile to few hundred of ps for GTA. If τ_S is fast (0.5 ps to 3 ps), the reorganization in the excited singlet state strongly accelerates the back-ET by lowering the excited state potential energy surface. In this case $\tau_s \approx \tau_{b-ET}$ (where τ_{b-ET} is the duration of the back-ET in the step 3), and the terminology „solvent controlled regime“ is usually used. For slowly relaxing solvents (τ_S>3 ps) a smaller amount of energy is expected to be transferred to the solvent, and the terminology used in this case is „vibrational controlled regime“.

During back-ET, it is assumed that the excess energy is deposited into highly excited vibrational modes of the electronic ground state. Step 4 represents schematically the intra- and inter-mode (not shown in the Fig. 5.4) vibrational relaxation in the electronic ground state (IVR).

5.3. Stationary vibrational spectra and ab initio calculations of geometry and vibrational spectra.

Before going to deal with the Raman pump-probe experiment, information concerning molecular structure of B-30 will be gained by a combined study of the stationary Raman and infrared spectra with ab initio calculations.

In particular, the influence of the solvents and excitation wavelengths on the Stokes-Raman spectra will be presented. In addition, the calculated vibrational frequencies in the electronic ground state allow an assignment most of the observed vibrations. The reasonable agreement between calculated and observed vibrational spectra indicate that the optimized molecular structures used in this calculations are close to reality. From the calculated geometry of the molecule in the electronic ground and excited state, statements regarding the vibrational modes involved in the geometry change will be made.

5.3.1. Stationary Stokes-Raman and infrared spectra

In Fig. 5.5 (a) and (b), resonance Stokes Raman spectra of B-30 dissolved in GTA are plotted for excitation at 606 nm and 303 nm, respectively (sample concentration 2×10^{-3} M). Solvent Raman lines are indicated by (*), and contributions from spectrally unresolved solvent and solute lines are marked by (+). Closely positioned Raman lines are better resolved with 606 nm excitation due to the smaller bandwidth of the pulses, compared to 303 nm excitation. Most of the strong Raman bands occur under both excitation conditions. There are, however, significant changes of relative intensities in the Raman spectrum under excitation in the CT and in the LE band. The resonance Raman spectrum of the CT band shows some additional bands, which are weak or even not present with 303 nm excitation.

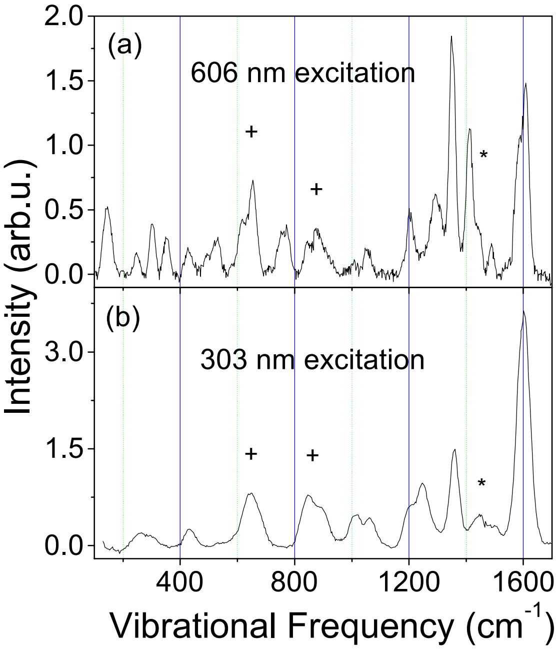

Fig. 5.5: Stationary Resonance Raman spectra of B-30 dissolved in GTA recorded by excitation in the charge transfer band (top) and in the locally excited band (bottom). Solvent lines are marked with *, and contributions from both solvent and solute lines with +.

Due to the limited performance of the polychromator without Notch filter, the low frequency region (ν<400 cm^{-1}) could not be recorded with a sufficient signal to noise ratio at 303 nm excitation.

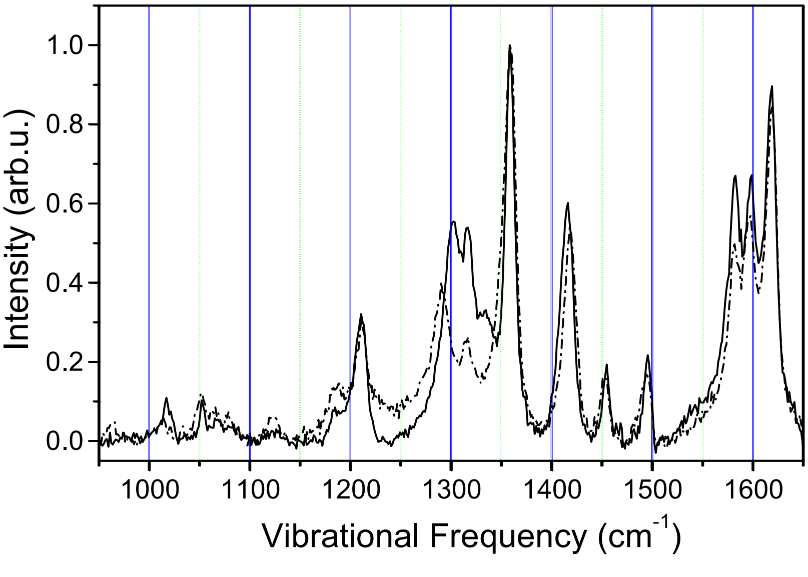

Fig. 5.6: Stokes-Raman spectra of B-30 dissolved in methanol (solid line) and in PC (dashed line).

The Stokes-Raman spectra recorded by excitation with 606 nm laser light are very similar for B-30 dissolved in PC and GTA. There is a difference in the 1250-1320 cm^{-1}

spectral region for B-30 dissolved in ETH or methanol, as seen in Fig. 5.6, probably due to the formation of H-bonds between solute and solvent [21, 22].

In Fig. 5.7 Raman spectra of B-30 dissolved in PC (2×10^{-2} M) are presented, recorded with 1064 nm by Brzezinka -see [23]- (lower panel) and with 600 nm excitation (upper panel), respectively.

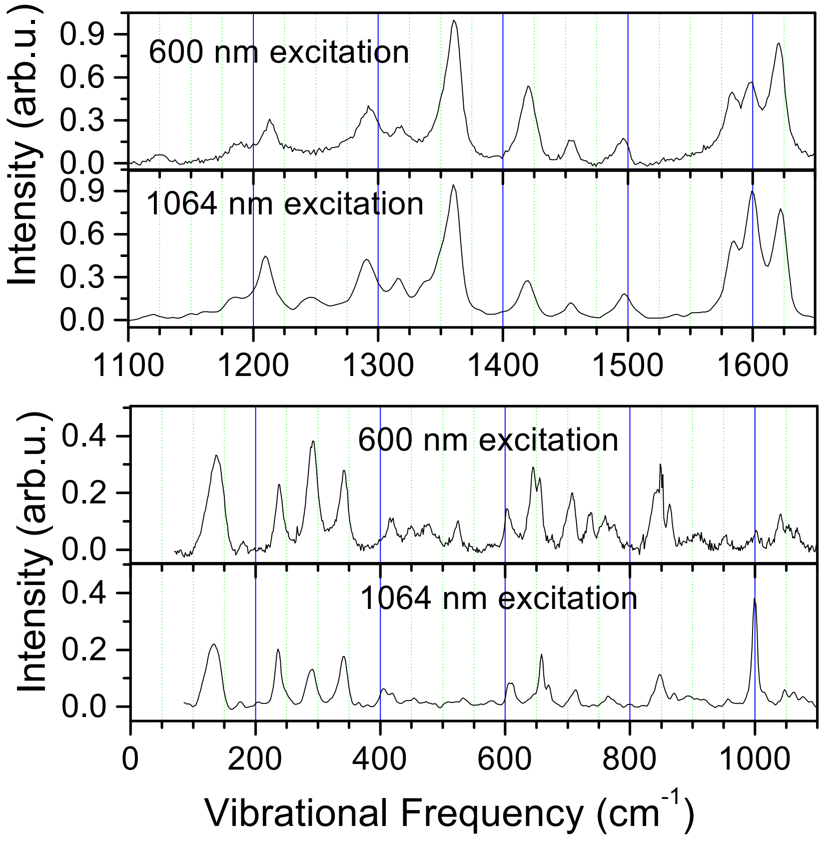

Fig. 5.7: Raman spectra of B-30 obtained after excitation in the CT band (600 nm) and off-resonance (1064 nm).

Raman spectra recorded with 600 nm excitation are resonance enhanced compared to excitation at 1064 nm by a factor of about 10. For off-resonance conditions, the solvent contribution has been subtracted from the original spectrum, whereas under electronic resonance the relative contribution of solvent Raman lines is negligible. The Raman spectrum recorded at 600 nm is in good agreement with the spectrum reported by McHale et al. recorded under similar excitation conditions (i.e., in the resonance with the CT transition) [21, 22]. In these papers, it has been reported that due to electronic resonance conditions, the depolarization ratios of all vibrations are close to $\rho=0.3$. In addition to the published vibrational frequencies (see [21, 22]), we found a rather strong low frequency line at 133 cm^{-1}. As will be discussed later, this mode is assigned to a torsional motion, which is assumed to play an important role in the ET reaction.

The Raman spectrum recorded at 1064 nm excitation shows the same vibrational pattern as the spectrum obtained with 600 nm excitation. However, we detect different relative intensities for some distinct Raman lines. For example, the Raman lines at 1622 cm^{-1} and 1419 cm^{-1} gain in their relative intensities under resonance excitation. Vice versa, we observe a strong line at 999 cm^{-1} with 1064 nm excitation which is rather weak under resonance excitation at 600 nm. Whether a Raman band gains or looses in relative intensity in changing the electronic resonance conditions depends on whether or not the normal mode is localized (spatially) in the same part as the electronic transition. The conclusions that can be derived will be discussed in paragraph 5.3.4.

The corresponding infrared spectrum of B-30 embedded in KBr (top) measured with a FTIR device together with a Raman spectrum of B-30 in PC (bottom) is presented in Fig. 5.8.

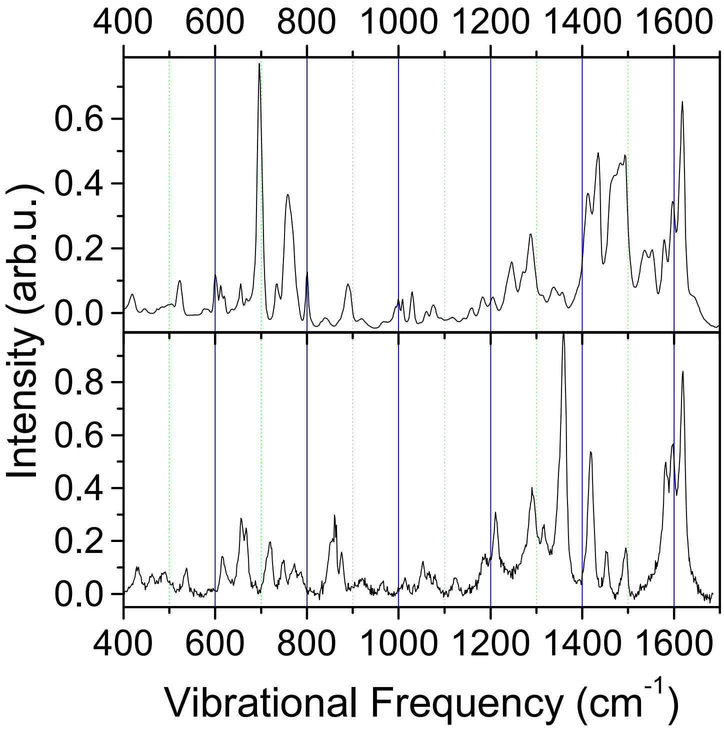

Fig. 5.8: Infrared spectrum of B-30 embedded in KBr (top) and Raman spectrum of B-30 dissolved in PC (bottom) for comparison.

5.3.2. Molecule geometry in ground and excited electronic state

Ground state geometry optimization and vibrational analysis of the complete B-30 molecule has been made by Dreyer [23]. He used the HF/3-21G (Hartree-Fock) method implemented in the program package GAUSSIAN98 [24]. For excited state calculations, the full structure was reduced to a model system solely consisting of the phenoxide and pyridinium rings and calculated with CI-singles/6-31G(d). For comparison, the ground state model structure was optimized at the HF/6-31D(d) level as well. All reported frequencies were scaled by a factor of 0.91 [25,26]. The obtained ground state geometry is shown in Fig. 5.9.

The most important geometry parameters are collected in Table 5.1. Bond angles are only given for the two cases in which the values deviate considerably from 120°. The numbering of atoms and notation of phenyl rings are shown in Fig. 5.9. The molecular structure is C_2 symmetric with a twisted chain of the phenoxide, pyridinium and phenyl ring C.

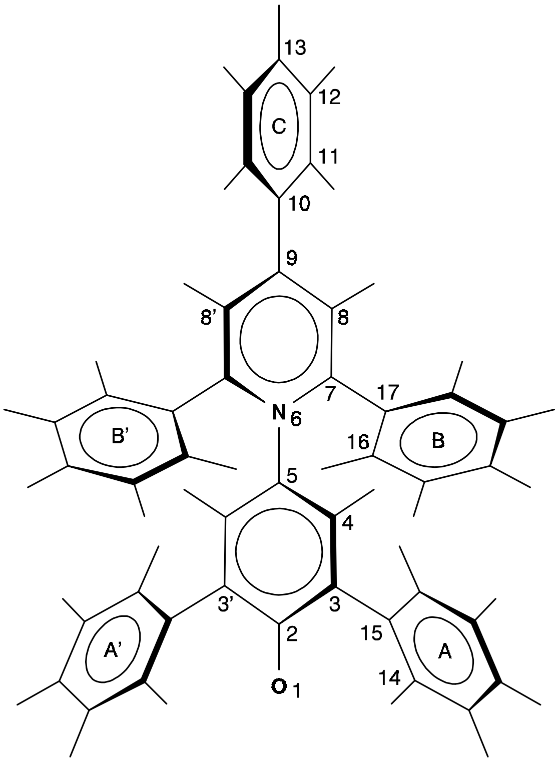

Fig. 5.9: Molecular structure of betaine-30 (B-30): see the numbering of atoms and naming of outer phenyl rings.

The most relevant geometry changes upon excitation to the first excited state are depicted in Figure 5.10.

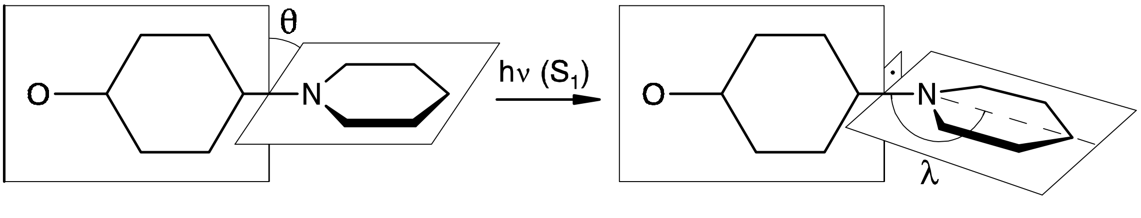

Fig. 5.10: Geometry change of B-30 after excitation in the CT band

The phenoxide and pyridinium rings are moved from a twisted conformation into a perpendicular position. This has also been observed by Lobaugh and Rossky [27] and was earlier considered by Bartkowiak and Lipinski [28]. In addition, the pyridinium ring tilts and the nitrogen atom becomes pyramidalized by $\lambda = 167.8°$. These two geometrical changes can be induced by the torsional and N-inversion vibrational modes, which were identified in the Raman spectrum at 133 and 291 cm^{-1} (see paragraph 5.3.3). The dipole moment is reduced from 15 D (18 D for the complete molecule) in the ground state to 3 D in the excited state, in reasonable agreement with experimental values of 16 D in the ground state and 6 D in the S_1 state [19]. The electronic wave function mainly corresponds to a HOMO-LUMO $\pi \rightarrow \pi^*$ transition. The HOMO is localized in the phenoxide ring, whereas the LUMO is distributed over both rings.

The calculated bond length changes from the ground to the excited state allow to make the prediction that bands which dominantly contain C–O (Raman: 1582 cm^{-1}, IR: 1553 cm^{-1}) or C–N stretching (Raman: 1209 cm^{-1}) contributions are expected to shift to higher wavenumbers in the excited state because of the increased bond order.

The calculated B-30 geometry can be roughly evaluated with respect to the crystal structure of 2,6-diphenyl-4-(4-bromophenyl)-N-(p-oxy-m,m'-diphenyl)-phenyl-pyridinium-betaine-monoethanolate, a B-30 structure with bromine attached at C_{13} and crystallized with an ethanol molecule, which distorts the crystal structure from C_2 symmetry [28]. The twist angle θ between the phenoxide and the pyridinium ring is calculated to 68° in the electronic ground state, which is very close to the crystal structure value of 65° [29]. Earlier semiempirical PPP [27] and AM1 [28, 30] calculations resulted in values of 52°, 60° and 48°, respectively. Phenyl ring C is twisted by χ = 45° with respect to the pyridinium ring, which is in the same order of magnitude as the sample range of χ values reported by Lobaugh and Rossky [27]. The experimental value measured under conditions of a frozen molecule is only 18° [29]. The twist angle of the A/A' and B/B' phenyl rings amount to ξ = 34° and ϕ = 54°, respectively, again in qualitative agreement with results of Lobaugh and Rossky [26]. Standard bond lengths

Table 5.1: Optimized geometry parameters for the complete B-30 molecule and the model structure. The dipole moments are given in D, bond lengths in pm, bond and dihedral angles in degrees.

[a] The model structure comprises the phenoxide and pyridinium rings (cf. Fig. 5.9).

[b] Experimental crystal structure of B-30 substituted with bromine at C_{13} and crystalized with ethanol hydrogen-bonded to O_1 [28].

[c] Both rings are orthogonal to each other, the N-pyramidalization causes the deviation from 90°.

	S_0 (full) HF/3-21G	S_0 (model) [a] HF/6-31G(d)	S_1 (model) CIS/6-31G(d)	experiment. [b]
μ (dipole moment)	18	15	3	
O_1–C_2	125.1	121.9	120.5	129.1
C_2–C_3	145.7	145.6	147.2	144.8/144.5
C_3–C_4	136.9	135.6	134.7	139.1/141.0
C_4–C_5	138.6	140.9	142.5	139.3/137.8
C_5–N_6	146.7	142.4	138.7	147.9
N_6–C_7	136.0	134.5	140.0	135.5/136.7
C_7–C_8	137.7	137.3	135.6	139.0/138.7
C_8–C_9	138.6	138.5	140.3	141.7/139.8
C_9–C_{10}	148.3	–	–	148.5
C_{10}–C_{11}	139.0	–	–	140.5/141.0
C_{11}–C_{12}	138.2	–	–	142.3/140.3
C_{12}–C_{13}	138.4	–	–	137.0/140.1
C_3–C_2–$C_{3'}$	115.8	114.4	116.1	118.1
C_8–C_9–$C_{8'}$	117.7	118.3	117.2	116.5
C_5–N_6–C_9 (λ)	180.0	180.0	167.8	180.0
C_4–C_5–N_6–C_7 (θ)	67.9	42	98 [c]	65
C_8–C_9–C_{10}–C_{11} (χ)	45.2	–	–	18

C_{14}–C_{15}–C_3–C_2 (ξ)	34	–	–	26/65
C_{16}–C_{17}–C_7–N_6 (ϕ)	55	–	–	65/70

for C–O single and double bonds are 135 pm [C(sp^2)–O] and 121 pm [C=O] [31]. Thus, the calculated C_2–O_1 bond length of 125.1 pm corresponds to a significant degree of double bond character. Accordingly, the adjacent C_2–$C_{3,3'}$ bonds are noticeably stretched in comparison to aromatic C–C bonds in benzene, and thus the phenoxide ring structure exhibits some degree of quinoidal character. All other phenyl ring structures are nearly uniform. This is in qualitative agreement with experimental values, although the quinoidal character is somewhat less pronounced [29]. However, the experimental C_2–O_1 bond length of 129.1 pm is elongated because of hydrogen bonding in the crystal structure, which also affects the quinoidal pattern. For the uncomplexed molecule the C_2–O_1 bond length can be expected to be much closer to the calculated value of 125.1 pm. The C_5–N_6 bond length of 146.7 pm between the phenoxide and the pyridinium ring is even somewhat longer than a standard [C(sp^2)–N(sp^2)] bond length of 140 pm [31], probably induced by the repulsion between the outer phenyl rings A and B. This long C_5–N_6 bond suggests that there is no significant degree of conjugation between the rings, in accordance with the large twist angle θ being far away from the coplanar conformation, which would maximize conjugation. Similar considerations hold for all other bonds between rings.

5.3.3. Assignment of the Raman vibrations

Experimental Raman frequencies obtained in PC (Fig. 5.7) and the corresponding experimental infrared frequencies measured in KBr (Fig. 5.8), together with the calculated vibrational frequencies at the ab-initio Hartree-Fock level (HF/3-21G) made by Dreyer [23], relative intensities, depolarization ratios and assignments, are collected in Table 5.2. The good agreement of experimental and calculated patterns allows to assign the majority of observed Raman and infrared bands.

The high-frequency Raman bands at 1622 and 1601 cm^{-1} (Fig. 5.7) originate from aromatic stretching modes of the pyridinium ring combined with aromatic stretching modes of the outer phenyl rings. In contrast, the mode at 1582 cm^{-1} corresponds to an aromatic stretching mode of the phenoxide ring and thus, exhibits C–O as well as C–N (PhO–Pyr) bond stretching character. The similarity of the frequencies with those measured in the infrared spectrum (Fig. 5.8) suggests that the three high frequency infrared bands are the same as the corresponding Raman bands.

A band being dominated by the C–O stretching motion is only observed in the infrared spectrum at 1553 cm^{-1}. In agreement with the calculated C_2–O_1 bond length of 125.1 pm, this frequency reveals partial double bond character. The region between 1350 and 1550 cm^{-1} contains several intense Raman and infrared band, which are mainly characterized by aromatic ring stretching motions. The most intense Raman band measured in polypropylene carbonate with excitation at 1064 nm occurs at 1355 nm and can be attributed to a stretching mode of the pyridinium ring combined with stretching modes of outer phenyl rings B and C against the pyridinium ring. The band at 1290 cm^{-1} corresponds to stretching modes of the phenoxide ring together with stretching modes of the adjacent phenyl rings A and the nitrogen from the pyridinium ring. The infrared bands

Table 5.2: Experimental Raman (in propylene carbonate, 1064 nm excitation) and infrared (in KBr) frequencies, calculated (HF/3-21G) vibrational frequencies (in cm^{-1}), experimental and calculated depolarization ratios ρ and assignments.

Abbreviations: Pyr = pyridinium ring; PhO = phenoxide ring; PhA,B,C = outer phenyl rings (cf. Figure 5.9); C–N = PhO–Pyr; ν = stretching; δ = in-plane deformation; γ = out-of-plane deformation; τ = torsion.

According to calculation the ground state molecule possess C$_2$-symmetry. Modes belonging to the B-species are designated (B), the other belong to A-species.

experimental			theoretical		assignment
Raman	ρ	IR	HF/3-21G(d)	ρ	
1622	0.52	1618	1617	0.60	ν(Pyr) + ν(PhB,C)
1601	0.48	1597	1611	0.13	ν(Pyr) + ν(PhA,B,C)
1582	0.53	1578	1593	0.74	– ν(PhO) + ν(C–O) + ν(C–N)
		1553	1553	0.49	ν(C–O) – ν(C–N) + ν(PhO)
		1535	1541 (B)	0.75	ν(Pyr)
1497	0.31		1501 (B)	0.75	ν(PhO)
1454	0.47				
		1435	1444 (B)	0.75	ν(PhO) + ν(PhA)
		1412	1423	0.75	ν(Pyr) + ν(PhB,C)
1419	0.37		1431	0.38	ν(Pyr–PhB) + ν(C–N)
1355	0.28		1344	0.08	ν(Pyr) + ν(Pyr–PhB,C)
1315	0.22		1290 (B)	0.75	δ(CH, PhO) + δ(CH,Pyr)
			1280 (B)	0.75	δ(CH, PhO) – δ(CH,Pyr)
1290	0.26		1252	0.12	ν(PhO) + ν(PhO–PhA) + ν(C–N)
		1287	1290	0.75	δ(CH,PhO) + δ(CH,Pyr)
		1271	1280	0.75	δ(CH,PhO) – δ(CH,Pyr)
1248	0.43		1235	0.75	ν(Pyr–PhC) + ν(Pyr–PhB)
1209	0.47		1185	0.44	ν(C–N) + δ(CH, PhO) + δ(CH, PhA,C)
999	0.16		1004	0.06	breathing(PhA,B,C) + γ(CH, PhO)
			1001	0.15	γ(CH, PhO) + γ(CH, PhO) + γ(CH, PhA)
			991	0.22	breathing(PhB,C) + γ(CH, Pyr)
		889	883	0.75	γ(C–O)
850	–		840	0.37	δ(PhO) + δ(Pyr) + γ(CH, PhB)
		758			
		696			
658	0.40		693	0.30	γ(Pyr)
341	0.36		361 (B)	0.75	N-inversion + wagging(PhA,B)
			348	0.46	γ(PhO)
291	0.54		296	0.28	γ(PhO)
			290	0.75	N-inversion
235	0.30		242	0.75	γ(Pyr) + translation (Pyr–PhC)
			229	0.74	γ(PhO)
			227	0.06	translation (Pyr–PhB,C)
133	0.36		130	0.55	τ (PhO–Pyr)
			116	0.24	τ (PhO–Pyr–PhC)

at 1287 and 1271 cm^{-1} are attributed to out-of-plane C–H deformation modes. The C_5–N_6 stretching motion dominantly contributes to the Raman band located at 1209 cm^{-1}. The sharp band at 999 cm^{-1} corresponds to breathing modes of the outer phenyl rings in combination with C–H out-of-plane deformation modes. The infrared band at 889 cm^{-1} has been assigned to an out-of-plane deformation mode of the C–O bond.
Four Raman bands are measured in the low frequency range below 400 cm^{-1}. At 341, 291 and 235 cm^{-1} a pattern of three bands with comparable intensities is observed. The central peak is attributed to the inversion of the pyridinium nitrogen atom, whereas the upper one corresponds to an out-of-plane deformation mode of the phenoxide ring and the lower one to a translation of the phenyl rings B and C against the pyridinium ring. The broad band at 133 cm^{-1} can be assigned to torsional motions of the three rings in the chain. Two different normal modes in this frequency region are calculated. The one at 130 cm^{-1} corresponds to the torsional motion of the phenoxide and pyridinium rings, which is described by a variation of the dihedral angle θ. The second calculated peak at 116 cm^{-1} is characterized as torsional motion of the pyridinium ring against the phenoxide ring and phenyl ring C, which is specified by changing the dihedral angles θ and χ.
The N-inversion and the torsional modes of the skeleton are very important molecular motions, which mediate the rearrangement in the first excited state as deduced from computational results.

5.3.4. Discussion of the dispersion effects

Next, the dispersion effects described in paragraph 5.3.1 will be discussed. The majority of the intense Raman bands in the range 1650 to 1200 cm^{-1} originate from modes localized in the phenoxide-pyridinium core of B-30 (see paragraph 5.3.3). They will experience high resonance enhancement under resonant excitation. Normal modes which dominantly originate from vibrational motions of the outer phenyl rings (like the band at 999 cm^{-1}, which is assigned to breathing motions of the outer phenyl rings), decrease in relative intensity under resonant excitation compared to non-resonant excitation. In the low wavenumber region, we observe a strong enhancement for the mode at 291 cm^{-1}, which contains a large contribution from the wagging motion of the central C–N bond in accordance with the calculated geometrical changes (see paragraph 5.3.3). In contrast, the dispersion effect for the torsional mode at 133 cm^{-1} is not so pronounced, although the band exhibits a very large origin shift (and consequently very high Franck-Condon factor), as deduced from its very high Raman intensity. The resonance Raman intensity is sensitive to geometrical changes between the electronic ground state and the corresponding Franck-Condon region of the excited electronic state, i.e., to geometrical changes occurring within the first tens of femtoseconds. As calculated by Lobaugh and Rossky by molecular dynamic simulations in acetonitrile [27], torsional relaxation of the central dihedral angle θ is supposed to occur on a time scale of several picoseconds. In other words, the vibration at 133 cm^{-1} will experience less resonance enhancement than the high frequency vibrations due to its slow torsional motion.

5.3.5. Overtones and combination tones

In addition to the fundamental frequencies, a manifold of overtones and combination tones can be observed by excitation of a B-30 solution ($2x10^{-2}M$) in UV at 303 nm. These spectra gives an indication about the anharmonicity of the potential energy surface

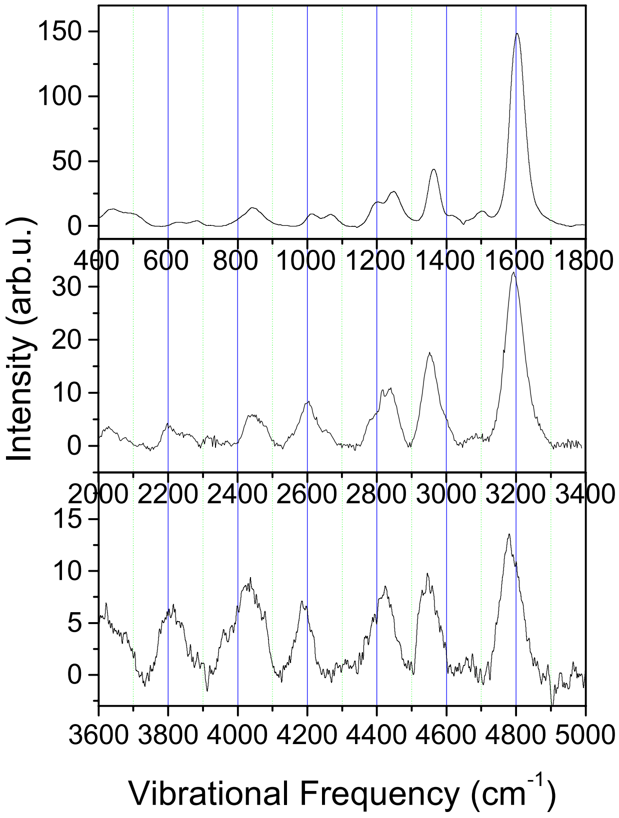

Fig. 5.11: Overtones and combination tones observed in B-30 dissolved in PC measured by 303 nm excitation.

in the ground state, and about the amounts of the anharmonic frequency shifts that should be observed in the case of intra-mode vibrational relaxation from the high-excited vibrational levels to the vibrational ground state. A typical Raman spectrum including the overtone region is shown in Fig. 5.11.
Besides the first and second overtone of the 1603 cm^{-1} vibration at 3196 cm^{-1} and 4790 cm^{-1}, respectively, combination tones of other frequencies with the 1603 cm^{-1} frequency can be observed. An anharmonical shift of approximately 12 and 19 cm^{-1} can be deduced for the first and second excited vibrational level of the 1603 cm^{-1} vibration, respectively.

5.4. Transient spectra and a view into the mechanism of back-ET

Detailed information about the mechanism of the intramolecular back-ET in B-30 can be further obtained by investigating the time evolution of the vibrational modes after back-ET by anti-Stokes Raman spectroscopy. It reflects the population change of particular modes and can be used to monitor the specific participation of vibrational modes in the ET. A detailed study of the transient anti-Stokes Raman spectra will be presented under the conditions of ‘solvent controlled’ and ‘vibrational controlled’ regime. The spectra are measured in the electronic ground singlet state after the back-ET. Transient Stokes-Raman spectra in the excited singlet state will also be presented.

5.4.1. Kinetics of the anti-Stokes Raman modes in slowly and fast relaxing solvents

The sample (concentration 3x10^{-3}M) was excited via the charge transfer transition by pulses at 606 nm (30-100 μJ energy/ pulse), while the probe pulses at 303 nm (2-10 μJ energy/pulse) were resonant with the transition to the locally excited state of the B-30 molecule. This scheme is illustrated in Fig. 5.12. The probe pulse was polarized linearly at magic angle (54.7^{o}) relative to the pump, in order to avoid temporal changes of the anti-Stokes Raman intensities due to molecular reorientation. Probing the very weak anti-Stokes Raman spectra in the UV spectral region is advantageous because the scattering signal increases with a ν^4 dependence (where ν is the excitation frequency), and because of the lack of fluorescence.

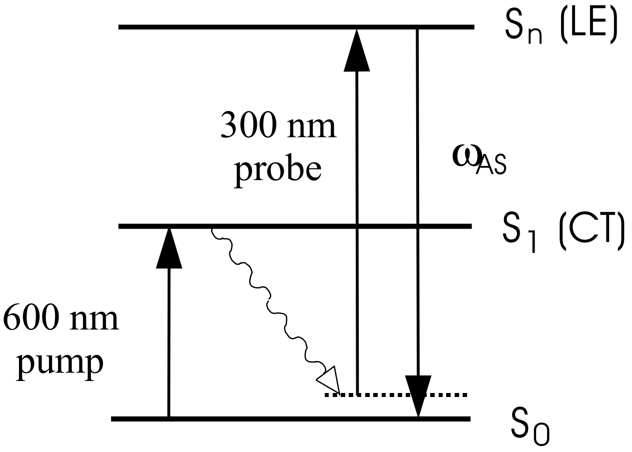

Fig. 5.12: Schema for excitation and probing of anti-Stokes Raman mode in B-30.

Time resolved anti-Stokes Raman spectra were obtained by subtraction of the spectra recorded with pump pulses at a negative delay of 50 ps with respect to the probe pulse from the corresponding spectra measured at positive delays. Thus, stray light due to the pump pulse does not contribute to the signal and the observed signals are due to the vibrational excess population only produced by back-ET in the electronic ground state. A typical accumulation time for each spectrum at a fixed delay was 200 s and up to ten of such spectra were averaged to obtain a sufficiently high signal to noise ratio. Integrated Raman intensities were determined - after subtraction of a base line - by fitting the Raman bands by Voigt line shapes.

Time-resolved anti-Stokes Raman spectra were measured for B-30 dissolved in PC, GTA and ETH. The solvation time of PC at room temperature is very fast (about 1 ps), and the measured back-ET of B-30 in PC equals the solvation time [4]. This is a typical case of ‘solvent controlled’ back-ET, where a considerable amount of energy is transferred to the solvent during the back-ET process. Despite the clearly longer solvation time of GTA (about 100 ps) and ETH (about 15 ps) at room temperature, the measured back-ET is only slightly longer (3.6 ps in GTA and 5.6 ps in ETH) [3-5]. These are typical cases of ‘vibrational controlled’ back-ET, where energy transfer to the solvent plays a minor role.

In Fig. 5.13 are presented the spectra recorded for a solution of B-30 dissolved in PC (left side) with an accumulation time of 30 min. for each spectrum, and GTA (right side) with an accumulation time of 90 min. for each spectrum, for different delays between excitation and probing. All strong Raman lines of the Stokes Raman spectrum with 303 nm excitation (Fig. 5.5) can be identified in the anti-Stokes Raman spectrum as well. Moreover, it is easy to observe a build-up of the anti-Stokes Raman intensities first in the high-frequency region within a few picoseconds and their subsequent decay that is slightly slower than the rise and accompanied by a redistribution of the relative intensities. The rise times are significantly slower for B-30 dissolved in GTA than in PC.

At early times, the mode with the highest frequency (1603 cm^{-1}) is dominant, at later times (t > 10 ps) the Raman bands with lower frequencies (1360 cm^{-1}, 1200/1245 cm^{-1}, 1013 cm^{-1}, 650 cm^{-1} and 435 cm^{-1}) increase in relative intensity. Within our experimental accuracy of ±15 cm^{-1}, the spectral positions of the Raman bands are independent of time delay.

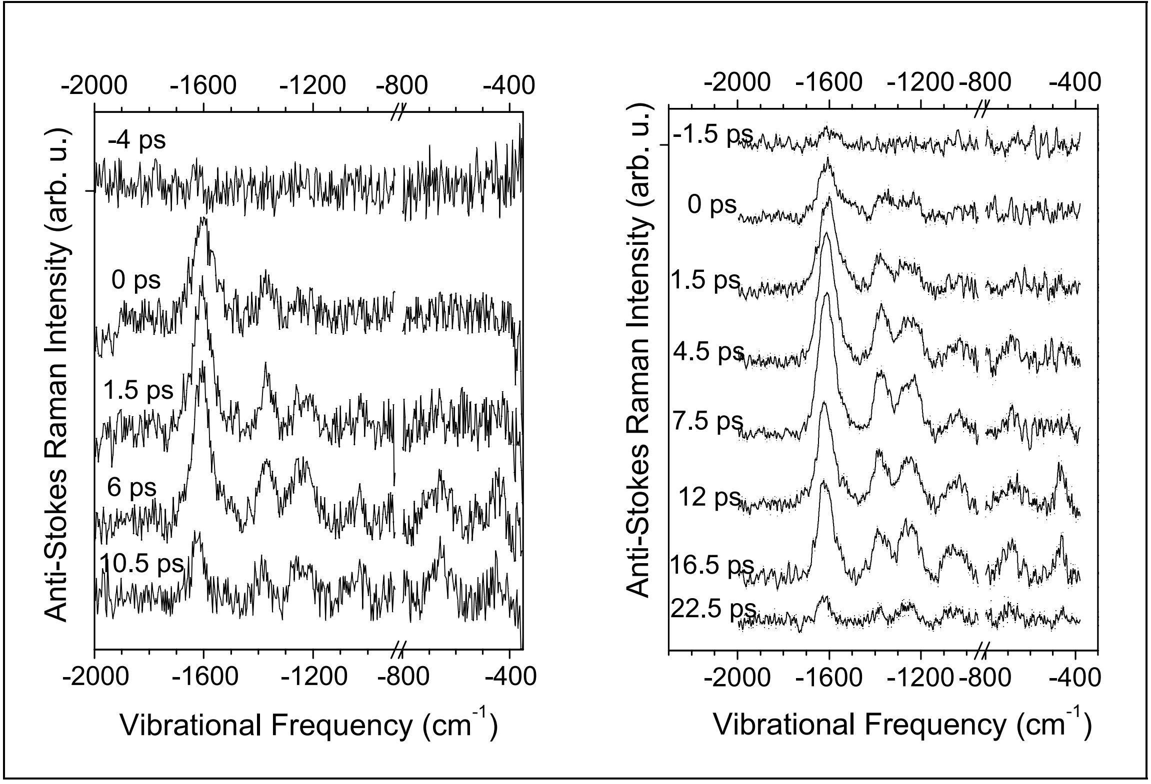

Fig.5.13: Transient anti-Stokes Raman spectra of B-30 dissolved in PC (left) and GTA (right).

In Fig. 5.14, the time evolution of the Raman intensities of the modes at 1603 cm^{-1}, 1360 cm^{-1} and 1200/1245 cm^{-1} are presented for B-30 dissolved in PC (left side), GTA (middle) and ETH (right side). In the upper panel of Fig. 5.14 the time-resolved small signal amplification of Sulforhodamine 101 (see also Fig. 3.10) which is used for determining the time resolution in the experiment and the zero-delay point is shown as well in addition.

Rise and decay of the anti-Stokes Raman intensities reflect the population dynamics of the corresponding excited vibrational levels. To quantify the different rise and decay times, the population dynamics of the vibrational level i, n_i, is modeled in a three level scheme. Within this simplest possible approximation, vibrational population n_i is fed into the level *i* from an initially excited level *p* of population $n_p(0)$ with a time constant t_1, while the population of the i^{th} level decays to a further level with a time constant t_2.

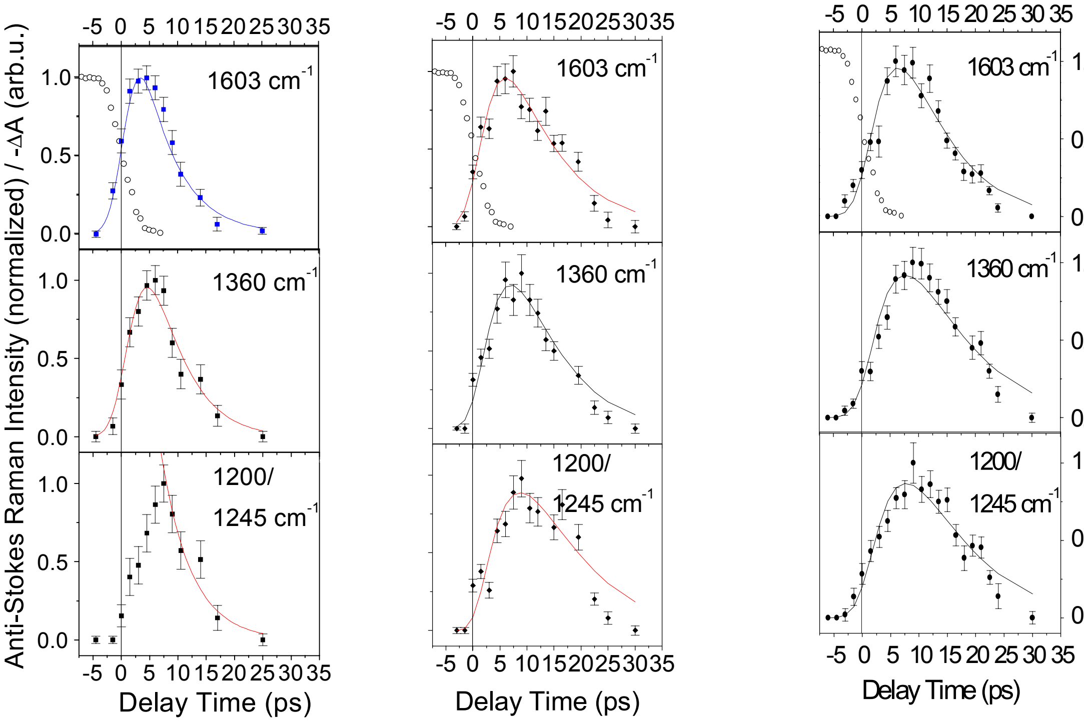

Fig. 5.14: Kinetics of the vibrational modes at 1603, 1360 and 1200/1245 cm^{-1} measured for B-30 dissolved in PC (left), GTA (middle) and in ETH (right), respectively.

The population kinetics is thus described as follows:

$$n_i(t) = n_p(0)\frac{e^{-\frac{t}{t_1}} - e^{-\frac{t}{t_2}}}{\frac{t_1}{t_2} - 1} \qquad (5.2)$$

This time behavior is convoluted with the cross correlation function of the pump and probe pulses. The solid lines in Fig. 5.14 give the results of the fit using this model.

In most cases, this approach reproduces the experimental results quite well. The Raman signals show a non-instantaneous intensity rise with the delay between pump and probe pulses, which is different for different modes and solvents. Mode selectivity, i.e., differences in rise times of the different vibrational modes, is most pronounced for B-30 in PC. The mode with the highest vibrational frequency at 1603 cm^{-1} exhibits the fastest rise time of $t_1 \leq 1$ ps, i.e. within the time resolution of the experiment, whereas a rise time of $t_1 = 3$ ps is determined for the vibration at 1360 cm^{-1}. The intensity of the Raman band at 1200/1245 cm^{-1} increases even more delayed, but does not follow a simple single exponential kinetics. All vibrational modes - within experimental uncertainties - decay single exponentially with a time constant of $t_2 = 5$ ps. For B-30 dissolved in GTA and in ETH (Fig. 5.14), the temporal rises of the anti-Stokes Raman intensities are slower than in PC solution. Furthermore, mode selectivity is less pronounced in GTA solution than for B-30 in PC and nearly disappears for B-30 in ETH. The decay of anti-Stokes Raman intensities is somewhat slower in GTA and ETH solutions, compared to B-30 dissolved in PC.

The time constants (rise time: t_1, decay time: t_2) determined for the vibrations at 1603 cm^{-1}, 1360 cm^{-1} and 1200/1245 cm^{-1} for B-30 dissolved in PC, GTA and in ETH are summarized in Table 5.3. Back-ET times determined from transient absorption measurements (5) are given for comparison in the first column of Table 5.3.

Table 5.3: Rise and decay times of anti-Stokes Raman kinetic curves measured for B-30 dissolved in propylene carbonate (PC), glycerol triacetin (GTA) and ethanol (ETH). They were approximated by an expression with two monoexponential terms (rise time t_1, decay time t_2). Back-ET times [3, 5] ($\tau_{\text{back-ET}}$) are given in parentheses.

Vibrational frequency	1603 cm^{-1}		1360 cm^{-1}		1200/1245cm^{-1}	
solvent	t_1, ($\tau_{\text{back-ET}}$) [ps]	t_2 [ps]	t_1 [ps]	t_2 [ps]	t_1 [ps]	t_2 [ps]
PC	1.0±0.3, (1.1)	6.1±0.4	3.0±0.5	5.0±0.6	nonexp.	5.3±1.2
GTA	3.8±0.8, (3.5)	8.5±1	5.0±1.2	6.7±1.2	7.0±1.3	7.5±1.7
ETH	5.6±1.2, (6.1)	5.6±1.3	7.0±1.4	7.0±1.4	7.1±1.5	7.0±1.6

5.4.2. Selective excitation of the vibrations and IVR after back-ET

The spectra in Fig. 5.5 show a change of the Raman intensities when changing the conditions of resonant Raman enhancement, i.e., when moving from 600 nm (CT band) to 300 nm (LE transition). This behavior reflects the different origin shifts of the vibrational potentials in the CT and LE states of B-30. Despite the differences in the Raman spectra, most of the bands that are strong in the CT resonance Raman spectrum show high intensities in the LE Raman spectrum. Consequently, it is possible to monitor the vibrational kinetics of the majority of modes involved in ET by recording the time-resolved anti-Stokes Raman spectra in resonance with the LE transition (except for the rather intense vibrations at 1290 cm^{-1} and 1419 cm^{-1} and the vibrations below 400 cm^{-1}).

The rate of intramolecular electron transfer is frequently approximated by Fermi's Golden Rule (FGR) (see paragraph 2.3.5):

$$k_{ET} = \frac{2\pi}{\hbar}\left|V_{el}\right|^2 F \tag{5.3}$$

V_{el} is the electronic coupling constant for the two diabatic electronic states and F contains a sum taken over the FC factors of the modes active in electron transfer. Each of them is multiplied by an effective energy conservation factor. On the basis of FGR, Wynne et. al. [32,33] derived a formula giving the transfer probability for the vibrational mode j (frequency ω_j) from the zero level in the donor (CT) state to the n^{th} level in the acceptor state:

$$\rho_n^j = N_j \left| < 0_j \mid n_j > \right|^2 \int_{-\infty}^{+\infty} dt e^{-\lambda_s kT \frac{t^2}{\hbar^2} - i\left(\lambda_S - n_j h\omega_j + \Delta G^0\right)\frac{t}{\hbar} + g^j(t)} \tag{5.4}$$

Here, N_j is a normalization factor, k the Boltzmann constant, λ_S the solvent reorganization energy, ΔG_0 the energy gap between the reactant and product state and $g^j(t)$ is the line shape function.

Assuming equal mode frequencies in the CT and electronic ground states, the coupling strength of each mode j is given by its respective FC overlap $<0\,|\,n_j>$:

$$<0|n_j> = \frac{z_j^{n_j}}{\sqrt{2^{n_j} n_j!}} e^{-0.25 z_j^2} \qquad (5.5)$$

with the origin shift parameter $z_j = \sqrt{\frac{m_j \omega_j}{\hbar}}\, q_{0j}$, which can be derived from the Raman spectrum with the relation: $z^2 \approx I/\omega_j$, where I is the intensity of the Raman mode ω_j, m_j and q_{0j} are the effective mass and origin shift of the j^{th} mode with frequency ω_j. From Eq. (5.4) and Eq. (5.5) it follows that applying comparable origin shift parameters of most transfer active modes (close to $z_j \leq 1$ as determined for B-30 [21,22]), the transfer is most favorable into those modes which bridge the gap with a minimum of quanta n. For a large energy gap and similar $z_j \leq 1$, i.e., the situation in B-30, the probability for back-ET mediated by high frequency modes should be higher than by low frequency modes. In agreement with this argument, the time-resolved data show pronounced vibrational excess populations of high-frequency modes, in particular of the mode at 1603 cm^{-1}.

In accordance with the predictions derived from FGR, the time-resolved data for B-30 in PC show different rise times of three prominent modes in the transient Raman spectra (see Fig. 5.14). A rise time of the 1603 cm^{-1} band in the PC solution close to the back-ET time of 1 ps indicates that this mode is excited predominantly by back-ET, whereas low frequency vibrations are less effective in accepting energy. However, from the almost equal decay times of the three modes it can be concluded that excitation of the modes at 1360 cm^{-1} and 1200/1245 cm^{-1} via energy transfer from the 1603 cm^{-1} mode is not effective. In contrast, those modes are partly excited by transfer via indirect channels of internal vibrational redistribution. The presented experimental data do not allow to determine other pathways of IVR which may represent such indirect channels.

A comment should be made on the role of low-frequency modes for back-ET. Low frequency vibrations can be involved in back-ET provided that their FC factors are large enough. In a variety of electron transfer systems, coherent wave packet propagations with frequencies on the order of 150 cm^{-1} have been observed. Molecular dynamics simulations for B-30 predict that the torsional motion between the phenoxide and the phenolate ring tunes the gap between the electronic ground and the CT state and thus promotes back-ET [27]. The vibration at 133 cm^{-1} has been identified as a torsional mode (Table 5.2). It exhibits about half the intensity of the mode at 1603 cm^{-1}. It has been suggested that the corresponding torsional motion of B-30 promotes back-ET [27]. Taking into account that the origin shift parameter can be approximated by $z^2 \approx I/\omega$ (I: intensity of the band), it is obvious that z^2 is considerably higher for this low frequency mode than for modes in the high frequency region. These considerations suggest that the 133 cm^{-1} torsional mode is part of the reaction coordinate. Further time-resolved studies are required to clarify this point experimentally.

Less pronounced differences in the rise times of the different vibrational bands are expected for the case that back-ET times are comparable to the time scale of IVR. This is the case for B-30 in GTA and ETH (see Table 5.3). Here, IVR processes strongly influence the observed rise times for all modes. Thus, these data clearly demonstrate the transition from a mode-specific behavior of B-30 in PC to IVR-dominated vibrational dynamics of B-30 in ETH.

5.4.3. Nonequilibrium vibrational populations of B-30 after back-ET

The data collected in Table 5.3 demonstrate that the measured rise times of the anti-Stokes Raman line at 1603 cm^{-1} agree with the respective decay time of the first excited electronic state $\tau_{back\text{-}ET}$ in different solvents. The rise times of the other vibrations are longer or comparable with t_1 of the 1603 cm^{-1} vibration. The anti-Stokes Raman frequencies coincide with the corresponding Stokes Raman frequencies measured at low intensities and do not change with delay. Consequently, the observed anti-Stokes Raman lines are due to population of excited vibrational levels of the electronic ground state. Furthermore, there are no apparent anharmonic shifts of the Raman line at 1603 cm^{-1} with delay time. This indicates that the anti-Stokes Raman signal originates mainly from the v=1 level of that mode, possibly with a small additional contribution from the v=2 and v=3 states. As high-lying levels of this mode are directly populated by the back-ET, the rise of nonequilibrium population in low-lying levels is determined by the electron transfer time and the intra-mode relaxation time. The experimental data show that the rise time of the Raman signal is identical to $\tau_{back\text{-}ET}$, pointing to a fast subpicosecond intra-mode relaxation.

Assuming equal scattering cross sections for the Stokes and anti-Stokes Raman signals[18], it is possible to make a rough estimation of the peak value of the population of the excited vibrational levels. A value of about 3% compared to the ground state population of the 1603 cm^{-1} mode can be obtained. However, despite the broad spectral width of the absorption near 300 nm of about 4700 cm^{-1}, different Raman excitation profiles for Stokes and anti-Stokes Raman scattering are to be expected [16, 18, 34, 35]. It is more realistic to assume that the ratios of cross sections between the vibrations in the Stokes Raman spectrum are nearly equal to the ratios between the same vibrations in the anti-Stokes Raman spectrum. Furthermore, following assumption has been made: the contributions from higher excited vibrational levels (v>1) to the anti-Stokes Raman scattering can either be neglected or contribute with approximately the same cross section as the v=1 vibrational level. Consequently, the "relative vibrational excess populations" have been derived by dividing the anti-Stokes Raman intensities with the corresponding relative Raman cross sections which, in turn, have been calculated from the Stokes Raman intensities recorded at 300 nm (see Table 5.2).

In Fig. 5.14 the relative vibrational populations at different delay times are shown for B-30 in PC and GTA. It is obvious for all solvents that the vibrational populations deviate substantially from thermal equilibrium within the first few picoseconds. For delay times of 1.5 ps, 3 ps and – for B-30 in GTA – 7.5 ps, one finds smaller populations of low-frequency than of high frequency modes, in contrast to equilibrium (Bose-Einstein) statistics. For example, the population of the mode at 1360 cm^{-1} exceeds the 1200/1245 cm^{-1} population. This finding reflects the incomplete randomization of vibrational energy among the Raman active modes, pointing to a relatively slow intramolecular thermalization of the vibrational system on a picosecond time scale. At delay times longer than about 10 ps, the vibrational populations are close to equilibrium statistics, which is characterized by a vibrational temperature of the subgroup of these vibrations.

However, the procedure for determining the vibrational temperature has to be very carefully analyzed, since higher excited vibrational levels in the ladder of a certain mode can contribute to the anti-Stokes Raman signal. For off-resonant excitation conditions the Raman signal increases linearly with the quantum number of the vibrational level [36]. In contrast, for resonance Raman excitation conditions a shift of the maxima of REP to longer wavelengths for excited vibrational levels and a decrease of the corresponding anti-Stokes Raman efficiency has been calculated for canthaxanthin [16]. Consequently, a decrease of the anti-Stokes Raman signal with increasing level number for excitation near the maximum of the absorption band seems to be more likely for the experimental conditions used here.

To evaluate how the estimated temperature deviates for different models, the distributions of excess populations shown in Fig. 5.15 has been approximated under three different assumptions. These are: the anti-Stokes Raman signal

(i) grows linearly with the level number, i.e., $\sigma_i = i \cdot \sigma_0$ where σ_i is the Raman cross-section of the vibrational level i, and σ_0 is the Raman cross-section of the ground state vibrational level

(ii) is independent of the level number, i.e., $\sigma_i = \sigma_{i-1} = ... = \sigma_0$ and

(iii) originates from the lowest excited vibrational level only, i.e., $\sigma_i = 0$ for $i > 1$

In order to fit the experimental points in Fig. 5.15, the anti-Stokes difference signal M_j for one mode ω_j normalized to the corresponding Stokes signal I_{Sj} have been derived (see Appendix 1) for the three cases:

(i)
$$M_j = \frac{I_{AS\,j}(T_e) - I_{AS\,j}(T_r)}{I_{S\,j}(T_r)} = \frac{n_j(\omega_j, T_e) - n_j(\omega_j, T_r)}{n_j(\omega_j, T_r) + 1} \qquad (5.6)$$

with the thermal population distribution:

$$n(\omega, T) = \left[e^{\frac{\hbar\omega}{kT}} - 1 \right]^{-1} \qquad (5.7)$$

Here, T_r and $T_e(t)$ are the vibrational temperatures before and after excitation by the pump pulse, respectively. T_r is the room temperature considered 300K, and $T_e(t)$ is a parameter which will be obtained form the fit of the experimental points with Eq. (5.6).

(ii)
$$M_j = e^{-\frac{\hbar\omega_j}{kT_e}} - e^{-\frac{\hbar\omega_j}{kT_r}} \qquad (5.8)$$

(iii)
$$M_j = e^{-\frac{\hbar\omega_j}{kT_e}} / (n_j(\omega_j, T_e) + 1) - e^{-\frac{\hbar\omega_j}{kT_r}} / (n_j(\omega_j, T_r) + 1) \qquad (5.9)$$

For B-30 in PC solution after 9 ps delay time, the assumptions (i) and (ii) result in different temperatures of 740 K and 595 K, respectively. The four modes 440, 1200/1245, 1360 and 1603 cm^{-1} can not be approximated reasonably assuming (iii), but they can be fitted excluding the vibration at 440 cm^{-1}. In the latter case, the fit with (ii) and (iii) results in the same temperature, with an uncertainty of 60 K. The minor influence on the result, despite the completely different assumptions, can be understood by taking into account that - for the temperature range under consideration - the populations of excited levels of the high frequency modes are below 15%. In contrast, for the 440 cm^{-1} vibration the contributions from higher excited levels are significant.

Changes in the Raman cross sections comparing excited vibrational levels should play a minor role for low frequency modes and consequently, (iii) can not be applied.

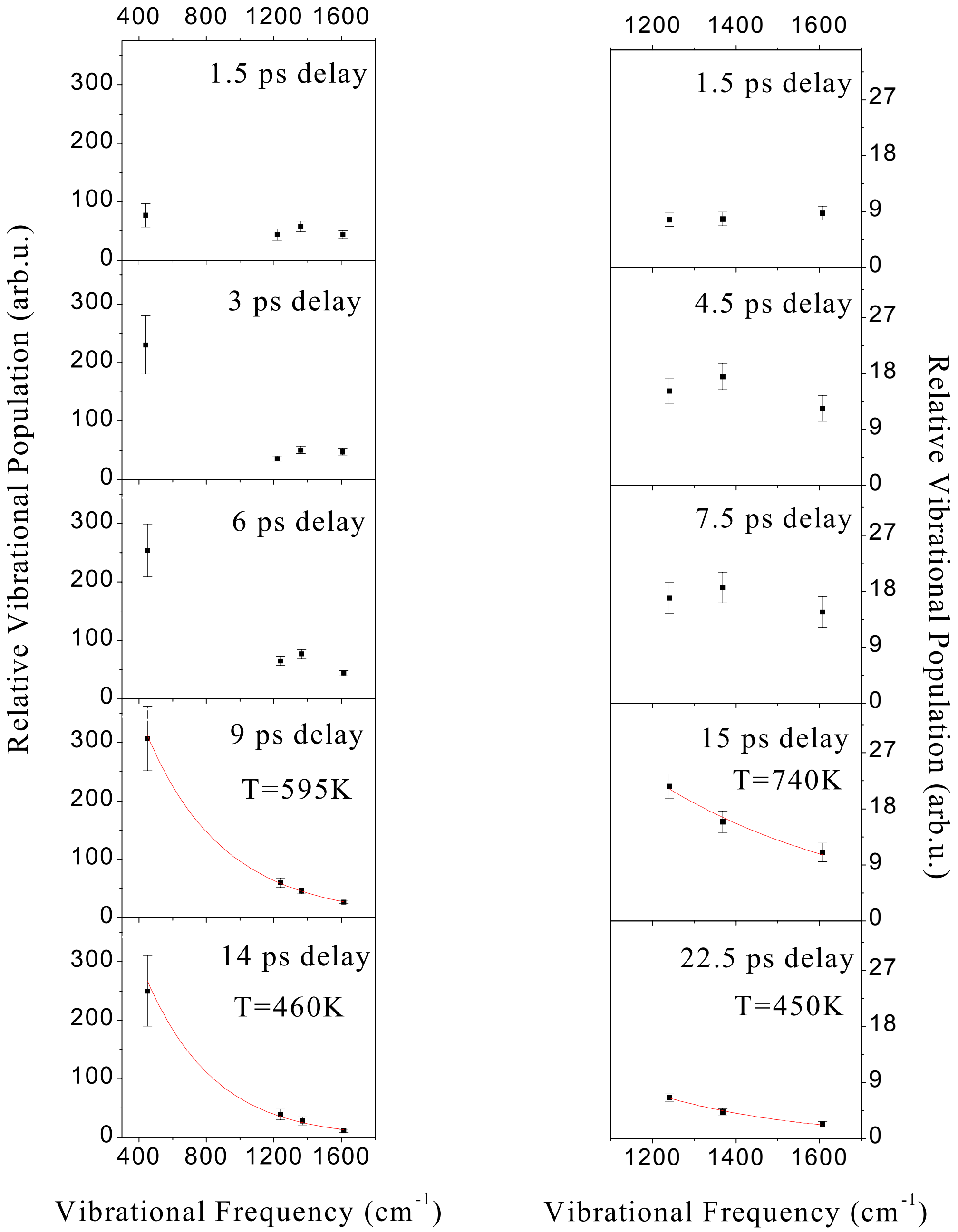

Fig. 5.15: Relative vibrational populations of the excited vibrational levels different vibration determined at different delays. Left: B-30 dissolved in PC; right: B-30 dissolved in GTA. Vibrational temperatures for relative vibrational populations, which have been fitted by Eq. (5.8), are given in the insert.

Because the temperatures T_e derived from (ii) represent a lower limit in comparison to (i), it is instructive to estimate and to compare temperatures T_e at thermal equilibrium based on assumption (ii). The temperature values T_e obtained at different delays are given in the inserts of Fig. 5.15. The measurements with B-30 in ETH give temperature values slightly higher than in the GTA solution. Vibrational temperatures T_e in ETH solution are 830, 730 and 530 K at 15, 18 and 22.5 ps, respectively.

For a comparison of the temperatures T_e derived for the subgroup of Raman active modes with the equilibrium temperature T_{equ} which would be achieved in case of random distribution over all vibrational modes (degrees of freedom) of the molecule, the temperature T_{equ} has been derived applying the expression:

$$\sum_{j=1}^{3N-6} \hbar\omega_j n_j(\omega_j, T_r) + \Delta E = \sum_{j=1}^{3N-6} \hbar\omega_j n_j(\omega_j, T_{equ}) \qquad (5.10)$$

$\Delta E \approx 16500\,\mathrm{cm}^{-1}$ is the photon energy of the pump pulse, T_r is the room temperature (300 K), $n_j(\omega_j, T_{r,equ})$ has the same form as in Eq. (5.7) and N=71 is the number of atoms in the molecule. An equilibrium temperature of T_{equ}= 520 K has been obtained. T_{equ} represents the maximum temperature at thermal equilibrium within the complete molecule as it neglects any flow of energy to the solvent shell. Nevertheless, T_e determined for early delay times in different solvents is always higher than T_{equ}. This suggests that (a) back-ET transfers most of the excess energy to the Raman active modes involved in the reaction, and (b) thermalization within the vibrational manifold of B-30 is incomplete even 10 to 15 ps after photoexcitation.

It is interesting to note that the measured excess of the temperature T_e above the calculated equilibrium temperature T_{equ} is larger for B-30 in GTA and ETH than in PC. This can be rationalized by taking into account that in the solvent controlled regime a considerable part of the absorbed energy is deposited into the solvent directly. For B-30, solvent reorganization energies between 3000 cm^{-1} and 6000 cm^{-1} have been estimated (see paragraph 5.2 and [4, 21, 22]). In contrast, if the solvation time exceeds the back-ET time, a larger fraction of the initial excitation energy is randomized within the solute before dissipation to the surrounding becomes efficient. Consequently, lower vibrational temperatures in the PC compared to the GTA and ETH solutions are to be expected. The experimental results are therefore in accordance with the theoretical models of intermolecular energy transfer during back-ET in the solvent controlled regime and under conditions of a "frozen" solvent.

5.4.4. Transient Stokes-Raman spectra in the first excited electronic singlet state

In order to gain more information about the change of the molecular structure during the ET process, a study of the Raman spectra in the first excited singlet state has been made. The excitation and probing scheme used is shown in Fig. 5.16.

The pump-probe transient spectra contain implicit information about the geometrical changes that occurs in the first excited singlet state, and follow up the relaxation to the ground state. Moreover, they can give an indication about the dynamics of H-bonds, if they are present.

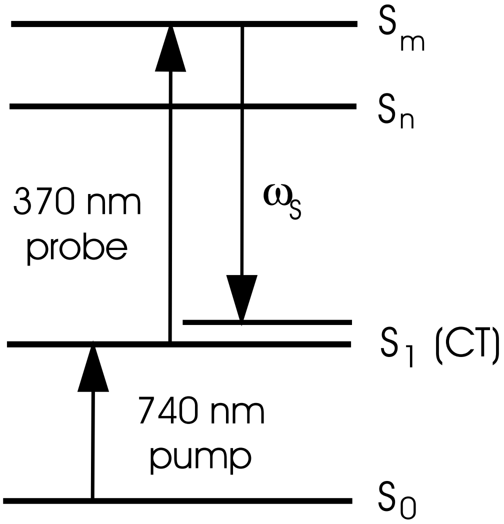

Fig.5.16: Schema for excitation and probing of Stokes Raman scattering in the excited singlet state of B-30.

Stokes-Raman spectra were measured for B-30 dissolved in dimethylsulfoxide and pentanol. These solvents are advantageous because of comparatively longer excited state lifetimes and good solubility of B-30. Pentanol forms H-bonds with B-30 as indicated by the appearance of the strong Raman band at 1300 cm^{-1} (see Fig. 5.17.a and the discussion of Fig. 5.6).

For the measurement of Raman spectra in the first excited electronic state, 600 nm laser light was used for excitation (maximum of the CT absorption band is 580 nm in pentanol and 620 nm in dimethylsulfoxide). The probe laser wavelength at 364 nm was generated by frequency doubling of the radiation at 728 nm, which, in turn, has been obtained by Raman shifting (SRS) of the 600 nm laser wavelength in high pressure methane. In this way, the resonance Raman enhancement due to transient absorption near 400 nm has been used.

The following procedure was applied in order to subtract the contribution of the molecules in the ground state to the spectra in the excited electronic state:

(i) a Stokes-Raman spectrum was recorded by excitation with the probe laser light at 364 nm, with a negative delay (-50 ps) between the pump and probe (i.e., the probe pulse hits the sample 50 ps before the pump pulse). A ground state Raman spectrum of B-30 was obtained in this way, as shown in Fig. 5.17.a for B-30 dissolved in pentanol;

(ii) a spectrum at a positive delay between the pump and probe pulses was measured;

(iii) the spectrum measured at point (i) was subtracted from the spectrum (ii).

Fig. 5.18 shows the kinetic of the intensity of the Raman band at 1000 cm^{-1} recorded at different delays between the pump and probe pulses. Other bands show the same dependency. In this experiment, a cross-correlation time between the pump and probe pulses of about 6 ps has been determined (under the assumption of gaussian pulses) by measuring the Kerr signal generated in CS_2 (open squares in Fig. 5.18). In a two-level model, a decay time of 10.8 ps of the Raman intensity has been determined from the fit of the experimental points. This decay time is very similar with the excited state lifetime measured by Barbara et al. (11 ps) in a transient absorption experiment, giving evidence that the observed spectra originate from the excited electronic state of B-30.

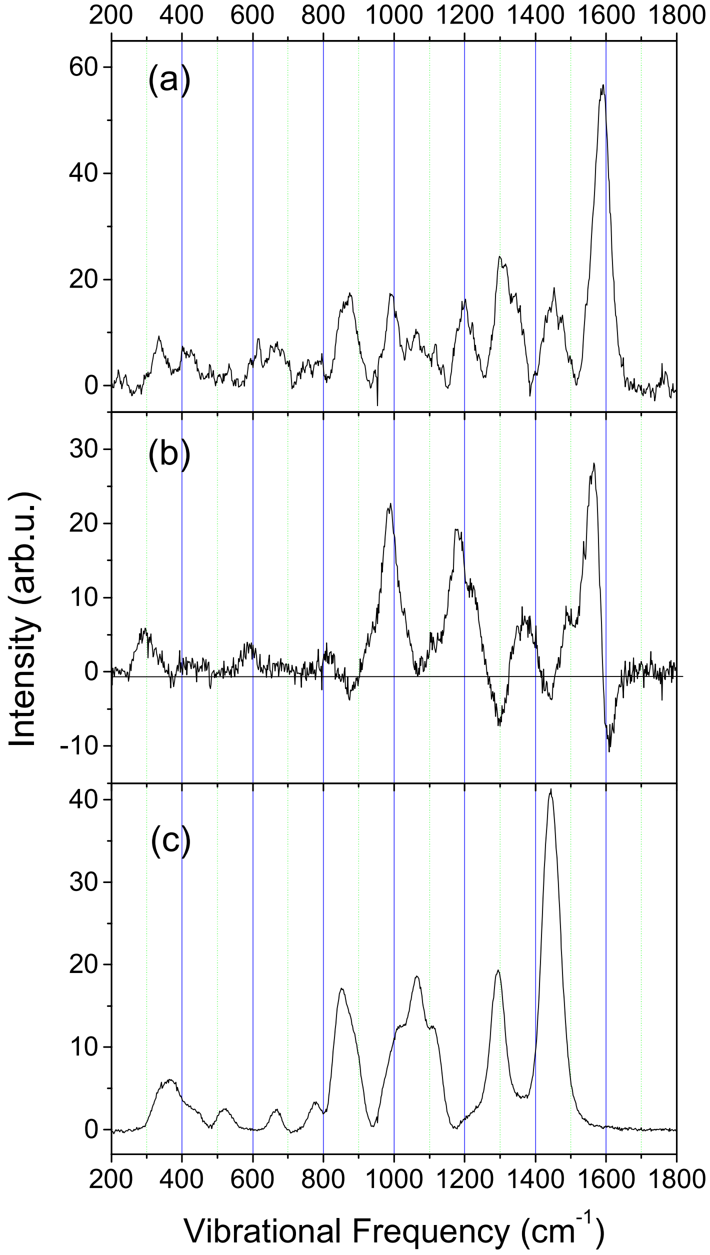

Fig. 5.17: Stokes-Raman spectrum of B-30 in pentanol in the electronic ground state with 364 nm excitation (a) and in the first excited electronic state by pump with 600 nm and probe with 364 nm (b). For comparison, a Raman spectrum of neat pentanol is shown, by excitation with 364 nm laser light (c).

The spectrum measured at 6 ps delay is presented in Fig. 5.17.b. The neat solvent spectrum is shown for comparison in Fig. 5.17.c.

Positive and negative components in the spectrum in Fig. 5.17.b are due to the contributions of Raman vibrations in the excited state and to depletion of the electronic ground state, respectively. Considerable frequency shifts of some Raman vibration in the excited state compared to the ground state are observed.

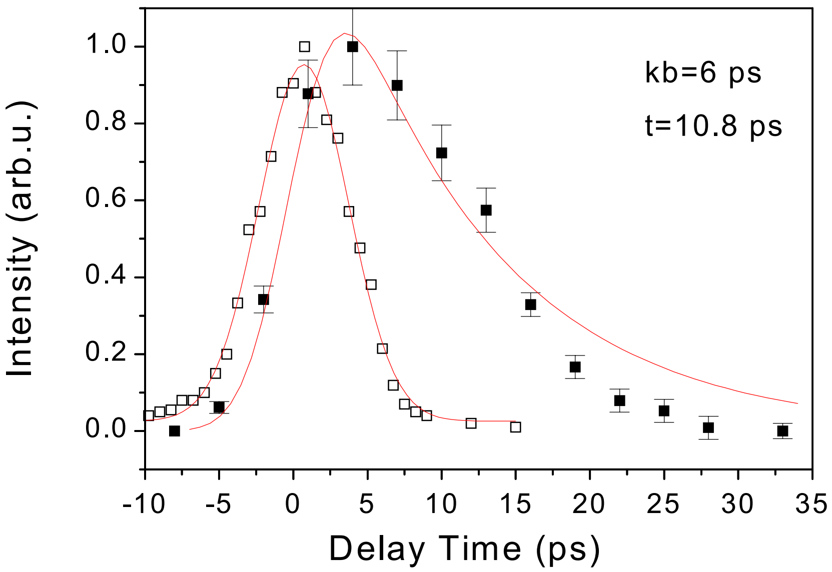

Fig. 5.18: Kinetic of the Stokes-Raman spectra in the first excited electronic state of B-30 dissolved in pentanol (solid squares) and cross-correlation between pump and probe beams (open squares). The solid lines are the fits of the experimental points.

The S_1 Raman pattern of B-30 does not show significant differences when dissolved in GTA or dimethylsulfoxide compared to the spectra recorded in pentanol (in contrast to the S_0 Raman pattern, where differences at 1300 cm^{-1} are observed for protic and aprotic solvents as shown in Fig. 5.6). As pentanol forms H-bonds in the electronic ground state, H-bond breaking after photoexcitation and subsequent formation of these bonds after back-ET may occur. For a discussion of these processes, the experimental results are summarized here:

(a) different patterns of Stokes-Raman spectra of B-30 dissolved in protic and aprotic solvents measured in S_0;

(b) similar patterns of Stokes-Raman spectra of B-30 dissolved in protic and aprotic solvents measured in S_1;

(c) no changes in the pattern of the S_0 Stokes-Raman spectra of B-30 dissolved in pentanol measured before and after back-ET, i. e., at negative (-20 ps) and positive (>10 ps) delay times.

Points (a) and (b) implies two possible explanations:

(i) there is no H-bond in the excited electronic state, i.e., the H-bond which are seen in S_0 in protic solvents breaks during (or after) ET.

(ii) there are H-bonds in S_1, but the respective vibrations are not Raman active.

In both cases there will be no differences in the spectra in S_1. However, if the bonds break, and either breaking in S_1 or formation in S_0 is long compared to the generation of S_1 (ET) or formation of S_0 population (back-ET), changes should be observable. Point (c) shows that this is not the case.

5.5. Conclusions

In conclusion, it has been shown that stationary, as well as time-resolved Stokes- and anti-Stokes Raman scattering, combined with ab-initio calculations is a powerful method to gain information about the role of vibrational modes in the process of ultrafast intramolecular ET.

As we are able to assign the observed vibrational (Raman and IR) spectra to the vibrational pattern calculated by HF methods, this gives strong support that the optimized geometries used in this calculations are close to the geometry of the real molecule. Additionally, very high FC-factors of the Raman line assigned to the torsional motion, and the pronounced dispersion effect of the line assigned to a N-inversion motion, indicate that strong geometrical changes accompanies the ET reaction. Furthermore, strong change of the C=N bond length has to be expected during ET.

Time-resolved anti-Stokes resonance Raman measurements give evidence that the vibrational modes which accept the main amount of excess energy due to back-ET can be predicted from the stationary resonance Raman spectra measured in the CT absorption band. In other words, our results are at least qualitatively in accordance with the calculations derived from FGR, that predicts that high frequency modes with strong FC factors are the main accepting modes.

In agreement with this predictions, our time-resolved anti-Stokes resonance Raman measurements show that the rise time of the vibrational population of the mode with highest frequency at 1600 cm^{-1} is near to the corresponding b-ET in different solvents. Modes with lower frequencies appear more or less delayed in comparison to the high frequency mode.

Our measurements also demonstrate the interplay of direct vibrational excitation and intramolecular vibrational redistribution in the electronic ground state, occurring after back-ET. In fast relaxing solvents, i.e., in the case of fast back-ET, we clearly observe mode specific rise times due to dominance of direct excitation of high frequency modes. In contrast, in slow relaxing solvents, i.e., in the case of slow back-ET, the selectivity diminishes, probably due to dominant IVR processes.

Furthermore, this study also give information concerning the process of IVR. We observe strong non equilibrium populations in the first picoseconds for all Raman modes which are assumed to accept the main amount of excess energy. About 10 ps after excitation (depending on the solvent), a Boltzmann distribution between these modes has been established, and determination of the temperature of this subgroup of vibrations becomes appropriate. A value of about 10 ps for thermalization is in contrast to earlier measurements [10] and supports recent measurements.

These investigations also show that the temperature observed in the subgroup of vibrations exceeds the vibrational temperature that could be achieved in the molecule if the whole excess energy available in the back-ET process were distributed thermally over all internal degrees of freedom of an isolated molecule, even 10-15 ps after photoexcitation. This indicate that even at this time, thermalization in the whole molecule is not complete. Different temperatures observed in slowly and fast relaxing solvents can be attributed to different pathways of vibrational relaxation in the excited electronic state under condition of „solvent“ and „vibrational“ controlled regime, respectively.

Although far from being complete, we have obtained essentially new information about excitation and vibrational energy redistribution in a complex molecule undergoing ultrafast intramolecular ET. This study demonstrates that anti-Stokes resonance Raman scattering is a valuable tool for the study of the ET mechanism in condensed matter. Extending time-resolution and sensitivity, even more information can be expected.

References

[1] A.M. Kjaer, and J. Ulstrup, *J.Am.Chem.Soc.*, **109** (1987) 1934

[2] E. Akesson, G.C. Walker, and P.F. Barbara; *J. Chem. Phys*. **95** (1991) 4188

[3] A.E. Johnson, N.E. Levinger, W. Jarzeba, R. Schlief, D.A.V. Kliner, and P.F. Barbara; *Chem. Phys*. **176** (1993) 555

[4] G.C. Walker, E. Akesson, A.E. Johnson, N.E. Levinger, and P.F. Barbara; *J. Phys. Chem*. **96** (1992) 3728

[5] A.E. Johnson, N.E. Levinger, W. Jarzeba, R. Schlief, D.A.V. Kliner, and P.F. Barbara; *Chem. Phys*. **176** (1993) 555

[6] R.A. Marcus, *J. Chem. Phys*. **24** (1956) 966, *J. Chem. Phys*. **24** (1956) 979, *J. Chem. Phys*. **26** (1957) 867, *J. Chem. Phys*. **26** (1957) 872, *Discuss. Faraday Soc*. **29** (1960) 21

[7] H. Sumi, and R.A. Marcus, *J.Chem.Phys*., **84** (1984) 4894

[8] J. Jortner, and M. Bixon; *J. Chem. Phys*. **88** (1988) 167

[9] M. Bixon, and J. Jortner; *J. Chem. Phys*. **176** (1993) 467

[10] T. Elsaesser, and W. Kaiser, *Annu. Rev. Phys. Chem*. **42** (1991) 83

[11] R.J. Sension, A.Z. Szarka, and R. Hochstrasser, *J. Chem. Phys*. **97** (1992) 5239

[12] C. Chudoba, S. Lutgen, T. Jentzsch, E. Riedle, M. Woerner, and T. Elsaesser, *Chem. Phys. Lett.* **240** (1995) 35

[13] K.G. Spears, X. Wen, and S.M. Arrivo, *J. Phys. Chem*. **98** (1994) 9693

[14] R.B. Dyer, K.A. Peterson, P.O. Stoutland, and W.H. Woodruff; *Biochemistry* **33** (1994) 500

[15] J.W. Petrich, J.L. Martin, D. Houde, C. Poyart, and A. Orstag; *Biochemistry* **26** (1987) 7914

[16] T. Nakabyashi, H. Okamoto, and M. Tasumi; *J. Phys. Chem*. A **101** (1997) 3494

[17] P. D.L. Phillips, J.-M. Rodier, and A.B. Myers; *Chem. Phys*. **175** (1993) 1

[18] S.C. Hayes, M.P. Philpott, and P.J. Reid; *J. Phys. Chem. A* **103** (1999) 5534

[19] W. Liptay, B. Dumbacher, and H. Weisenberger; *Z. Naturforschung A* **23** (1968) 1613

[20] C. Reichardt, in „*Molecular interactions*", Vol. 3, eds H. Ratajczak, W.J. Orville- Thomas, Wiley, New York (1982) 241

[21] Y. Zong, and J.L. McHale; *J. Chem. Phys*. **106** (1997) 4963

[22] Y. Zong, and J.L. McHale; *J. Chem. Phys*. **107** (1997) 2920

[23] S. Hogiu, J. Dreyer, M. Pfeiffer, K-W. Brzezinka, and W. Werncke; accepted in *J. Raman Spectrosc.*

[24] Gaussian 98 (Revision A.2), M. J. Frisch, G. W. Trucks, H. B. Schlegel, G. E. Scuseria, M. A. Robb, J. R. Cheeseman, V. G. Zakrzewski, J. A. Montgomery, R. E. Stratmann, J. C. Burant, S. Dapprich, J. M. Millam, A. D. Daniels, K. N. Kudin, M. C. Strain, O. Farkas, J. Tomasi, V. Barone, M. Cossi, R. Cammi, B. Mennucci, C. Pomelli, C. Adamo, S. Clifford, J. Ochterski, G. A. Petersson, P. Y. Ayala, Q. Cui, K. Morokuma, D. K. Malick, A. D. Rabuck, K. Raghavachari, J. B. Foresman, J. Cioslowski, J. V. Ortiz, B. B. Stefanov, G. Liu, A. Liashenko, P. Piskorz, I. Komaromi, R. Gomperts, R. L. Martin, D. J. Fox, T. Keith, M. A. Al-Laham, C. Y. Peng, A. Nanayakkara, C. Gonzalez, M. Challacombe, P. M. W. Gill, G. B. Johnson, W. Chen, M. W. Wong, J. L. Andres, M. Head-Gordon, E. S. Replogle and J. A. Pople, Gaussian, Inc.,; Pittsburgh PA.

[25] A. Scott, and L. Radom, *J. Phys. Chem.* **100 (**1996) 16502-16513

[26] M. D. Halls, and H. B. Schlegel, *J. Chem. Phys*. **111 (**1999) 8819-8824

[27] J. Lobaugh, P. Rossky; *J. Phys. Chem. A* **103** (1999) 9432

[28] W. Bartkowiak, and Lipinski, *J. Phys. Chem. A* **102 (**1998) 5236

[29] R. Allmann *Z. Kristallogr*. **128 (**1969) 115

[30] S. R. Mente, and M. Maroncelli. *J. Phys. Chem. B* **103 (**1999) 7704

[31] P. Rademacher, „*Strukturen organischer Moleküle*“, Ed. M. Klessinger; VCH: Weinheim (1987)

[32] K. Wynne, C. Galli, R.M. Hochstrasser; *J. Chem. Phys*. **100** (1994) 4797

[33] K. Wynne, G.D. Reid, R.M. Hochstrasser; *J. Chem. Phys*. **105** (1996) 2287

[34] K.T. Schomacker, O. Bangcharoenpaurpong, P.M. Champion; *J. Chem. Phys*. **80** (1984) 4701

[35] A.P. Shreve, R.A. Mathies; *J. Phys. Chem*. **99** (1995) 7285

[36] G.Seifert, R. Zuerl, and H. Graener, *J. Phys. Chem*. **103** (1999) 10749

6. Summary

In this thesis vibronic coupling effects occurring at conical intersections have been studied. Strong vibronic coupling between two excited electronic singlet states in a polyene-like molecule, DPH, and the role of vibrational modes in photoinduced ultrafast back-ET in B-30 have been studied with a picosecond time-resolved CARS and Raman set-up, respectively. The experimental apparatus developed in our laboratory is a 50 Hz repetition rate system based on laser amplification in a dye medium. The high pulse energy (200 µJ) which can be obtained allows easily converting the wavelength by SHG or SRS, and thus confer the necessary variability for the experiments. The results obtained show a new effect of excited state vibronic coupling in diphenylpolyenes and allow a view into the mechanism of ET.

6.1. Vibronic coupling in DPH

In a picosecond time-resolved CARS experiment it was possible to observe for the first time two very broad and unusual up-shifted vibrational frequencies in the excited singlet state of DPH, which have frequencies higher than frequency region of the C=C stretching mode [1]. This effect was not observed in the two closest related diphenylpolyenes, DPB and DPO, where the gap between the first and second excited singlet states is larger than in DPH. Time-resolved and polarization sensitive CARS measurements carried out for DPH dissolved in a large variety of solvents differing in their physical properties [1, 2] gave evidence of vibronic coupling between the first and second excited singlet states. Quantum-chemical calculations and time-resolved CARS measurements allowed to assign the two broad vibrational frequencies to the C=C symmetric stretching mode. Two explanations have been discussed: (i) the simultaneous existence of two rotamers, where the two frequencies originate from „different molecules“ and (ii) a model of vibronic coupling by an asymmetric low frequency mode [3]. According to this model, the two up-shifted frequencies originate from the double-well potential formed along the C=C coordinate due to the vibronic mixing between the nearly degenerate low lying excited electronic states [3, 4]. The experimental findings are thus related to a pseudo-Jahn-Teller effect due to nonadiabatic coupling between the first and second excited singlet states in DPH.

6.2. Back-ET in B-30

Excitation of high-frequency vibrational modes after photoinduced b-ET and subsequent IVR has been observed for the first time in B-30 [5]. In the primary event, high frequency Raman active modes are most effective in accepting energy. This is in accordance with predictions derived from Fermi’s Golden Rule.

However, for complete explanation of the vibrational population kinetics, additional channels of IVR have to be taken into account [6]. Although energy transfer between the Raman active modes has been finished after about 10 to 15 ps, thermalization is not yet complete in the whole molecule. Interplay between vibrational excitation and intramolecular vibrational redistribution in the electronic ground state after back-ET has also been observed. It has been demonstrated that the time-scale for IVR is about 10 ps.
An assignment of the observed Raman vibrations allowed to determine the role of the respective vibrations in the ET transfer process at a molecular level [7]. In particular, the torsional mode between the pyridinium and phenoxide rings and the N-inversion mode are expected to play a significant role in the geometry changes in the excited electronic state and in the back-ET.

In conclusion, this thesis tries to give a microscopic view of two specific photophysical processes occurring in condensed matter. The results should contribute to an understanding of the mechanism of energy transfer between the excited states of polyenes, and to help to elucidate the role of vibrational modes in ET reactions. The experimental results are also a test for quantum-mechanical calculation performed in large molecules.
By developing a system with higher temporal and spectral resolution, it will be possible to obtain more details about these processes.

References

[1] S. Hogiu, W. Werncke, M. Pfeiffer, A. Lau, T. Steinke; „Picosecond time-resolved CARS spectroscopy of a mixed excited singlet state of diphenylhexatriene“, *Chem. Phys. Lett*. **287** (1998) 8

[2] S. Hogiu, W. Werncke, M. Pfeiffer, A. Lau; „Evidence of strong vibronic coupling in the first excited singlet state of diphenylhexatriene by picosecond CARS spectroscopy“, *Chem. Phys. Lett*. **303** (1999) 218

[3] M. Pfeiffer, W. Werncke, S. Hogiu, A. Kummrow, A. Lau; „Strong vibronic coupling in the first excited singlet state of diphenylhexatriene by an asymmetric low-frequency mode“, *Chem. Phys. Lett*. **295** (1998) 56

[4] W. Werncke, S. Hogiu, M. Pfeiffer, A. Lau; „Strong S_1-S_2 vibronic coupling and enhanced third order hyperpolarizability in the first excited singlet state of diphenylhexatriene studied by time-resolved CARS“, *J. Phys. Chem. A*, **104 (**2000) 4211-4217

[5] S. Hogiu, W. Werncke, M. Pfeiffer, T. Elsaesser; „Mode specific vibrational kinetics after intramolecular electron transfer studied by picosecond anti-Stokes Raman spectroscopy“, *Chem. Phys. Lett*. **312** (1999) 407

[6] S. Hogiu; W. Werncke, M. Pfeiffer, J. Dreyer, T. Elsaesser; „Mode specific vibrational excitation and energy redistribution after ultrafast intramolecular electron transfer“, accepted for publication in *J. Chem. Phys.*

[7] S. Hogiu, J. Dreyer, M. Pfeiffer, K.-W. Brzezinka, W. Werncke; „Vibrational analysis and excited state geometrical changes of betaine-30 derived from Raman and infrared spectra combined with ab initio calculations“, accepted for publication in *J. Raman Spectrosc.* .

Appendix 1

Vibrational population measured with anti-Stokes Raman intensity

The Raman intensity I_{raman} can be written as:

$$I_{raman} = \sum_i n_i \sigma_i I_{laser} \qquad \text{(A.1)}$$

where σ_i is the Raman cross-section for the level i, n_i is the population of the level i, and I_{laser} is the incident laser intensity.

The measured difference signal normalized to the corresponding Stokes intensity is:

$$M = \frac{I_{AS}(T_e) - I_{AS}(T_r)}{I_{St}(T_r)} \qquad \text{(A.2)}$$

Three cases will be discussed in the following, under the assumption that $\sigma_i^{St} = \sigma_i^{AS}$

(i) $\sigma_i = i\sigma_0$

The Stokes and anti-Stokes intensities become:

$$I_{St} = \sum_i n_i \sigma_{i+1} I_{laser} = \sum_i n_i (i+1) \sigma_0 I_{laser} \qquad \text{(A.3)}$$

$$I_{AS} = \sum_i n_i \sigma_i I_{laser} = \sum_i n_i i \sigma_0 I_{laser} \qquad \text{(A.4)}$$

The population of level i can be written according to the Boltzmann distribution:

$$n_i = n_{i-1} e^{-\alpha} = \ldots = n_0 e^{-i\alpha} \qquad \text{(A.5)}$$

where following notation has been made:

$$\alpha = \frac{\hbar\omega}{k_B T} \qquad \text{(A.6)}$$

with $\hbar$ the Planck constant, ω the vibrational frequency, k_B the Boltzmann constant, and T the temperature.

The sum of the populations n_i over all levels i equals the total number of scattering molecules per unit volume N_0:

$$N_0 = \sum_i n_i = \sum_i n_0 e^{-i\alpha} = \frac{n_0}{1 - e^{-\alpha}} \qquad \text{(A.7)}$$

Inserting (A.7) into (A.5) results:

$$n_i = N_0\left(1-e^{-\alpha}\right)e^{-i\alpha} \qquad \text{(A.8)}$$

With (A.8), Eq. (A.3) transforms into:

$$I_{st} = N_0\sigma_0 I_{laser}\left(1-e^{-\alpha}\right)\sum_i (i+1)e^{-i\alpha} = N_0\sigma_0 I_{laser}\left(\frac{1}{e^{\alpha}-1}+1\right) \qquad \text{(A.9)}$$

and Eq. (A.4) becomes:

$$I_{st} = N_0\sigma_0 I_{laser}\left(1-e^{-\alpha}\right)\sum_i ie^{-i\alpha} = N_0\sigma_0 I_{laser}\frac{1}{e^{\alpha}-1} \qquad \text{(A.10)}$$

Here, the equality $\sum_i ie^{-i\alpha} = \frac{\partial}{\partial\alpha}\left(\sum_i e^{-i\alpha}\right) = \frac{e^{-\alpha}}{(1-e^{-\alpha})^2}$ has been used.

With the notation:

$$\frac{1}{e^{\alpha}-1} = n(\omega,T) \qquad \text{(A.11)}$$

Eq. (A.2) transforms:

$$M(\omega,T) = \frac{n(\omega,T_e)-n(\omega,T_r)}{n(\omega,T_r)+1} \qquad \text{(A.12)}$$

(ii) $\sigma_i = \sigma_{i-1} = \ldots = \sigma_0$

In this case, one can write for the stokes and anti-Stokes intensities:

$$I_{St} = \sum_i n_i\sigma_0 I_{laser} = N_0\sigma_0 I_{laser}(1-e^{-\alpha})\sum_i e^{-i\alpha} = N_0\sigma_0 I_{laser} \qquad \text{(A.13)}$$

$$I_{AS} = I_{St} - I_{n_0} = N_0\sigma_0 I_{laser} - n_0\sigma_0 I_{laser} = N_0\sigma_0 I_{laser}e^{-\alpha} \qquad \text{(A.14)}$$

Introducing (A.13) and (A.14) in (A.2), following expression is obtained:

$$M = e^{-\frac{\hbar\omega}{k_B T_e}} - e^{-\frac{\hbar\omega}{k_B T_r}} \qquad \text{(A.15)}$$

(iii) $\sigma_i = 0$ for $i \geq 1$

$$I_{St} = N_0\sigma_0 I_{laser} \qquad \text{(A.16)}$$

$$I_{AS} = n_1\sigma_0 I_{laser} = N_0\sigma_0 I_{laser}\left(1-e^{-\alpha}\right)e^{-\alpha} \qquad \text{(A.17)}$$

With (A.16) and (A.17), Eq. (A.2) can be written as:

$$M = \frac{e^{-\frac{\hbar\omega}{k_B T_e}}}{n(\omega,T_e)+1} - \frac{e^{-\frac{\hbar\omega}{k_B T_r}}}{n(\omega,T_r)+1} \qquad \text{(A.18)}$$

In Eq. (A.18) the notation (A.11) has been used.

Zusammenfassung

In vielen Fällen werden verschiedene elektronische Zustände eines Moleküls als unabhängig voneinander betrachtet. Diese Vereinfachung entspricht oft nicht hinreichend der Realität. Beträchtliche Wechselwirkungen zwischen elektronischen Niveaus werden durch die Bewegung der Kerne, d.h. durch vibronische Kopplung hervorgerufen.

Die vorliegende Arbeit gliedert sich in zwei Teile. Der erste Teil befasst sich mit der vibronischen Kopplung zweier angeregter Elektronenniveaus in einem Polyen.

Der zweite Teil ist der Rolle von Schwingungsmoden beim ultraschnellen photoinduzierten intramolekularen Elektronentransfer gewidmet.

Vibronische Kopplung in Polyenen übt einen wesentlichen Einfluss auf die Relaxation der Elektronenniveaus aus. Die Kenntnis der mikroskopischen Vorgänge ist von entscheidender Bedeutung für ein Verständnis von Energietransfermechanismen, wie sie z. B. in photosynthetischen Systemen auftreten.

Wir haben Diphenylhexatrien mit Pikosekunden-zeitaufgelöster Kohärenter Antistokes Ramanspektroskopie (CARS) in Hinblick auf vibronische Kopplungsmechanismen zwischen den angeregten Elektronenniveaus untersucht.

Im Gegensatz zum typischen Ramanspektrum des elektronischen Grundzustands von Polyenmolekülen, in dem wenige starke Ramanlinien im Frequenzbereich der C-C bzw. C=C Streckschwingungen der Kette auftreten, weist das Spektrum im angeregten Zustand des Diphenylhexatriens eine Vielzahl von Ramanlinien auf, die über den gesamten Spektralbereich verteilt sind. Überraschend ist das Auftreten zweier extrem frequenzverbreiterter Ramanlinien, die gegenüber dem C=C Streckschwingungsbereich zu höheren Wellenzahlen verschoben sind. Beide Ramanlinien lassen sich mit Erhöhung der Lösungsmittelpolarisierbarkeit (d. h. mit Erniedrigung des energetischen Abstandes zwischen den angeregten elektronischen Niveaus) um mehr als 50 cm^{-1} in Richtung niedrigerer Frequenzen verschieben.

Die Pikosekunden-zeitaufgelösten Messungen, die mit einer Impulsdauer von 2 ps durchgeführt wurden zeigen, dass beide Banden gleichzeitig auftreten und dass deren Intensitätsanstieg durch die zeitliche Auflösung unserer Apparatur bestimmt wird. Weiterhin ist keine Änderung in den relativen Intensitäten der beiden Linien mit Veränderung des Energieabstandes der beiden niedrigsten angeregten Sigulettzustände festzustellen. Dies lässt den Schluss zu, dass es sich hierbei nicht um zwei im thermischen Gleichgewicht befindlichen elektronisch angeregten Zustände handelt, sondern dass die Ramanlinien einem gemeinsamen angeregten Elektronenzustand zuzuordnen sind.

Für ein Verständnis dieser ungewöhnlichen Phänomene, die wir zum ersten Mal beobachten, wurden quantenchemische Rechnungen durchgeführt. Sie ermöglichen die Zuordnung der beiden Ramanlinien als totalsymmetrische C=C Streckschwingungsmoden. Die Verschiebung einer Ramanlinie zu höheren Wellenzahlen ist auf eine bereits bekannte vibronische Kopplung zwischen dem elektronischen Grundzustand und dem ersten angeregten Singulettzustand zurückzuführen. Sie kann aber nicht das Auftreten von zwei Linien erklären.

Zur Erklärung des Sachverhalts werden zwei Modelle diskutiert:

(i) Die Existenz zweier Isomere im ersten angeregten Elektronenniveau des Diphenylhexatriens.
In diesem Fall führen kleine Abweichungen von der C_{2h} Symmetrie des Moleküls durch Änderung der vibronischen Kopplungskonstanten zu signifikanten Verschiebungen der Frequenzen der Ramanlinien.

(ii) Vibronische Kopplung der beiden Elektronenniveaus durch eine niederfrequente asymmetrische Schwingungsbewegung (b_u -Mode).
In diesem Modell bildet sich unter Bedingungen eines sehr kleinen Energieabstandes zwischen den Elektronenniveaus ein Doppelmuldenpotential im niedrigsten angeregten Singulettzustand entlang der Koordinate der totalsymmetrischen C=C Streckschwingung der Polyenkette (pseudo Jahn-Teller Effekt). Auf diese Weise können zwei unterschiedliche Schwingungsfrequenzen durch eine gleichartige Schwingungsbewegung erzeugt werden. Die unterschiedlichen Krümmungen der beiden Potentialminima bestimmen die Frequenzen der beiden Schwingungsresonanzen. Eine Verringerung des Energieabstandes zwischen den Elektronenniveaus führt zu einer geringeren Krümmung in beiden Minima und damit zu einem Absinken beider Frequenzen, in Übereinstimmung mit dem Experiment.

Die Abgabe der Überschussenergie nach photoinduzierten elementaren Reaktionen (wie z. B. dem Elektronentransfer) in kondensierter Materie erfolgt in vielen Fällen durch strahlungslose Deaktivierung vom angeregten Elektronenzustand in den Grundzustand und durch Transfer der Energie zum Lösungsmittel. Für ein Verständnis der mikroskopischen Mechanismen beim Elektronentransfer ist eine Analyse der Rolle der beteiligten Molekülschwingungen von grosser Wichtigkeit.
Wir haben hierfür stationäre Ramanspektroskopie und insbesondere Messungen der Stokes- und anti-Stokes-Ramanspektren mit Pikosekunden-Zeitauflösung angewendet. Quantenchemische Rechnungen auf *ab initio* Basis ergänzen diese Untersuchungen.
Die Dynamik der Besetzung angeregter Schwingungsniveaus nach photoinduziertem intramolekularem Elektronenrücktransfer in Betain-30 wurde in schnell und in langsam relaxierenden Lösungsmitteln untersucht (d. h. in Lösungsmitteln, in denen die Solvatisierungsdynamik die Kinetik des Elektronenrücktransfers beträchtlich verkürzt, bzw. nur unwesentlich beeinflusst). Zum ersten Mal wurde eine modenspezifische Kinetik der Ramanaktiven Schwingungen nach Elektronentransfer beobachtet. Sie ist besonders ausgeprägt in Betain-30, das in einem schnell relaxierenden Lösungsmittel gelöst ist. Hier weist die höchstfrequenteste Mode bei 1603 cm^{-1} eine Anklingzeit ihrer Besetzung auf, die mit der Elektronenrücktransferzeit nahezu übereinstimmt. Dies spricht für eine direkte Besetzung der Mode durch den Rücktransfer. Dagegen klingen niederfrequentere Moden deutlich langsamer an, und haben zu einem späteren Zeitpunkt eine höhere Besetzung als die hochfrequenten Moden. Das spricht für einen geringeren direkten Energietransfer in der Anfangsphase und für die Existenz von zusätzlichen Kanälen der intramolekularen Schwingungsenergieumverteilung, die zu einer höheren Besetzung zu einem späteren Zeitpunkt führt. Die Modenspezifik geht in langsam relaxierenden Lösungsmitteln verloren, was auf die Dominanz intramolekularer Schwingungsenergieumverteilung hinweist.
Eine Thermalisierung zwischen den beobachteten Ramanaktiven Moden stellt sich frühestens 10 ps nach Anregung ein. Die Schwingungstemperatur dieser Moden übersteigt zu diesem Zeitpunkt 600 K und ist in langsam relaxierenden Lösungsmitteln sogar noch höher. Die berechnete Gleichgewichtstemperatur des isolierten Moleküls

(berechnet unter der Annahme, dass die Überschussenergie über alle Freiheitsgrade des Moleküls verteilt ist) ist allerdings niedriger als dieser Wert, was auf eine nicht abgeschlossene intramolekulare Thermalisierung in dem gesamten Molekül schliessen lässt. Die niedrigere Temperatur in schnell relaxierenden verglichen zu langsam relaxierenden Lösungsmitteln ist auf einen direkten Transfer eines Teils der Überschussenergie zum Lösungsmittel zurückzuführen.

Quantenchemische Rechnungen und stationäre Stokes-Raman Messungen deuten auf eine besondere Rolle zweier niederfrequenter Moden bei Elektronenrücktransfer hin. Es sind dies die 133 cm^{-1} und die 290 cm^{-1} Mode, die einer Torsion zwischen dem Phenoxid- und Pyridinring, bzw. einer N-Inversions Bewegung zuzuordnen sind.

Diese Ergebnisse demonstrieren, dass die Methode der zeitaufgelösten Ramanspektroskopie einen Einblick in den Mechanismus der Elektronentransfersreaktion ermöglicht. Sie sind zumindest qualitativ in Übereinstimmung mit Rechnungen die auf Fermi's Goldener Regel basieren, die eine dominante Rolle hochfrequenter Ramanaktiver Moden mit hohen Franck-Condon Faktoren beim Elektronentransfer vorhersagen.

LEBENSLAUF

Persönliche Daten	Name	Sebastian Wachsmann-Hogiu	
	Geburtsdatum/Ort	01.02.1968 in Prundu-Bargaului, Rumänien	
	Familienstand	ledig	
Ausbildung und beruflicher Werdegang	Schulbildung	1974 – 1978	Grundschule in Prundu-Bargaului, Rumänien
		1978 – 1982	Gymnasium in Prundu-Bargaului, Rumänien
		1982 – 1986	Obergymnasium in Bistrita, Rumänien (Mathematik-Physik)
	Wehrdienst	Sept. 1986 – Juni 1987	
	Studium	1987 – 1992	Diplomstudiengang Physik an der Univ. Bukarest, Rumänien
		Juni 1992	Diplom im Fach Physik, Spezialfach Biophysik
		1993 – 1996	Wissenschaftlicher Assistent an der Laserabteilung des Instituts für Atomphysik Bukarest, Magurele, Rumänien
		09/1996 – 07/1997	DAAD Stipendium am Max-Born-Institut für Nichtlineare Optik und Kurzzeitspektroskopie, Berlin
		Seit 08/1997	Anfertigung der vorliegenden Dissertation am Max-Born- Institut für Nichtlineare Optik und Kurzzeitspektroskopie, Berlin, bei Herrn Prof. Dr. Thomas Elsässer

:

ERKLÄRUNG

Hiermit erkläre ich, die Dissertation selbständig und ohne unerlaubte Hilfe angefertigt zu haben.

Ich habe mich anderwärts nicht um einen Doktorgrad beworben und besitze einen entsprechenden Doktorgrad nicht.

Ich erkläre die Kenntnisnahme der dem Verfahren zugrunde liegenden Promotionsordnung der Mathematisch-Naturwissenschaftlichen Fakultät I der Humboldt-Universität zu Berlin.

10. Juli 2000 Sebastian Wachsmann-Hogiu